Al-Si Cast Alloys - Microstructure and Mechanical Properties at Ambient and Elevated Temperature

MOHAMMADREZA ZAMANI

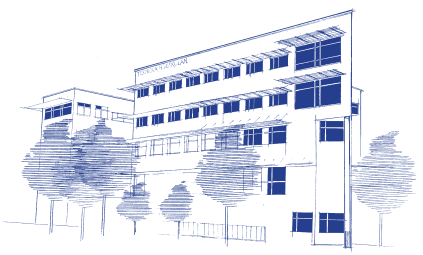

School of Engineering
Jönköping University

Licentiate thesis
Dissertation Series No. 7 • 2015

LICENTIATE THESIS

Al-Si Cast Alloys - Microstructure and Mechanical Properties at Ambient and Elevated Temperature

MOHAMMADREZA ZAMANI

SCHOOL OF ENGINEERING
JÖNKÖPING UNIVERSITY

Department of Materials and Manufacturing
SCHOOL OF ENGINEERING, JÖNKÖPING UNIVERSITY
Jönköping, Sweden 2015

Al-Si Cast Alloys -
Microstructure and Mechanical Properties at Ambient and Elevated Temperature

Mohammadreza Zamani

Department of Materials and Manufacturing
School of Engineering, Jönköping University
SE-551 11 Jönköping, Sweden
mohammadreza.zamani@jth.hj.se

Research Series from the School of Engineering, Jönköping University
Department of Materials and Manufacturing
Dissertation Series No. 7, 2015
ISBN 978-91-87289-08-8

Published and Distributed by
School of Engineering, Jönköping University
Department of Materials and Manufacturing
SE-551 11 Jönköping, Sweden

Printed in Sweden by
Ineko AB
Kållered, 2015

ABSTRACT

Aluminium alloys with Si as the major alloying element form a class of material providing the most significant part of all casting manufactured materials. These alloys have a wide range of applications in the automotive and aerospace industries due to an excellent combination of castability and mechanical properties, as well as good corrosion resistance and wear resistivity. Additions of minor alloying elements such as Cu and Mg improve the mechanical properties and make the alloy responsive to heat treatment. The aim of this work is studying the role of size and morphology of microstructural constituents (e.g SDAS, Si-particles and intermetalics) on mechanical properties of Al-Si based casting alloy at room temperatures up to 500 ºC.

The cooling rate controls the secondary dendrite arm spacing (SDAS), size and distribution of secondary phases. As SDAS becomes smaller, porosity and second phase constituents are dispersed more finely and evenly. This refinement of the microstructure leads to substantial improvement in tensile properties (e.g. R_m and ε_F). Addition of about 280 ppm Sr to EN AC-46000 alloy yields fully modified Si-particles (from coarse plates to fine fibres) regardless of the cooling conditions. Depression in eutectic growth temperature as a result of Sr addition was found to be strongly correlated to the level of modification irrespective of coarseness of microstructure. Modification treatment can improve elongation to failure to a great extent as long as the intermetallic compounds are refined in size.

Above 300 ºC, tensile strength, $R_{p0.2}$ and R_m, of EN AC-46000 alloys are dramatically degraded while the ductility was increased. The fine microstructure (SDAS 10 μm) has superior R_m and ductility compared to the coarse microstructure (SDAS 25 μm) at all test temperature (from room to 500 ºC). Concentration of solutes (e.g. Cu and Mg) in the dendrites increases at 300 ºC and above where $R_{p0.2}$ monotonically decreased. The brittleness of the alloy below 300 ºC was related to accumulation of a high volume fraction damaged particles such as Cu- Fe-bearing phases and Si-particles. The initiation rate of damage in the coarse particles was significantly higher, which enhances the probability of failure and decreasing both R_m and ε_F compared to the fine microstructure. A physically-based model was adapted, improved and validated in order to predict the flow stress behaviour of EN AC-46000 cast alloys at room temperature up to 400 ºC for various microstructures. The temperature dependant variables of the model were quite well correlated to the underlying physics of the material.

Keywords: Al-Si based casting alloys, elevated temperature, microstructural scale effect, Sr modification

ACKNOWLEDGEMENTS

First of all, I am grateful to the Almighty God for providing me wisdom and means to continue my studies up to this level.

I express my sincere gratitude to:

Asscociate Prof. Salem Seifeddine, my supervisor, for the continuous support during my study, insightful discussion on my research, for his patience and motivation.

Prof. Anders Jarfors, my supervisor, for the valuable comments and advices and for giving me the opportunity to pursue my academic study in higher level.

Assistant Prof. Nils-Erik Andesson, for helpful discussion and useful comments.

Associate Prof Ales Svoboda for helping me with the modelling parts.

Toni Bogdanoff, Lars Johansson, Esbjörn Ollas and master student Mana Azizderouei for helping me with the experimental work.

My cheerful friends who are more than just solid colleagues at the School of Engineering whom I have been blessed with in my daily work. Thank you very much for making the working atmosphere as cool as possible.

The KK-stiftelsen (The Knowledge Foundation) for the financial support.

The industrial partner Kongsberg Automotive AB and their helpful personell; Albin Hagberg, Jonas Rolfart, Anneli Johansson, Sofie Rydell Wigren, Jonas Bergner, Endre Berta, Henrik Nilsson and Meron Kliger.

My family; Hossein, Azam, Zeinab, Osveh, Mohammad, Mohesn, Afsaneh, Saber, Niloofar and Safa who have brought great joy to my life. Finally I owe much to Hoda, without her love and understanding I would not have completed this work.

Mohammadreza Zamani

Jönköping 2015

SUPPLEMENTS

The following supplements constitute the basis of this thesis.

Supplement I M. Zamani, S. Seifeddine, A.E.W Jarfors**;** Effects of Microstructure and Defects on Tensile and Fracture Behaviour of a HPDC Component; Potential Properties and Actual Outcome of EN AC-44300 Alloy, Light Metals Proceeding, TMS 2014. February 16th-20th, San Diego, CA, USA.

Zamani was the main author. Seifeddine and Jarfors contributed with advice regarding the work.

Supplement II M. Zamani, S. Seifeddine, M. Azizderouei; The Role of Sr on Microstructure Formation and Mechanical Properties of Al-Si-Cu-Mg Cast Alloys, Light Metals Proceeding, TMS 2013. March 3rd-7th, San Antonio, TX, USA.

*Zamani was the main author. Seifeddine contributed with advice regarding the work. Azizideroue*i *helped with the experimental within her master thesis work.*

Supplement III M. Zamani, S. Seifeddine; Assessment of Modification Level in EN AC-46000 Aluminium Cast Alloys Using Thermal Analysis and Microscopic Evaluation, Metals Proceeding, TMS 2015. March 15th-19th, Orlando, FL, USA.

Zamani was the main author. Seifeddine contributed with advice regarding the work.

Supplement IV M. Zamani, S. Seifeddine, A.E.W. Jarfors; High Temperature Tensile Deformation Behaviour and Failure Process of an Al-Si-Cu-Mg Cast Alloy – The Microstructural Scale Effect. Submitted to the journal of Materials & Design.

Zamani was the main author. Seifeddine and Jarfors contributed with advice regarding the work.

Supplement V M. Zamani, H. Dini, A. Svoboda, L.E Lindgren, S. Seifeddine, N. Andersson, A.E.W. Jarfors; A Dislocation Density Based Yield Stress Model for as-cast EN AC-46000 Alloy; Effect of Temperature and Microstructure. To be submitted to the journal of Materials & Design.

Zamani was the main author. Dini, Svoboda Lindegren contributed in optimization and curve-fitting of the model. Seifeddine, Jarfors and Andersson contributed with advice regarding the work.

TABLE OF CONTENTS

CHAPTER I

INTRODUCTION

CHAPTER INTRODUCTION

This chapter starts with a background on the Al-Si casting alloy system, including alloying elements, solidification and typical casting irregularities in these alloys. The mean, tools and mechanisms of cooling rate refinements of microstructure and eutectic modification will be described. The features that control the tensile properties and deformation mechanisms are explained. Eventually the model based on density of dislocation and concentration of vacancy, which has been used in this work, is introduced.

1.1 AL-SI BASED CASTING ALLOYS

1.1.1 Background

Due to economic and environmental requirements, it is becoming increasingly important to reduce vehicle weight. For such an objective, Al-Si cast alloys have been widely employed to produce automotive components working at ambient and fairly high temperature (up to 200 ºC) due to excellent characteristics such as low cost manufacturing, excellent castability, high specific strength and recyclability [1, 2]. Cu and Mg are commonly added to improve the strength at room and elevated temperatures and enable the possibility of heat treatment [3]. The microstructure of these casting alloys contains α-Al dendrites as the main constituent, which is decorated with eutectic Si particles and many intermetallic phases such as Al_2Cu, Mg_2Si, Fe-bearing phases etc. The size, morphology and distribution of microstructural features govern the mechanical properties of theses alloys [4]. It is well-known that a refined microstructure results in improved tensile properties. The refinement of microstructure can be achieved through high cooling rate or chemical modification. Usage of Al-Si-Cu-Mg alloys at temperature above 230 ºC is however limited due to coarsening of Si particles and dissolution of Cu- and Mg-bearing phases.

1.1.2 Alloying elements

Si is the main and most important alloying element of Al-Si cast alloy. In hypoeutectic Al-Si alloy, the Si content normally varies from 5 to 12 wt. %. Si is primarily responsible for so-called "good castability"; i.e., the ability to readily fill dies and to solidify castings with no hot tearing or hot cracking issues. The more Si an alloy contains, the lower is its thermal expansion coefficient. Si is a very hard phase, thus it contributes significantly to an alloy's wear resistance. Si combines with other elements to improve an alloy's strength and to make alloys heat treatable.

An alloy which comprises more than 7 wt. % of Si forms three-dimensional eutectic Si networks of interconnected Si platelets embedded in the ductile-Al matrix upon solidification [5-7]. Si content in Al-Si based cast alloys influences tensile properties at both room and elevated temperature; while its role becomes more highlighted in the absence of alloy elements (e.g. Cu, Mg and Fe) [8]. The contribution to the strength of Al-Si alloys is caused by the load transfer from α-Al matrix to the rigid highly interconnected Si plates [9]. The load carrying capability of the eutectic Si can be reduced by means of spheroidization which results in, improving the machinability, ductility and fatigue resistance of the alloys [5, 6]. As the Al-Si cast alloys exposed under elevated temperature, the eutectic Si particles first fragment and spheroidize, then coarsen and their aspect ratio decreases, which results in a loss of interconnectivity of the eutectic phases. The rate of rate of losing interconnectivity is strongly dependent on temperature and time of exposure [5, 7, 10, 11]. It has been reported that increasing the Si content from 7 wt% to 12 wt% in a low alloy element Al-Si cast alloy, lead to improvement of yield strength and UTS of up to 22 and 25 MPa at 250 ºC respectively [12].

Two important alloying elements which have been widely added to Al-Si cast alloys are Cu and Mg, which increase the strength of the alloy at room and elevated temperature (up to 190 ºC) and makes them responsive to heat treatment. These alloys are used for a wide range of applications, such as engine cooling fans, crank cases, high speed rotating parts, structural aerospace components, air compressor pistons, fuel pumps, compressor cases, timing gears, rocker arms, machine parts, etc. [3,4]. When they are exposed to temperatures above 200 ºC, the major alloy strengthening phases like θ(Al_2Cu), β(Mg_2Si) and/or S(Al_2CuMg) tend to become unstable, coarsen rapidly, and then dissolve, leading to the production of an alloy which has an undesirable microstructure for high temperature applications [8].

The addition of Mg is associated with enhancing the tensile properties of Al-Si alloys at elevated temperature (up to ~200 ºC). The presence of Mg also enhances creep resistance and decreases the rate of strength loss at high temperature in the alloys [8, 13]. The significant increase in strength at high temperature was achieved after solution treatment due to activating precipitation hardening through Mg bearing phases. The increase in high temperature strength of the Mg containing alloys can only be attributed to the precipitation of secondary phase β-Mg_2Si[8]. Cu addition was found to increase the strength at elevated temperatures (up to ~200 ºC) and to improve creep resistance of Al-Si alloys [8, 13, 14].

1.1.3 Solidification

Al-Si alloys solidify by a primary precipitation of dendrites; an illustration of primary aluminium dendrite (α-Al) structure embedded in Al-Si eutectic is shown in Figure 1. In hypoeutectic Al-Si alloys primary aluminium solidifies dendritically and grows in <100> direction. Dendrites are often drawn having four secondary arms growing around the primary stem at each junction which is true for cubic structures [15]. The undercooling depends on the cooling rate, the concentration of the alloying element in the melt and the type of the alloying element. It is well established that the undercooling increases with increasing cooling rate and increasing concentration of the alloying element [16].

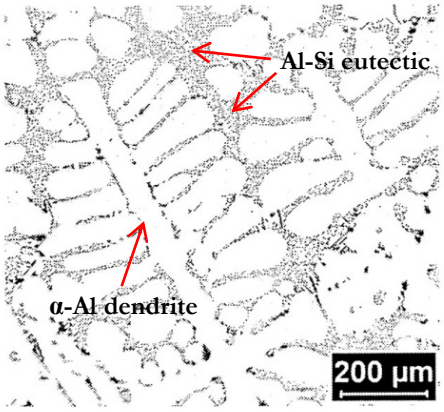

Figure 1. Solidification structure of hypoeutectic Al-Si alloy [10].

The solidification of the alloy continues with formation of Al-Si eutectic mixture. In eutectic solidification two phases of Al and Si precipitate simultaneously from the liquid at constant temperature [16, 17]. Figure 2 presents a phase diagram of the Al-Si system with a eutectic point. The eutectic point is at 12.6 wt. % Si and the eutectic temperature is 577 °C. Aluminium dissolves a maximum of 1.6 wt. % of Si while the solubility of Al in Si is almost zero [18]. Eutectic alloys provide a natural composite which gives good properties for the alloy. [16, 17]. Commercial aluminium alloys often contain other alloying elements such as Cu and Mg in addition to Si. The eutectics of these alloys may be more complex than those observed when looking at the binary system. Formation of Cu- and Mg-bearing intermetallic phases often occurs after eutectic formation.

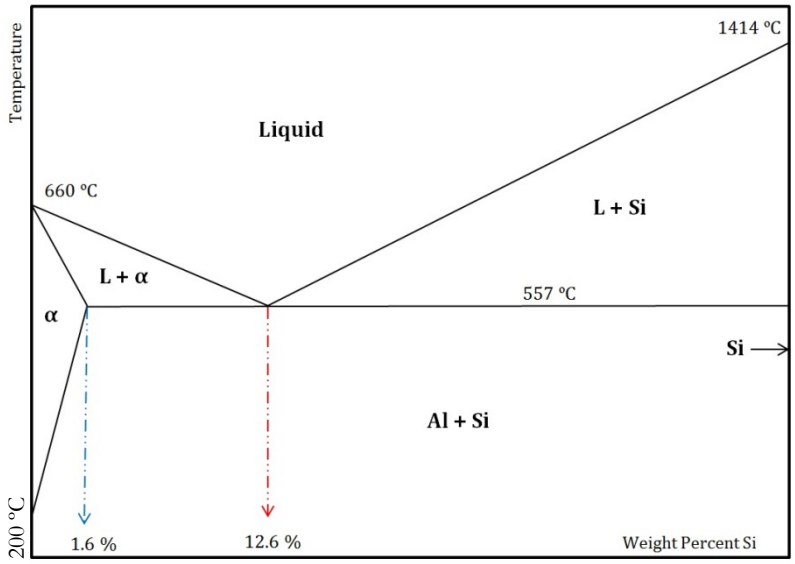

Figure 2. The schematic phase diagram of Al-Si.

1.1.4 Casting defects

The level and type of defects in Al-Si castings depend on the condition of the melt, the manufacturing process and post solidification treatments. Such defects in the castings cause an unfortunate scattering of the mechanical properties and degrade the performance of the component. Lowered defect content results in more reliable castings which enable designers to design thinner sections; lowering weight and material use. The reduction in weight is

important because a large portion of the aluminium castings, roughly two thirds, are manufactured for the automotive industry [19]. The most typical defect in Al-Si originates from either processing or chemical composition. Gas porosity and oxides are two common irregularities which are initiated through poor melt treatment or non-optimized casting route. High levels of iron are also associated with formation of deleterious compounds which appear as defects in the casting.
Once solidification of the alloy progresses, any excess hydrogen, not soluble in the solid and not able to escape the solidified section, will form porosity within the casting, reducing its properties. If the die cavity filling is not in steady state, additional pores will appear in the casting, an effect which is more probable in the HPDC process. When the melt meets with oxygen, aluminium will immediately oxidise forming a skin of oxide. If the oxide skin is removed or cracked, a new oxide layer will immediately form. The oxide film formed on aluminium has an amorphous structure and has a low permeability and therefore creates a protective layer at the surface of the liquid aluminium. As long as the oxides are at the surface of the melt they do not present any significant threat to the quality of the liquid metal. However, melting, pouring and transferring liquid metal will most certainly entrain newly formed thin oxides into the melt making them possibly harmful [20].
Beside the porosity and oxides, iron is the most common impurity, and possibly the most detrimental, in Al-Si cast alloy. The solubility in solid aluminium is about 0.05 wt. % at 660°C. The solubility is even less at room temperature and when iron is present in the melt it will form quite harmful intermetallic compounds. Increasing the Fe content drastically reduces the ductility of the alloy. However a minor amount of 0.8-1.0 wt. % is normally favourable to avoid die soldering. Increasing the iron content even more will also affect the tensile strength, however the reduction in tensile strength is less severe [21].
There are a number of intermetallic phases that have been identified in aluminium-Si based alloys. The most important phases are α-$Al_{15}(Fe,Mn)_3Si_2$ and β-Al_5FeSi, where the α phase appears as Chinese script or polyhedrons and the β phase appears as 2-D needles and 3-D platelets. The β phase is the most undesirable Fe-bearing phase due to its morphology which causing a greater reduction in ductility. The most efficient way of promoting formation of α phase in favour of the more detrimental β phase is neutralisation with Mn addition. The amount of Mn addition is related to the Fe content and cooling rate.

1.2 MICROSTRUCTURE OF THE ALLOYS

The microstructure of the Al-Si cast alloys primarily consists of a primary phase (α-Al) and eutectic mixture of Al-Si. The amount of eutectic mixture in the microstructure depends on the level Si. The eutectic mixture contains soft Al as matrix containing Si particles. The morphology of Si-particles is plate-like which may be altered upon modification treatment. The presence of Cu, Mg and Fe in the alloy leads to formation of various intermetallic compounds in the microstructure of the alloy. The most common intermetallic phases are Al_2Cu, Mg_2Si, α-$Al_{12}(Fe,Mn)_3Si_2$ and β-Al_5FeSi. The cooling rate has a marked effect on the size, morphology, and distribution of all the microstructural constituents. Increasing cooling rate refines all microstructural features in size, decreases SDAS, changes the morphology of eutectic Si from large and elongated plates-like to small and rounder ones and decreases the size of all intermetallic compounds regardless of their type. Although an increased cooling rate refined eutectic Si-particles, the plate-like morphology of them remained unaffected. However a Sr treatment may modify the coarse plate-like morphology of Si-particles to fine fibrous. The mechanisms of both cooling rate refinement and Sr-modification of eutectic Si-particles are briefly explained in the following sections.

1.2.1 Cooling rate refinement and mechanisms

The cooling rate refinement of eutectic Si-particles has been described based on the surface energy of the Al-Si solid interface [22]. This theory is one of the widely accepted theories for quench modification. The rate of advance of the solidification interface depends on a balance between the rate of heat flow from the liquid to the solid through the interface and the latent heat of fusion released during solidification. The thermal conductivities of Al and Si in their pure form are 205 and 83 W/(mK) respectively, and their latent heats of fusion are 396 and 1411 J/g respectively. Since the difference between the magnitude of the thermal conductivity of pure Al and pure Si and the difference between the magnitude of the latent heat of fusion of pure Al and pure Si are large, Al will solidify much faster than Si. Thus, Al gains a lead during solidification of the eutectic as shown in Figure 3(a).

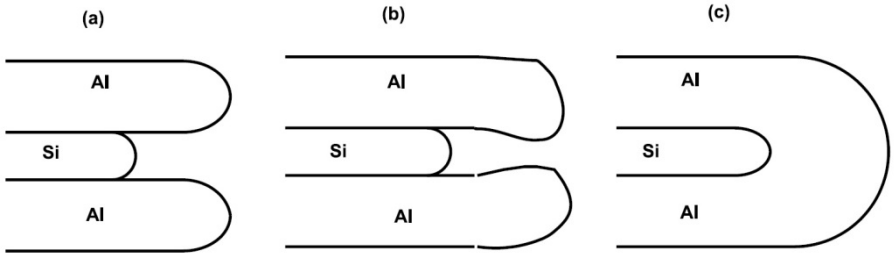

Figure 3. Eutectic solidification in unmodified chill cast Al–Si alloys [22].

As the cooling rate increases, the lead of Al over Si increases causing complete encasement of the lagging Si crystal by the advancing Al as depicted in Figure 3(b) and(c). This theory accounts for the formation of the modified eutectic structure at high cooling rates [22].

1.2.2 Eutectic Si Modification

1.2.2.1 Characteristics and means

One way to improve mechanical properties of Al-Si based foundry alloys is through modification. The Al-Si eutectic consists of a hard, brittle Si phase in a softer Al matrix which is the reason why most of the mechanical properties of castings, especially the elongation to fracture, are determined by the eutectic microstructure. The term "modification" describes the method in which inoculants in the form of master alloys are added to an Al melt in order to promote the formation of a fine and fibrous eutectic Si structure during the solidification process. Modification of the Al–Si eutectic from a flake-like (Figure 4a) to a fine fibrous Si structure (Figure 4b) can be achieved in two different ways; by addition of certain elements (chemical-modification) or with a rapid cooling rate (quench-modification). Several modifiers are known (e.g., strontium, sodium, antimony, barium and calcium), of which strontium is the most addition that has been employed in the Al alloy industry in recent years as a chemical modifier owing to the following reasons: (a) it is easy to handle, (b) it is effective and (c) its fading effect is low. Addition of a few hundred parts per million Sr modifies the eutectic Si morphology from coarse plate-like into fine fibrous and has a beneficial effect on both strength and ductility, which is due to changing the fracture mode from transgranular and brittle to intergranulare and interdendritic.

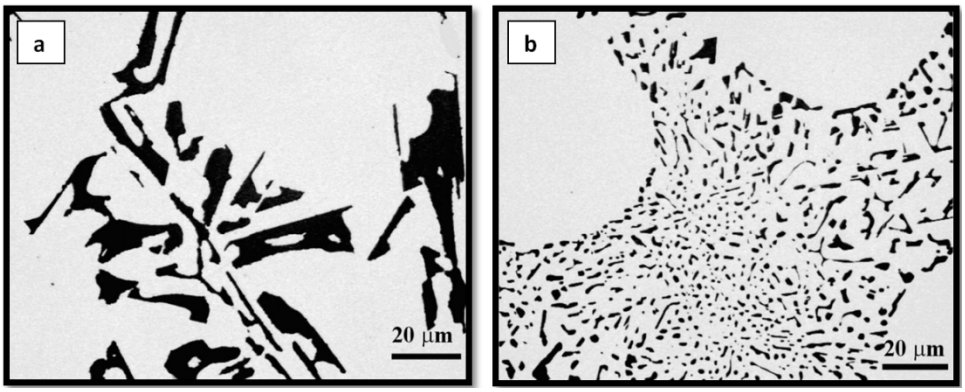

Figure 4. The morphology of eutectic Si; (a)Unmodified and (b) Modified structure [23].

In hypereutectic compositions (Si content exceeding 12.6 wt. %), phosphorus is added to the molten alloys which has a marked effect on the distribution and form of the primary Si phase. Investigations have shown that retained trace concentrations as low as 0.0015 through 0.03 % P are effective in achieving the refined structure. No elements are known that beneficially modify both the eutectic and hypereutectic phases. Modification has been recognized to change the amount, characteristics, and distribution of porosity. An impediment to a full acceptance of eutectic modification as a means to improve the mechanical properties of as-cast components is that modification often results in increased porosity, although this claim is not fully accepted and porosity is strongly linked to casting parameters. Modification can lose its positive effect by addition of large amounts of modifier (Na > 0.02 and Sr > 0.1 wt. %) which called overmodification and which often causes the formation of Al_2Si_2Sr brittle compounds which degrade alloy performance. However eutectic modification is not always a guarantee for improving performance of Al-Si based alloys, and the presence of other undesirable compounds (like Fe-rich intermetallic compounds) or casting defects may dominate properties. Several techniques such as metallographic study, thermal analysis and a method based on physical properties of the alloys have been utilized to assess the modification level of eutectic Si in Al cast alloys. The assessment based on analysis of cooling curves has been introduced as the most accurate and least subjective technique for this purpose [23].

1.2.2.2 Mechanisms

In order to realize the mechanisms of eutectic Si modification – both quench and chemical, it is very important to understand the growth mechanism of flaky Si (unmodified) beforehand. Most of the theories which explain modification assume a change in growth mechanism of Si. So unless a complete understanding of the growth of flaky Si is available, theories of modification would still be incomplete. However, the exact growth mechanism of flaky Si is still under debate. The proposed growth mechanisms of flaky Si are discussed below, subsequently the possible modification mechanism are introduced.

1.2.2.2.1 Growth mechanisms of flaky Si

Twin Plane Re-entrant edge (TPRE) Mechanism: This was first introduced to explain the growth of germanium dendrites and was later extended to the growth of Si. The equilibrium habit of Si is an octahedron bound by eight (111) planes. A twin crystal is half of the equilibrium crystal reflected across the remaining solid along the twin composition plane. Consequently, the outline of the twin Si crystal consists of six edges of the intersection of pairs of (111) planes as shown in Figure 5(a). The external angles between these bounding

planes are 141° and 219°. The bounding planes that make a 141° external angle form a re-entrant corner, while those planes that make a 219° external angle form a ridge. Because of the more favorable bonding for an atom joining a re-entrant corner than one joining a ridge, re-entrant corners are more favorable nucleation sites than ridges [24].

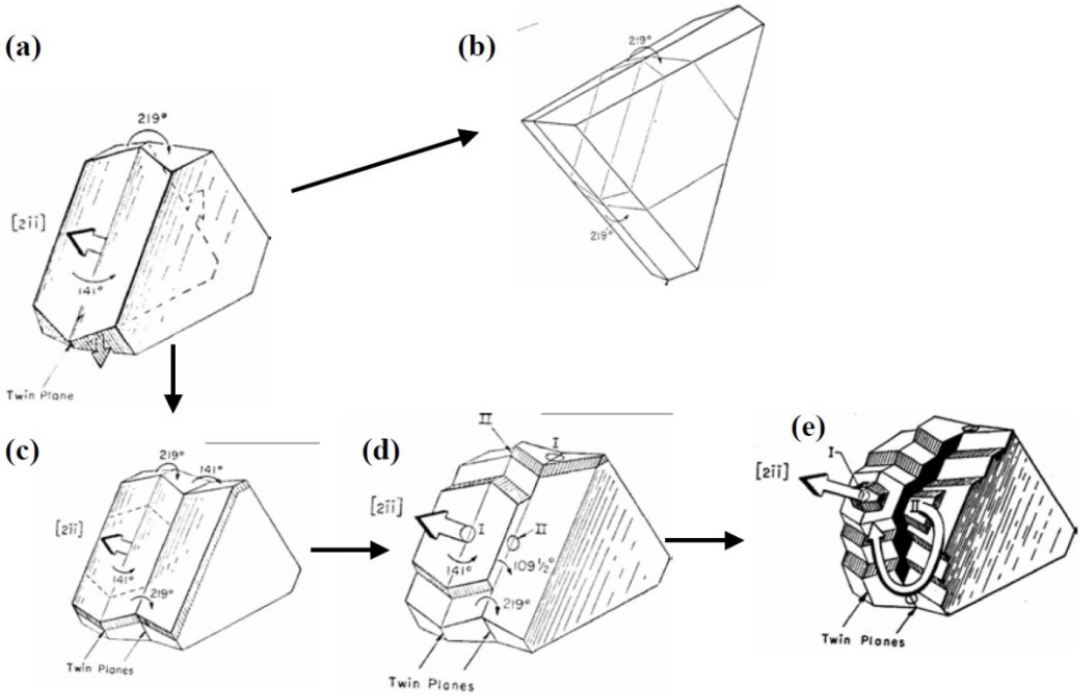

Figure 5. Twin Plane Re-entrant Edge Mechanism (a) Crystal with a single twin (b) Closure of twins due to ridge formation (c) Crystal with two twins (d) Creation of extra re-entrant corners I and II (e) Propagation of crystal due to re-entrant corners [24].

Thus, the presence of a re-entrant corner leads to rapid growth along the [211] direction. However, the rapid growth on the re-entrant corner stops when a trigonal solid that is bounded entirely by ridges is formed, Figure 5(b). However, if the crystal has two twins instead of one as shown in Figure 5(c), it will have six re-entrant corners located along the [211] direction. Growth on the re-entrant corners now generates more re-entrant corners as shown in Figure 5(d) and the newly generated re-entrant corners relieve the blockage of nucleation sites that is caused by the formation of ridges. Figure 5(e) shows a solid with several steps that are growing simultaneously by the re-entrant edge mechanism. Later it was experimentally verified that the TPRE mechanism is responsible for the growth of germanium dendrites and it was observed that all germanium dendrites invariably contain two or more twins and never a single twin.

Layer Growth Mechanism: Materials having high melting entropy such as Si tend to form atomically smooth, close packed interfaces. Thus any atom leaving the liquid and attaching itself to a flat solid surface increases the interfacial energy. Thus, the atom is likely to jump back into the liquid. However, if the interface contains ledges, liquid atoms will be easily able to join the solid without increasing the interfacial energy as shown in Figure 6.

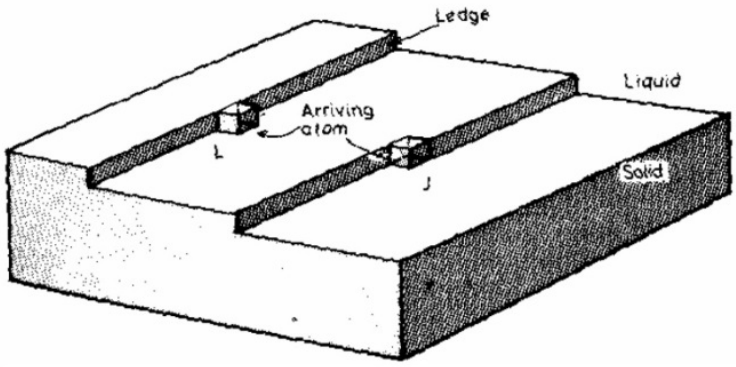

Figure 6. Layer growth mechanism of atomically smooth interfaces by formation of ledges [25].

It was suggested that Si in flake form grows predominantly by the layer growth mechanism. The average twin spacing was measured and it was found to be between 0.4 to 1.0 μm in slowly cooled specimens. It was observed that twin spacing is much larger than that would be expected from the TPRE mechanism. Moreover, microstructural analysis using TEM revealed that twins emerge on the non-faceted part of the Si crystal and do not form any re-entrant edges or grooves. Although the layer growth mechanism explains how growth proceeds once the ledges are formed, the nucleation of layers is very important and needs to be understood. One of the main sources for nucleation of new layers is screw dislocations. Studying the effect of screw dislocations in nucleating new layers and its interactions with re-entrant edges revealed that screw dislocations, which are prevalent in real crystals, should be accounted for when developing a growth mechanism for faceted crystals. Hence, four different cases based on the presence or absence of screw dislocations and twin junctions on the surface of a crystal were considered as they are depicted in figure 7 [22].

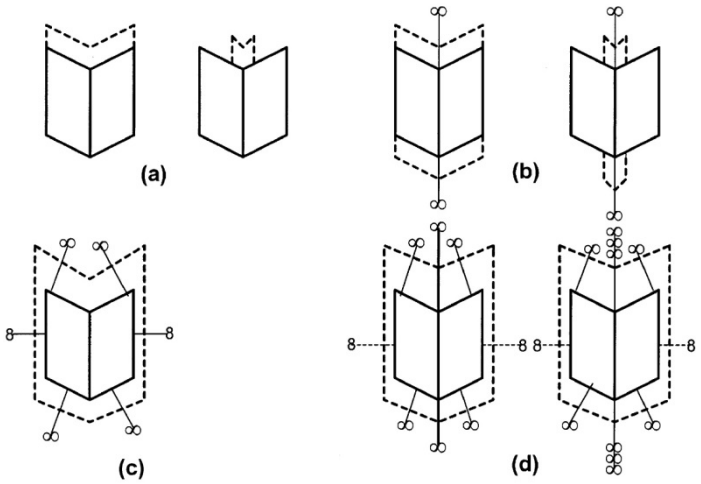

Figure 7. Hypothetical conditions of a screw dislocation and a re-entrant corner [22].

There are basically four preferable growth sites in a given faceted crystal; kinks, steps, re-entrant corners and surface nucleation. In the case depicted in Figure 7(a), there are no screw dislocations exposed on the surface neither at the twin junction nor at the crystal surface. Therefore the operative growth mechanism in this case is the TPRE mechanism. In the case depicted in Figure 7(b), a screw dislocation is exposed at a twin junction; the preferred growth occurs at the twin junction. In this case the crystal grows in both the forward and backward directions. In the case depicted in Figure 7(c), a screw dislocation is exposed on the surface of

the crystal. As screw dislocations initiate easy surface nucleation, growth occurs on all the crystal's surfaces uniforMLy, and the TPRE mechanism does not contribute to growth. The case presented in Figure 7(d), screw dislocations are exposed at both a twin junction and the crystal surface. In this case, growth of the crystal depends on the density of screw dislocations on the surface and at the twin junction. If the density of screw dislocations at the twin junction is higher than that at the crystal surface, growth will occur preferentially along the twin junction, and the resulting crystal will resemble those that grow by the TPRE mechanism.

1.2.2.2.2 Modification theories

Most recent theories explain the modification process as a result of restricted growth of Si by the impurity atoms present in the melt. However, within this type of theories there are different thoughts about how impurity atoms influence the growth of Si. A change in surface energy, poisoning of TPRE or growth ledges are some of the possible reasons which are proposed.

Surface Energy Theory: This theory attempted to explain chemical modification of the Al-Si eutectic based on the surface energy of the Al-Si solid interface. Although this theory is one of the widely accepted theories for quench modification, there are still many debates supporting chemical modification [26]. A decrease in surface energy of the Al-Si solid interface upon the addition of the chemical modifier increases the interface angle θ as shown in Figure 8.

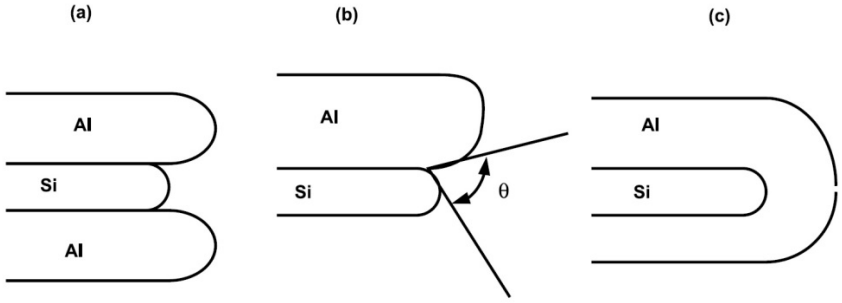

Figure 8. Eutectic solidification in sodium modified Al–Si alloys [22].

This in turn suppresses growth of the Si crystal and causes modification of the eutectic structure and under-cooling. It was later proved that addition of sodium decreases the surface tension of the eutectic liquid. In order to study the effect of this change in surface tension on the interfacial angles, an Al-Si eutectic alloy was grown on a polycrystalline Si substrate with and without sodium atmosphere. Although no change in the presence of sodium was recorded, the clear difference between surface tensions is not negligible and the significance of this is still debated [22].

Interfacial poisoning theories: These theories explain chemical modification in a way that impurity atoms (Na, Sr, etc.) poison the growth sites of Si as the interface starts to advance. Among the theories which believe interfacial poisoning of Si at the interface causes the decrease in growth rate of Si, there are two different trains of thought. It is suggested that modifier atoms poisoning the re-entrant edges supposedly stop the growth by the TPRE mechanism [22].

TPRE Poisoning: One group of researchers believes that interfacial poisoning of re-entrant edges of TPRE mechanism by modifier atoms is responsible for modification. The typical growth of Si is in a zig-zig fashion. Study of electron diffraction patterns of the fibers revealed the growth mechanism, which is shown schematically in Figure 9. The AB twins in the left

bottom of the figure lead to branching in the form of BC twins through multiple twinning. Further AB twins are in the [112] direction, while the BC twins are in [112] directions.

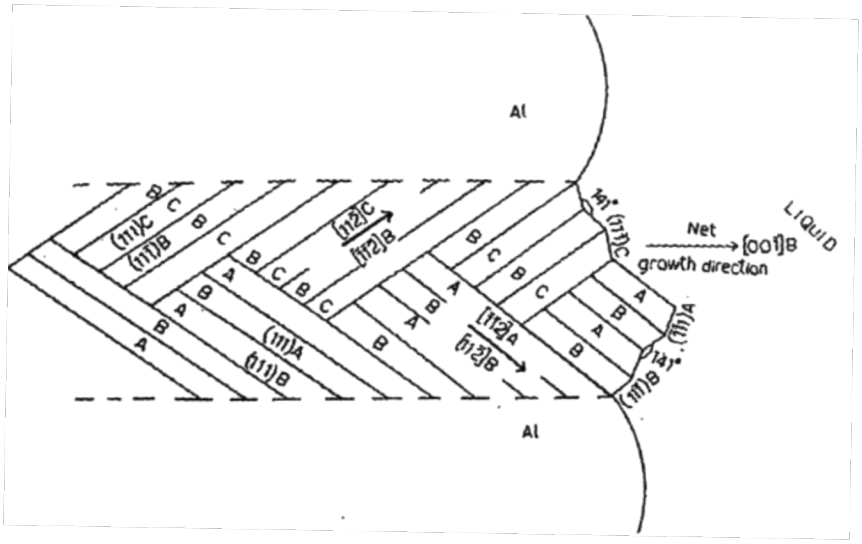

Figure 9. Schematic diagram of twins and their growth directions in a modified Si fiber [22].

Because of the impurity atom poisoning, the fiber changes its direction by multiple twinning, often resulting in coral type morphology. This hypothesis of the TPRE poisoning mechanism does not exactly predict how the poisoning of re-entrant edges takes place and what characteristics determine whether an element can act as a modifier [22].

Impurity Induced Twinning: In this theory, interfacial poisoning takes place by poisoning the growing ledges of Si. The impurity atoms such as Na or Sr can act as a poison to already growing atomic layers. The impurities are assumed to adsorb on the step or kink sites, thus preventing attachment of atoms or molecules to the crystal as shown in Figure 10. These poisoning atoms could induce twinning by altering the stacking sequence of atomic layers in order to grow around the impurity [27].

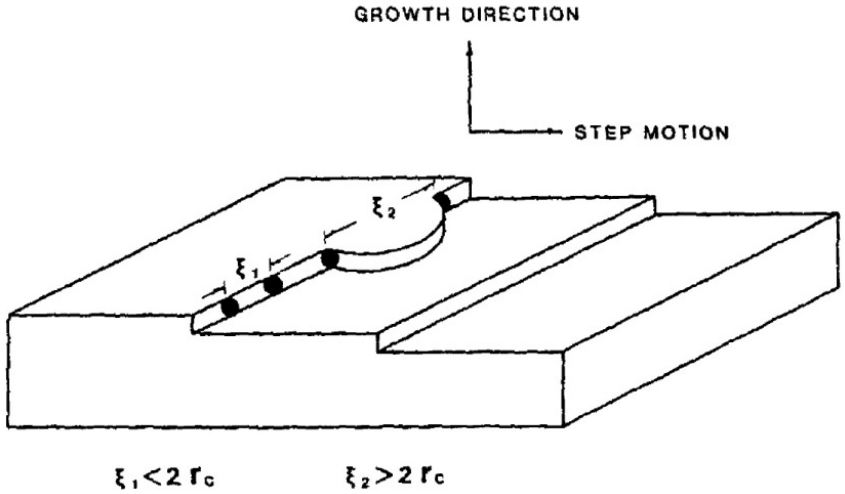

Figure 10. Schematic view of impurity atoms pinning the steps of a Si crystal growing by the layer growth mechanism at the solid/liquid interface [27].

1.3 MECHANICAL PROPERTIES AT ROOM AND ELEVATED TEMPERATURE

1.3.1 Deformation mechanisms

Inelastic deformation occurs in metals due to slip, climb or twinning .When the temperature is less than approximately 0.5 T_M (T_M is absolute melting temperature), deform occurs primarily due to propagation of dislocations through the lattice. This results in the slip of one segment of crystal relative to another crystal segment. At higher temperatures deformation by dislocation climb, a diffusion-controlled process, become more important. Twinning, a rotation of atoms in the lattice structure, takes place in crystals that do not easily permit slip deformation. Twinning is of secondary importance since the resulting strains are very small compared to slip and climb [28]. These three types of deformation mechanisms are introduced in what follows.

1.3.1.1 Slip of dislocations

A perfect defect free crystal could endure stresses much higher than those commonly observed for yield and plastic flow in metals. In ideal crystals, plastic flow results from sliding one plane of atoms over another by simultaneous breaking of all the metallic bonds between the atoms. However, the actual yield stress is much lower than the theoretical shear stress, due to the presence of dislocation in lattice structures. As it is depicted in Figure 11, an edge dislocation is an extra plane of atoms in crystals lattice. Accordingly, the crystal is deformed along the line where the extra plane terminates. When a shear stress is applied to the crystal lattice, the atoms in a continuous plane next to the edge of the extra plane may move from their current bonds and form new bonds with the atoms on the edge of the extra plane. As a result, the extra plane moves one atomic distance along the continuous plane. Application of the stress may actually cause the dislocation to move several steps along the slip plane in the crystal lattice [28].

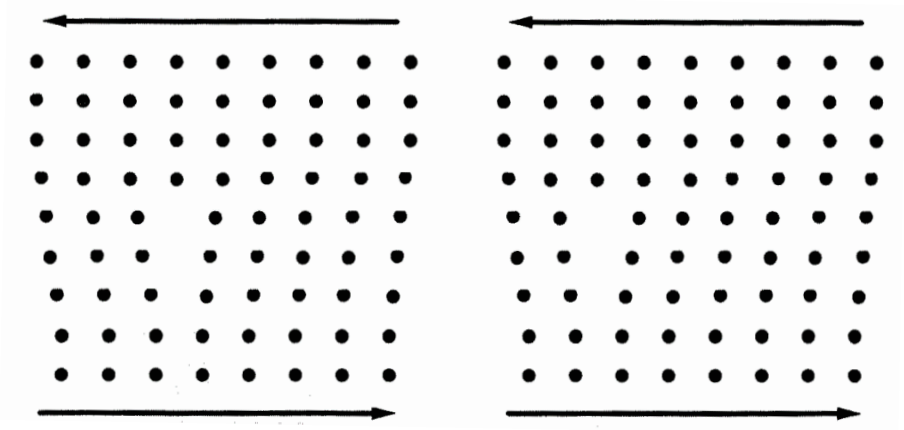

Figure 11. Propagation of an edge dislocation through a crystal lattice [28].

The slip planes and slip direction in metals depends on the crystal structure of the metal. Slip often occurs on planes of high atomic density in a closely packed direction, where the distances between atoms are a minimum. Al has the FCC structure; the close packed direction and plane are illustrated in Figure 12. However slip is observed in a non-close packed direction on the octahedral plane, and on the cube plane at high temperature [28].

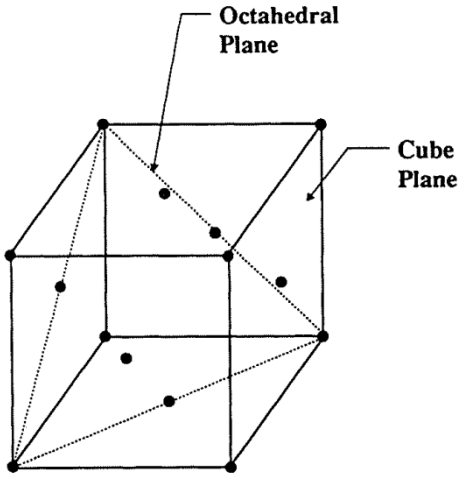

Figure 12. Unit cell of face-centered cubic (FCC) structure and different slip planes [28].

1.3.1.2 Dislocation climb

An edge dislocation generally propagates in the slip plane, but under special conditions it can move in a direction perpendicular to the slip plane. Dislocation climb occurs by the diffusion of atoms and vacancies towards or away from the site of the dislocation. As it is depicted in Figure 13, positive climb takes place when atoms are removed from the dislocation plane by the diffusion of an atom to a vacant lattice site and hence results in moving up of the dislocation one lattice distance. In negative climb, atoms are added and the dislocation moves down one lattice distance [28].

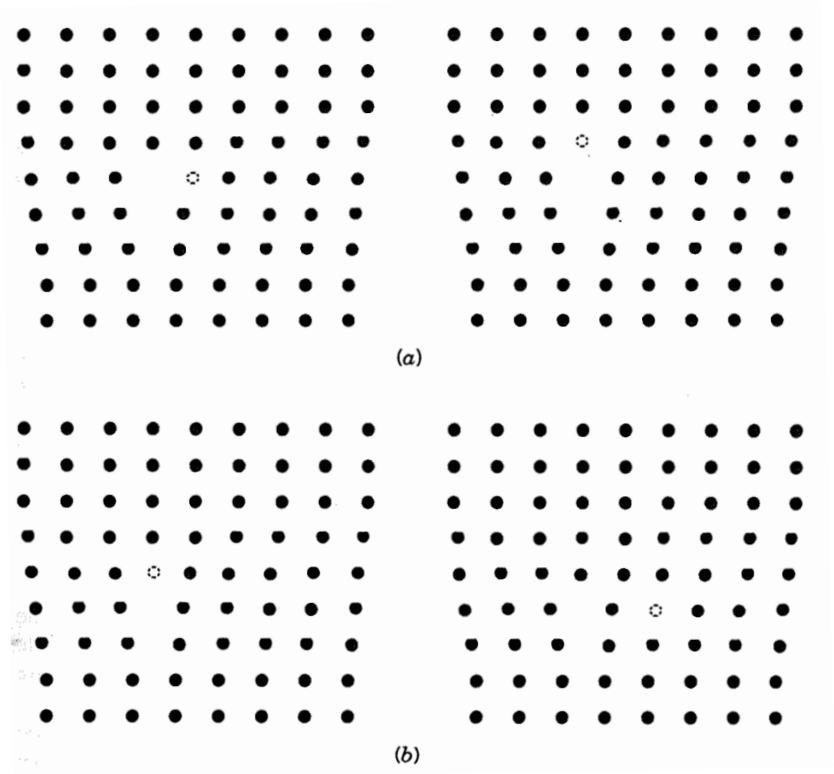

Figure 13 Schematic diagram showing (a) positive and (b) negative dislocation climb resulting from the diffusion of atoms or vacancies to or from an edge dislocation [28].

The importance of dislocation climb increases with increasing temperature because climb is a diffusion process. As the temperature increases the potential for climb increases and the potential for slip decreases [28].

1.3.2 Tensile properties and dislocations

Generally speaking, for Al alloys room temperature falls in a range below than $0.3T_m$ [29]. In this region the deformation mechanism is usually slip; although twinning and kinking may also occur. Slip is adequately described by the movement of dislocations through the crystals. Deformation begins when the applied stress is great enough to activate dislocation sources and stops only if the back stress from dislocations piled up at obstructions exceeds the applied stress. Obviously, there are two approaches to increasing strength; firstly locking possible dislocation sources, and secondly providing dispersed obstructions to dislocation motion [29].
Increasing temperature generally has the following effects on stress-strain curves [30, 31]:

- Increasing ductility and toughness
- Lowering the yield stress and modulus of elasticity

Temperature also affects the strain hardening exponent of most metals. The movement of dislocations through a lattice is aided by thermal vibration. Consequently resistance to slip increases as the temperature falls. The resistance to the movement of a dislocation along a slip plane is measured by the Peierls force and one theory at least places the reason for increased strength at low temperatures firmly on the increase in Peierls force. There are alternative possibilities to explain this increase in resistance to slip, termed lattice friction stress, such as the greater difficulty of moving jogged dislocations through the lattice. Whatever the reason for this behaviour, one thing is certain, that FCC metals are less influenced by low temperatures than are BCC metals [30, 31].

The strength of Al alloys decreases with an increase in temperature, excluding any effects of age-hardening within narrow temperature ranges for various holding periods. Shear, compression, bearing and fatigue strengths vary with temperature in much the same way as tensile strength; ratios of these strengths to tensile strength may be taken as constant. The modulus of elasticity of Al alloys also decreases as the operating temperature increases. The modulus of elasticity is determined by the binding forces between atoms. Increasing temperature decreases these binding forces and consequently decreases modulus of elasticity[31].

1.4 MODELLING THE DEFORMATION BEHAVIOR OF AL ALLOYS

1.4.1 The empirical vs. physical models

There are different empirical models which describe the inelastic behavior of materials. The most well-known models are based on power-law models [32, 33] where plastic strain varies as a power of applied stress. These empirical models are primarily derived from curve-fitting and their validity at different temperatures and strain rates is quite limited. Although there are a few hardening models that can be obtained from empirical models and models based on dislocation mechanisms (e.g. power law creep [34]), not considering the underlying physical process restricts their range of validity [35].

In the models based on physics of material, the underlying physical process, dislocation processes, etc. are used to formulate constitutive equations [35]. Dislocation densities are the

microstructural variables that govern the properties [36] and provide an understanding about physics of the material [35]. Change in density of immobile dislocation is related to slip system and the thermally activated annihilation by the climb of the dislocations. The immobilization rate of mobile dislocations is a function of microstructure, strain rate and temperature. The recovery process occurs with climb [36] and glide of dislocations [37]. The diffusion of vacancies, which usually takes place at elevated temperature, is a dominant factor in the recovery process of dislocations. The high concentration of vacancies near grain boundaries enhances creep controlled by dislocation glide and climb processes [38].

Lindgren et al. [35] proposed a dislocation density model in order to describe the plasticity of an austenitic stainless steel. This model was subsequently employed by others in order to describe plastic deformation and flow stress behavior of Ti-6Al-4V [39] and Al-5Mg alloy [40] at different exposure temperatures. The model describes hardening/softening behavior of the material based on dislocation density and excess vacancies. The modelling defines the flow curves of the material explicitly.

1.4.2 Evolution of flow stress model

According to the work by Bergström [41] and Kocks [42], the flow stress is assumed to consist of two major components, (equation 1):

$$\sigma_y = \sigma^* + \sigma_G \qquad (1)$$

where σ^* is the stress needed to overcome short range barriers and is thermally activated, σ_G is the athermal stress contribution from the long-range interactions of the dislocation substructure which cannot be assisted by thermal vibrations.

1.4.2.1 Short range flow stress

The strength of obstacles, which a dislocation meets during movement, determines the dependency of flow strength on applied strain rate ($\dot{\bar{\varepsilon}}^p$). The dislocation velocity is related to plastic strain rate through the Orowan equation, equation 2:

$$\dot{\bar{\varepsilon}}^p = \frac{\rho_m b \bar{v}}{m} \qquad (2)$$

where $\bar{v}$ is the average velocity of mobile dislocations (ϱ_m) having a density of ϱ_m, b and m are the Burgers vector and Taylor's factor respectively. The velocity is considered during the time taken by a dislocation to pass an obstacle where the most of it, is the waiting time. The velocity is written according to Frost and Ashby [43] as equation 3:

$$\bar{v} = \Lambda \upsilon_a \exp\left(-\frac{\Delta G}{kT}\right) \qquad (3)$$

where Λ is the mean free path of dislocations between two obstacles, ν_a is the attempt frequency which depends on characteristics of the obstacles, ΔG is the activation energy, k is Boltzmann's constant and T is the temperature. Replacing the average velocity in equation (2) leads to the following equation, equation (4):

$$\dot{\bar{\varepsilon}}^p = \frac{\rho_m \Lambda b \nu_a}{m} \exp\left(-\frac{\Delta G}{kT}\right) \qquad (4)$$

Since a specific amount of activation energy is required for a dislocation in order to pass a barrier, the motion of a dislocation is facilitated by activation energy. The form of the ΔG function depends on the applied stress and strength of the obstacles. Different shapes of barrier energy distribution results in different constitutive equations. A generalised equation for these shapes was proposed by Kocks et al. [44], see equation (5):

$$\Delta G = \Delta F\left[1-\left(\frac{\sigma^*}{\sigma_{ath}}\right)^p\right]^q \qquad (5)$$

Here, $\Delta F = \Delta f_0 Gb^3$ is the required activation energy to overcome lattice resistance in the absence of any external force, $\sigma_{ath} = \tau_0 G$ is the athermal flow stress meaning the stress level required to be exceeded in order to move dislocations across the lattice without the aid of thermal energy. The exponents $0 < p \leq 1$ and $0 < q \leq 2$ are concerned with shape of the energy barriers. According to Frost and Ashby [45], the pre-exponential term in equation (4) is constant to a first approximation and termed as the reference strain rate, $\dot{\bar{\varepsilon}}^{ref}$. Combining the equations (4) and (5), the first term in equation (1) which is the strain rate-dependent part of the yield strength and the short-range stress component, is written as [42, 43, 46] equation (6):

$$\sigma^* = \tau_0 G\left\{1-\left[\frac{kT}{\Delta f_0 Gb^3}\ln\left(\frac{\dot{\bar{\varepsilon}}^{ref}}{\dot{\bar{\varepsilon}}^{pl}}\right)\right]^{1/q}\right\}^{1/p} \qquad (6)$$

1.4.2.2 Long range flow stress

The long-range barriers are due to interactions with the dislocation substructure and are related to the immobile dislocation density. Seeger assumed that the number of dislocations intersecting a unit area is ϱ, the the mean distance between dislocations is $\varrho^{-0.5}$. The term related to long-range barriers, σ_G, in equation (1) is expressed as equation (7) [47]:

$$\sigma_G = m\alpha Gb\sqrt{\rho_i} \qquad (7)$$

where m is the Taylor orientation factor which is a texture affected parameter, which expresses the effects of resolved shear stress in different slip systems into effective stress-strain relations. a is a proportionality lattice parameter, ϱ_i is the immobile dislocation density, G is a temperature dependent shear modulus (computed from the elastic modulus, E, and Poisson ratio v), and b is the Burgers vector. The mobile dislocation density is assumed to be much smaller than the immobile according to Bergström [48] and Estrin [49]. The presented model only considers the density of immobile dislocations ϱ_i which consist of hardening (+) and recovery (-) terms, see equation 8.

$$\dot{\rho}_i = \dot{\rho}_i^{(+)} - \dot{\rho}_i^{(-)} \qquad (8)$$

Unlike BCC materials, the flow stress of fcc materials (such as Al) become strain rate dependant at elevated temperature [50]. The mobile dislocations move a distance, called the mean free path (Λ) before they become immobilized or annihilated, and then turn into immobile dislocations in the next cell. Hence, it is important to interpret the role of thermal

barriers during hardening (term $\dot{\rho}_i^{(+)}$ in equation 8) in order to build the flow curves. The density of immobile dislocations and their average velocity are proportional to the plastic strain rate [49], see equation 9.

$$\dot{\rho}_i^{(+)} = \frac{m}{b}\frac{1}{\Lambda}\dot{\bar{\varepsilon}}^p \qquad (9)$$

where m is the Taylor orientation factor used for polycrystalline metals. The mean free path (Λ) for the material in this study was obtained from the SDAS (λ) and dislocation sub-cell diameter (s) [35] through equation 10:

$$\frac{1}{\Lambda} = \frac{1}{\lambda} + \frac{1}{s} \qquad (10)$$

In this study, the formation and evolution of sub-cells is modelled using the following relation where K_c is a calibration parameter depending on temperature, see equation 11.

$$s = K_c \frac{1}{\sqrt{\rho_i}} \qquad (11)$$

The dislocation density is reduced during the recovery process due to glide and climb of dislocations. The term which is controlled by climb is proportional to the current dislocation density and the plastic strain rate, and is formulated as equation 12 [51]:

$$\dot{\rho}_{i\,(glide)}^{(-)} = \Omega\rho_i\dot{\bar{\varepsilon}}^p \qquad (12)$$

where Ω is a recovery function that depends on temperature and strain rate. This equation takes only dynamic recovery into consideration due to the strain rate. Static recovery, however, is controlled by diffusion climb having the following formulation in equation 13 [52]:

$$\dot{\rho}_{i\,(c\lim b)}^{(-)} = 2c_\gamma D_v \frac{c_v}{c_v^{eq}}\frac{Gb^3}{kT}\left(\rho_i^2 - \rho_{eq}^2\right) \qquad (13)$$

where c_v^{eq} and c_v are the equilibrium and current vacancy concentrations, and c_γ is a calibration parameter related to the stacking-fault energy. Since c_v^{eq} is the corresponding value for a pure metal, a scale factor is multiplied in order to correct the vacancy concentration ratio considering the interaction of major alloying elements with vacancies. Jarfors [53] used the following scale factor according to Lomer [54] in the study on Al-Si alloys, see equation 14:

$$\frac{X_{vac}^{Al-Si}}{X_{vac}^{Al}} = 1 - ZX_{Si} + ZX_{Si}\exp\left(\frac{E}{kT}\right) \qquad (14)$$

where Z is the coordination number, X_{si} is concentration of solute, E (J) is the vacancy-solute binary interaction energy and k (J K^{-1}) is Boltzmann's constant. Concentration of solute in the

matrix (X_{si}) was measured using the WDS technique. X_{si} and Z are given the following values respectively; 0.015, 12.

The dislocation density decreases towards an equilibrium value of ϱ_{eg}. The self-diffusion coefficient, D_v, is derived using equation 15 [55]

$$D_v = a^2 \upsilon_a e^{\frac{\Delta S_{vm}+\Delta S_{vf}}{k}} e^{-\frac{Q_{vm}+Q_{vf}}{kT}} = D_{v0} e^{-\frac{Q_v}{kT}} \quad (15)$$

where ΔS_{vm} is the increase in entropy due to vacancy motion, ΔS_{vf} is the increase in entropy when a vacancy forms, Q_{vm} is the energy barrier for vacancy motion and Q_{vf} is the activation energy of vacancy formation.

In order to solve equation (15), the vacancy concentration needs to be calculated. The generation and motion of vacancies are coupled with the recovery of dislocations and diffusion of solute atoms. In FCC metals, the concentration of strain-induced vacancy is significant due to their low diffusivities. A model for excess vacancy concentration with generation and annihilation components has been proposed by Militzer *et al* [52]. In the present model, it is assumed that only long-range stress contributes to vacancy formation and only mono-vacancies are concerned. When a crystal is held for a sufficient time at a given temperature, an equilibrium level of vacancies is reached. Deforming the material or changing the temperature generates excess vacancies. The effect of excess vacancies on diffusion is taken into account through (15) as equation 16:

$$\dot{c}_v^{ex} = \dot{c}_v - \dot{c}_v^{eq} = \left(\chi \frac{\sigma_y b}{Q_{vf}} + \varsigma \frac{c_j}{4b^2} \right) \frac{\Omega_0}{b} \dot{\bar{\varepsilon}}^p - D_{vm} \left(\frac{1}{s^2} + \frac{1}{\lambda^2} \right) \left(c_v - c_v^{eq} \right) \quad (16)$$

where the factor χ is the fraction of mechanical work needed for the vacancy formation, Q_{vf} is the activation energy for forming a vacancy, Ω_0 is the atomic volume and c_j is the concentration of thermal jogs. The parameter ς describes the neutralisation effect by vacancy emitting and absorbing jogs, c_v^{eq} is the equilibrium concentration of vacancies at a given temperature, c_v is the non-equilibrium vacancy concentration and D_{vm} is the vacancy migration. The stress σ_y is equal to the flow stress during a plastic deformation. Eventually, in order to update the flow curves evolution for arbitrary paths, a radial return algorithm is employed. Details about the stress update algorithm are shown in Lindgren *et al* (2008) [35].

CHAPTER 2

RESEARCH APPROACH

CHAPTER INTRODUCTION

This chapter describes the research methodology used in this thesis. The purpose and aim of the work are first described. It is then followed by elaborating the research activity and methodology.

2.1 PURPOSE AND AIM

The usage of Al-Si based cast alloys are currently increasing. The microstructural constituents have a marked contribution in the strengthening of these alloys. Their exclusive contribution to the strength of the alloys at different working temperature however has not been exclusively mapped. The aim of this work is to expand understanding of the effect of the size and morphology of the microstructural constituents (e.g. SDAS, eutectic Si-particles and intermetallic phases) on tensile properties of Al-Si cast alloys at different temperatures (room temperature up to 500 ºC). As a result, adapting and developing a physically based model which enables prediction of the flow stress behaviour of these alloys comprising different microstructures. The model can be employed in FEMs simulation of the behaviour of cast components at different working temperatures.

2.2 RESEARCH DESIGN

2.2.1 Research approach

There are two major traditions of research approach based on different reasoning fashions; the interpretivist and positivist approaches [56]. In the former the reasoning is inductive and in the latter is deductive. The inductive reasoning starts from a specific observation towards a general law, while in the deductive reasoning the discussion moves from general principles to specific cases.

The research approach of this study is structured according to deductive reasoning. The flow chart of the research approach of this study is shown in Figure 14. The present work started by defining the topic of interest according to real industrial problems concerning the parameters that influence the performance of the Al-Si casting alloy in a cast component. The effort has been made in order to investigate the potential for improvement in mechanical properties of the alloy. Hence, the role of microstructure on deformation behaviour of these alloys at different temperatures was investigated. A physics based model was adapted and improved, enabling prediction of the flow stress curves of EN AC-46000 alloy at different temperatures with various microstructures. Prior to each research phase, a comprehensive

literature survey is done on the selected topics to collect relevant information and data in relevant works. The online resources (primarily Scopus, ScienceDirect and SpringerLink) were used. The survey provided us better understanding about the lack of knowledge in this field of science and also helped us to identify the possibilities and challenges. Furthermore, the theoretical framework and variables are defined. Prior to designing the experiments, in a separate study, the validity and reliability of our experimental set-up which has been employed during our research was evaluated. Then, the experimental routine was designed according to the scopes and variables in a way to understand the cause and effect of desired variables. The obtained results were collected, evaluated, analysed and compared with data available in the literature. The conclusions were made drawing on the obtained results and outcome of other researches.

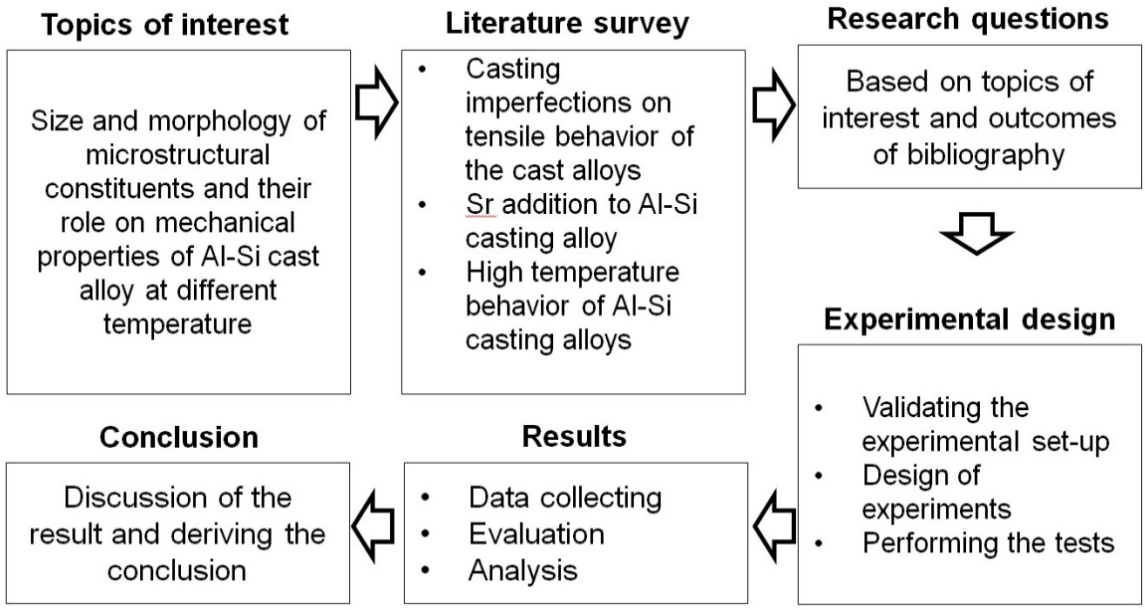

Figure 14 Schematic illustration of the research approach of the present work.

The present research comprises four major topics:

- An investigation on HPDC automotive component of Al-Si alloy; Finding the typical casting defects in the component and find the relation with the performance of the alloy with the defects. To employ and validate a manufacturing technique (gradient solidification technique) in order to minimize the influence of casting uncertainties.
- Sr addition to the EN AC-46000 cast alloy; to study the role of Si modification on porosity formation, microstructure and mechanical properties of the alloy. Find an appropriate tool to assess the modification level (ML) and to predict the optimum Sr level in Al-Si cast alloy.
- High temperature deformation behaviour of EN AC-46000 alloy; to study the role of cooling rate on microstructure and tensile properties of EN AC-46000 at room and elevated temperature.
- Modelling the tensile behaviour of EN AC-46000 alloy; to adapt and improve a physically-based constitutive model that enables the prediction of flow stress behaviour of EN AC-46000 alloy at ambient and elevated temperature for various microstructures.

2.2.2 Research questions

Several research questions have been raised and answered during each phase of this study. The main questions can be categorized in five main areas and are addressed in the indicated supplements:

- **Casting defects and mechanical properties (Supplement I & II)**
  - Which types of casting defects are predominant in the HPDC component? (Supplement I)
  - To which extent the casting defects may harm the tensile properties of the alloy? (Supplement I)
  - How the level of these uncertainties can be minimized in order to study solely the role of other parameters (e.g. microstructure)? (Supplement I)
  - Is Sr-modification associated with pore formation during casting? (Supplement II)

- **Sr modification (Supplement I & II & III)**
  - What is the effect of Sr-modification on microstructure of Al-Si based cast alloys with different cooling rate? (Supplement I & II)
  - What is the most appropriate approach in order to assess the level of modification and predict the optimum Sr content in the alloy? (Supplement II & III)
  - Can Sr addition change the failure mode of Al-Si-Cu-Mg casting alloys? (Supplement I & II)

- **Microstructure and mechanical properties (Supplement I & II & IV)**
  - What is the effect of cooling rate on tensile properties of Al-Si-Cu-Mg casting alloys? (Supplement II & IV)
  - Do refined Si-particles guarantee an improvement in mechanical properties of Al-Si-Cu-Mg casting alloys? (Supplement I & II)

- **High temperature behaviour** (Supplement IV & V)
  - What is the evolution of matrix and particles upon exposure to elevated temperature? (Supplement IV)
  - What is the effect of strain rate on deformation behaviour of Al-Si-Cu-Mg casting alloys at different temperature? (Supplement IV & V)
  - What is the effect of microstructural coarseness on failure process of AL-Si-Cu-Mg cast alloys at elevated temperature? (Supplement IV)

- **Modelling the tensile behaviour** (Supplement V)
  - Is it possible to predict the flow stress behaviour of EN AC-46000 cast alloys at different temperatures based on underlying physics of the material? (Supplement V)
  - Does the model have validity for different as-cast microstructures? (Supplement V)

2.3 MATERIAL AND EXPERIMENTAL PROCEDURE

2.3.1 Materials

2.3.1.1 The alloys

Two distinctive Al-Si based alloy systems were investigated in present work with distinctive properties for different applications. The chemical composition of the alloys is summarized in Table 1.

Table 1. Chemical compositions of the alloys (wt.%).

	Si	Cu	Mg	Fe	Zn	Mn	Al
EN AC-44300	12	0.1	0.02	0.7	0.1	0.1	Bal.
EN AC-46000	8-10	2.0-2.6	0.26	0.8	0.9	0.2	Bal.

The ingots of the alloy were melted in a 10-kW resistance furnace with a Si carbide bonded graphite crucible at 730°C. Cylindrical rods (length 20 cm, diameter 1 cm) were cast in a permanent copper mold. In order to investigate the effect of Sr-modification, another melts of each alloy were prepared with different Sr level (up to 486 ppm), using Al-10%Sr master alloy. The addition was carried out by placing Al-10%Sr master alloy piece on the melt surface and twenty minutes was allowed for dissolution of strontium. Chemical composition of each sample was obtained by optical emission spectroscopy. The EN AC-46000 alloy and EN AC-44300 were modified by five and two different Sr levels respectively. The chemical composition of the prepared alloys is provided in
Table 2.

Table 2. Chemical compositions of EN AC-46000 and EN AC-44300 with different Sr content (wt. % except for Sr ppm).

		Si	Cu	Mg	Fe	Zn	Mn	Sr	Al
EN AC-46000	**Alloy 1**	8.02	2.11	0.26	0.78	0.99	0.17	**0**	Bal.
	Alloy 2	8.02	1.89	0.26	0.92	1.03	0.21	**37**	Bal.
	Alloy 3	8.05	1.90	0.26	0.91	1.05	0.21	**68**	Bal.
	Alloy 4	8.10	2.02	0.25	0.90	0.96	0.24	**150**	Bal.
	Alloy 5	8.30	1.99	0.27	0.98	1.06	0.21	**276**	Bal.
	Alloy 6	8.21	1.95	0.27	0.98	1.07	0.21	**486**	Bal.
EN AC-44300	**Alloy 1**	11.99	0.2	0.26	0.69	0.99	0.17	**0**	Bal.
	Alloy 2	11.78	0.1	0.26	0.61	1.03	0.19	**90**	Bal.
	Alloy 3	11.67	0.1	0.26	0.56	1.05	0.21	**165**	Bal.

The alloys used for high temperature study was also from EN AC-46000 family alloy with minor difference in level of Si and Cu. It was additionally modified with 480 ppm Sr. The chemical composition is summarized in Table 3.

Table 3. Chemical compositions of the alloy used for high temperature studies (wt. % except for Sr ppm).

Si	Cu	Mg	Fe	Zn	Mn	Sr	Al
10.0	2.6	0.24	0.8	0.8	0.26	**0** and **480**	Bal.

2.3.1.2 The component

The casting that has been studied is a structural automotive component, Figure 15. The component in its application is subjected to cyclic torsion load. The studied component is manufactured by HPDC using the commercial EN AC-44300. The chemical composition of cast component is presented as Alloy 1 in
Table 2, measured by optical emission spectroscopy, SPECTROMAX.

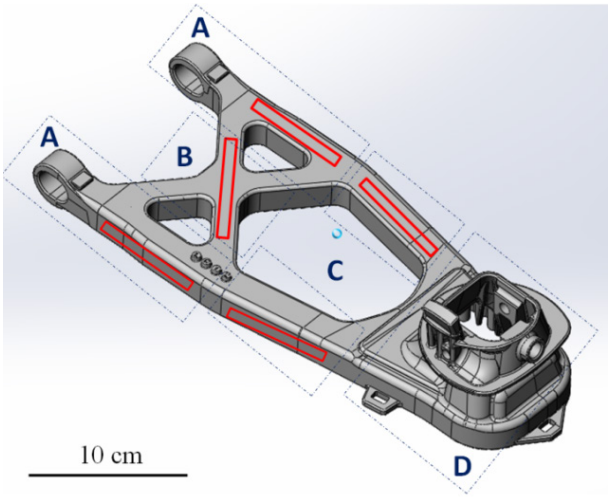

Figure 15. CAD configuration of the component.

2.3.2 Casting

2.3.2.1 The gradient solidification technique

Initial cylindrical rods (length 20 cm, diameter 1 cm) were cast in a permanent copper mold. The cast rods were then re-melted and heated to 710°C for 20 minutes under Ar-atmosphere and subsequently solidified using the gradient solidification technique. The gradient solidification set-up enables the generation of well-fed and homogenous material, with low levels of oxides, shrinkage- and gas-porosity over the entire length of sample. Varying the pulling rate of the furnace let us control the scale of the microstructure to generate desired microstructure. In order to produce defect free samples with a microstructure scale similar to the high pressure die casting (HPDC), die casting and sand casting process, the pulling rate of the furnace was set to 3, 0.3 and 0.03 $mm.s^{-1}$ respectively. Average secondary dendrite arm spacings (SDAS) of 10, 25 and 50 μm respectively were obtained. Water was used as the cooling media beneath the furnace for the pulling rate of 3 and 0.3 $mm.s^{-1}$ while air was the cooling media corresponding to pulling rate 0.03 $mm.s^{-1}$.

2.3.2.2 Controlled-cooling rate casting

In order to assess the level of modification under different cooling rates, a casting set-up with reordered thermal history was designed. Three cylindrical steel molds with same geometry (Figure 16) encased in a steel box, ceramic box and a fiberglass insulation box respectively. They yielded three different cooling rates during solidification. The prepared melt was poured into the molds which were preheated to 700°C and the temperature was read by K-type thermocouples (Ni-Cr-Ni) located at two positions of mold wall and mold center, both at mid-height. The schematic view and dimensions of the mold set-up is demonstrated in Figure 16.

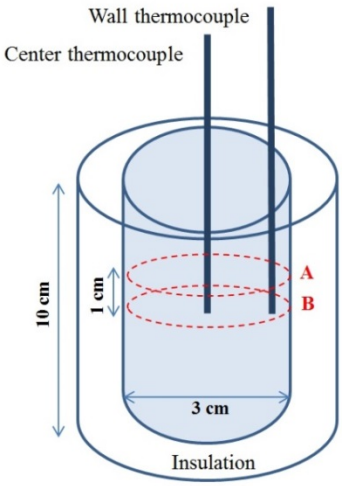

Figure 16. The schematic view of the mold set-up for controlled cooling rate casting.

The temperature-time data was collected via a high-speed data acquisition system logged on a computer through a commercials interface which recorded temperature every 0.01 second. In order to allow a good comparison of results for each alloy, the same thermocouples were used for all tests. This was achieved by placing the thermocouples inside in a 1 mm diameter stainless steel sheath which allows removing the thermocouple from solidified samples. The dash lines show the locations that the samples for the purpose of metallographic study were prepared.

2.3.3 Sample preparation

2.3.3.1 Tensile test specimens

Two types of tensile specimens were prepared; flat and cylindrical. The cylindrical tensile test bars were produced out of the directionally solidified rods and the flat tensile test bars were extracted from different locations of the components (as is illustrated in Figure 15 with solid red line) and prepared according to ASTM B557M-10 [10]. The geometry and dimensions of the specimen are presented in Figure 17.

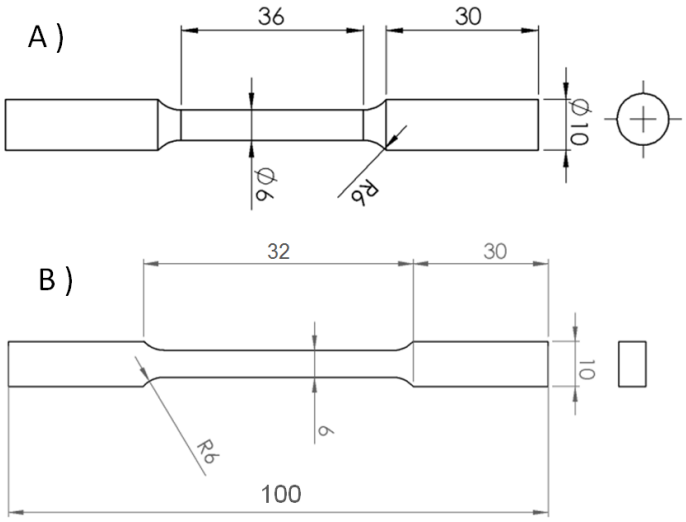

Figure 17. Geometry and dimensions of the standard A) Round and B) Flat tensile specimens used in this study. All values presented in mm.

2.3.3.2 Specimens for microscopic analysis

The as-cast samples and tensile-tested specimens were mounted horizontal and parallel to the tensile axis and then ground and polished to the centre of the cylindrical bar. Size, morphology and distribution of fractured particles were examined by optical microscopy and then quantitatively assessed using a Stream Motion Image Analyser. A STRUERS polishing machine, polishing clothes and lubricants were used for the metallographic preparation. The lubricants used were water, diamond particles (DP) and silica (OPS) suspended in water based solution. Different polishing recipes were used for preparation of the OM and WDS/EBSD samples. The details of the grinding and polishing steps are summarized in Table 4.

Table 4. Details of grinding and polishing steps of OP and (WDS/EBSD) samples.

	Type	Lubricant	Time (min)	Force (N)
Grit SiC paper	P320	Water	Till reaching the desired thickness	30
	P800	Water	1 (1)	25
	P1200	Water	2 (2)	25
Polishing pad	LARGO	DP 9 μm	3 (3)	20
	MOL	DP 3 μm	3 (5)	15
	NAP	DP 1 μm	5 (7)	10
	CHEM	OP-S 0.04 μm	5(15)	5
	CHEM	OP-AN 0.02 μm	- (15)	5

2.3.4 Tensile testing

Tensile tests were carried out using a Zwick/Roell Z100 testing machine, at different temperatures; from room temperature up to 500 ºC. In the study of high temperature deformation, the strain rates were varied from 10^{-4} to 10^{-1} in 4 levels. A wide temperature range from room temperature up to immediately below the solidus temperature was chosen in order to describe the behaviour of the alloy at any plausible working temperature. Besides, experimental data are aimed to be used to define a model on deformation behaviour of the alloy. The upper limit of the strain rate, 10^{-1}, was selected due to the intrinsic limited ductility of the alloy according to literatures, especially at temperatures below 0.5 Tm. The lower limit, 10^{-4}, was selected to avoid creep-like deformation of the alloy. In order to have statistical significance in the results, at least four replicas for each case were performed. The Zwick/Roell system has a reliable control of temperature through a built-in resistance furnace (with 3 built-in thermocouples), and tensile strain measured through a laser extensometer. The tensile test was conducted immediately after casting the specimen in order to exclude any aging effect on the results. In order to have statistical significance in the results, at least four replicates for each case were performed. Prior to tensile testing, the specimens were heated up to the pre-set temperature and held for 15 minutes to homogenize. Flow curves, the maximum stress value (R_m), the stress at 0.2% offset strain ($R_{p0.2}$), the strain at which failure occurs (ε_F) on the stress-strain curve were derived from the data acquisition system of the machine.

2.3.5 Methods of analysis

2.3.5.1 Optical microscopy (OM)

The microstructures and fractured surface were studied using optical microscopy, (OLYMPUS GX71). Image analysis technique (Stream Motion Image Analyzer) was used enabling quantitative study of the microstructure evolution at different condition. The SDAS, size and aspect ratio of eutectic Si-particles, area fraction of intermetallic phases were measured in as cast condition. The fraction of cracked/damaged particles after failure was measured. In order to study qualitatively the evolution of microstructural features in as-cast alloy at elevated temperature, a region of interest (ROI) was selected by micro-indentation on the metallography specimens Figure 18. The specimens were then heated up from 300 to 500ºC for 15 minutes. The surface was subsequently probed after each exposure without performing any surface removal step.

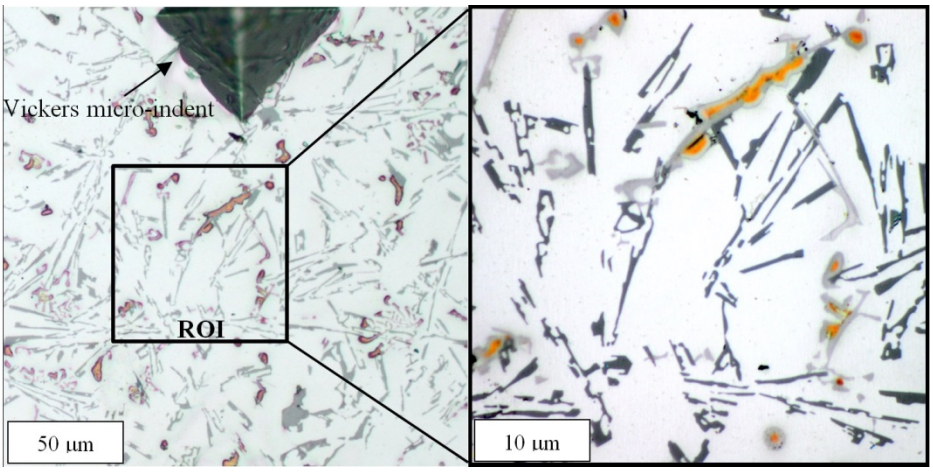

Figure 18. Micrograph of the alloy in ROI.

The rectangular area of (5×1) mm^2 in both sides of the fractured surface, (not closer than 0.2 mm to fracture surface) was probed. It is to be noted that no attempt was made in the quantitative analysis to distinguish the type, size and orientation of fractured particles**.**

2.3.5.2 Scanning electron microscopy (SEM)

In order to study microstructure and particularly the fractured surface, scanning electron microscope (SEM, JEOL7001F) equipped with energy dispersive spectrometer (EDS) was employed. The types of secondary phases in the microstructure of the alloys were identified using EDS analysis.

2.3.5.3 Wavelength-Dispersive X-ray Spectroscopy (WDS)

Exposure at elevated temperature is associated with coarsening of Si-particles and dissolution of selected secondary phases which as a result alter the concentration profile of alloying elements in the matrix. In order to study concentration profiles and micro-segregation of the alloy elements (Mg, Cu and Si) across the dendrite arms at different temperature, the SEM equipped with WDS was employed. The samples for WDS analysis were heated-up to desired temperatures, kept for 15 min and quenched immediately in 40 ºC water, in order to avoid equilibrium cooling. Three points were measured over a single dendrite arm (Figure 19), and at least nine dendrites were measured for each sample.

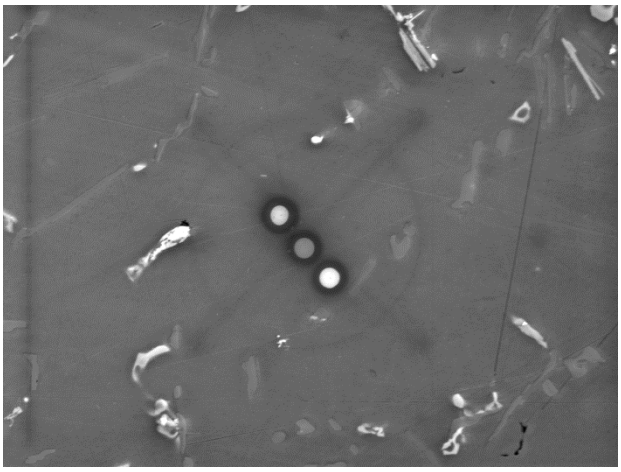

Figure 19. Typical arrangement of WDS probes over a dendrite arm.

2.3.5.4 Electron backscatter diffraction (EBSD)

Grain size determination was made through Electron Backscatter Diffraction (EBSD) analysis to (i) ensure that there were no texture effects from the sample manufacturing technique (gradient solidification), and (ii) to evaluate size of the grain in as-cast condition. A longitudinal section of 10×30 mm was probed from the middle of as-cast rods.

2.3.5.5 X-ray Radiography

X-ray radiography is an imaging technique which uses X-ray radiation to view the internal structure of a different density and opaque object. The technique offers the possibility of detecting macro-pores and other defects inside the specimens and components. Only shrinkage and gas pores larger than 200 μm, were detected. X-ray radiography of the components and tensile specimens was carried out prior to performing tensile tests. The specimens were categorized according to level of micro-pores that they contain.

2.3.5.6 Density measurements

In order to determine the volume fraction of porosity, the mass density of each sample for different conditions was measured via the buoyancy method by means of a Mettler-Toledo machine. The quantity of porosity (φ) was obtained from the equation $f = (\varrho_0 - \varrho_C)/\varrho_0$, where ϱ_0 is the mean density of reference samples, and ϱ_C is density of each sample. The volumetric porosity of (a) the directionally solidified specimens, (b) the specimens extracted from the components and (c) the Sr-modified samples were measured.

2.3.5.7 DSC

Differential scanning calorimeter (DSC) analysis was carried out for the samples corresponding to high temperature study in order to find non-equilibrium reactions which may occur during heating. DSC was performed under purified argon atmosphere using NETZSCH 404C Pegasus instrument with the scanning rate of 5°C/min in the temperature range of 27 - 500 ºC.

CHAPTER 3

SUMMARY OF RESULTS AND DISCUSSION

CHAPTER INTRODUCTION

In this chapter, the main results of the appended supplements are summarized and discussed. The supplements address the research questions to various degrees. This chapter is divided in four main sections; the gradient solidification set up, eutectic Si modification, high temperature deformation behaviour, and physics-based modelling the tensile behaviour of EN AC-46000 alloy.

3.1 THE GRADIENT SOLIDIDFICATION SET-UP

3.1.1 Characteristics of defects in the cast component

Different types of defect were found in the component by means of SEM and optical microscopy. Gas cavities and oxide films were found as the most frequent defects in the component which could be an evidence of turbulent filling conditions see Figure 20.

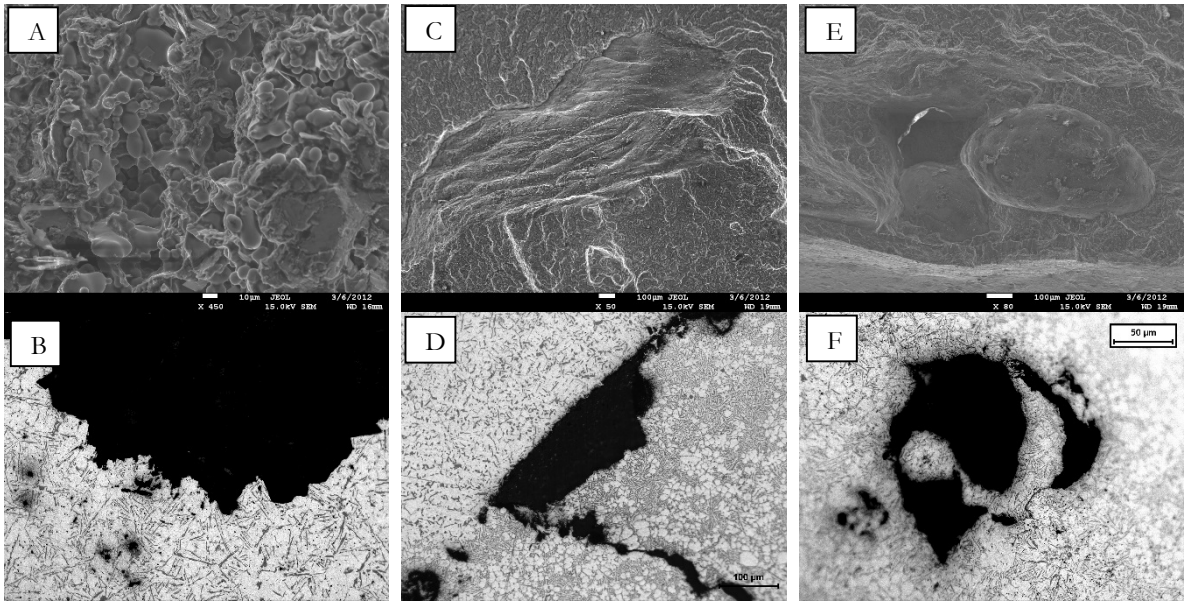

Figure 20. SEM and optical microscopy images of casting defects present inside or in the fracture surface of the cast component. A and B show microporosity in the

fracture surface. B and E shows large oxide film in the fracture surface and inside the component respectively. E and F show a pre-solidified droplet in the area near the fracture surface.

Pre-solidified droplets (Figure 20E and F) were found in the components, which originated from turbulent filling events when fine melt droplets make contact with the mold and rapidly solidify. The interface between the droplets and surrounding alloy lacked coherency which made the interface suitable for crack nucleation. By nature, the HPDC process is turbulent where the inevitable remaining air and gases inside the cavity are entrapped into the casting to a certain degree, even when venting is provided. However several approaches have been employed to reduce air entrapment during filling [57]. The different size pores and gas cavities (in Figure 21) were detected inside the component by X-ray radiography. However, smaller pores, which were not detected through X-ray radiography due to instrumental limitations were found in the following metallographic images. Figure 21 shows the micro- and macro-pores detected in the component.

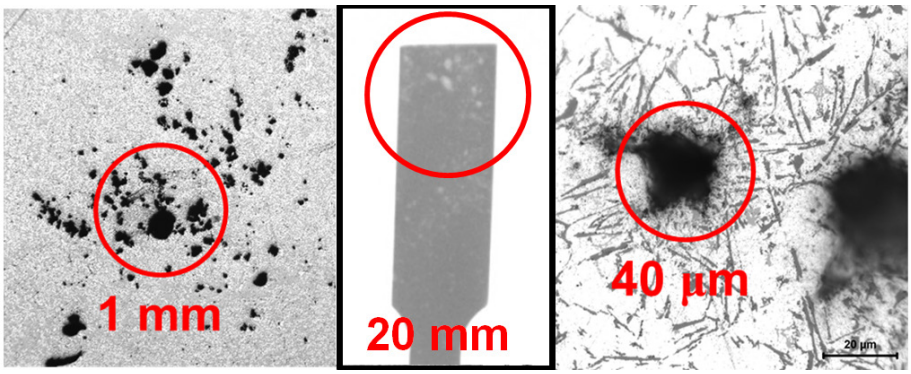

Figure 21. Micro- and macro-porosity in the component.

In addition, potassium- and chlorine- containing particles (Figure 22), which most likely originated from slag residues trapped after melt cleaning with salts, and other slag residues, were also found. Micro-porosity and oxide films are present as well in different sections that can act as sites for crack initiation and propagation. In addition, oxide layers which contribute to failure, and are not detectable through radiography, are found in non-fractured regions as well.

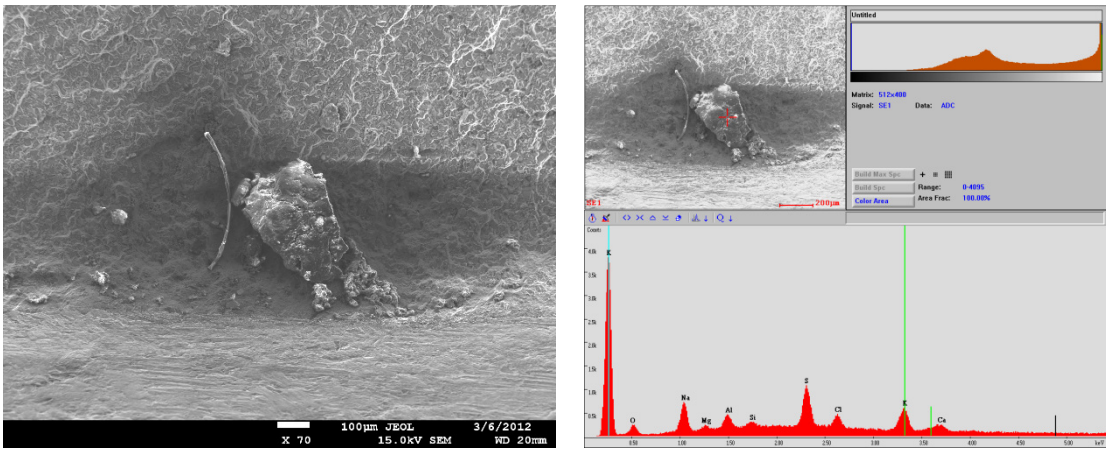

Figure 22. Slag residue found in fractured surface of the failed component.

3.1.2 Defect level in directionally solidified samples

Different possible casting defects found in a typical die cast component were indicated in a previous section. It is well-known that casting defects have marked effects on the tensile properties of the Al-Si casting alloy at room and elevated temperature [58]. The presence of such defects was associated with degrading the ductility to a great extent and consequently shortening of the plastic strain region. They subsequently prevent direct determination of stress-strain relation in the plastic region and also result in significant scattering in measured tensile properties [59]. In order to tackle this issue, the levels of these uncertainties are minimized by using the directional solidification technique in this study.

The specimens were classified with respect to their porosity level as range 0 (reference specimen), 1 and 2 (Category A, for instance A_1 and A_2) according to ASTM standard [60]. In what follows, the specimens will be referred to as A_0 for the gradient solidification specimen, A_1 as representative of the component specimens with no porosity-detected under X-ray and A_2 as representative of component specimens which contain porosity as detected by X-ray radiography. Samples in A_1 and A_2 are extracted from three components and from different locations. Typical locations of extracted specimens are illustrated with solid lines in Figure 15. Density of specimens, as well as the standard error of measurements, was measured and the proportional volumetric pore was calculated considering the directionally solidified samples as reference, see Table 5. Each category contains at least six specimens. It is seen that the level of porosity in the specimens is significantly reduced using the gradient solidification set-up.

Table 5. Density, ϱ, standard error, SE, and volumetric pore fraction, f, of specimens.

	A_0	A_1	A_2
ϱ (kg/m^3)	2715	2645	2539
SE	20	34	71
f (%)	0	2.57	6.48

3.1.3 The microstructure contrast

The gradient solidification set-up was assigned to produce samples having desired SDAS by changing the furnace pulling speed. Figure 23 shows the microstructure of EN AC 46000 alloys cast (a) in gradient solidification set up, A_0 category and (b) in a die cast component A_1 and A_2 categories. Due to the excellent feeding conditions, A_0 class castings possess a homogenized and well-organized dendritic structure compared to those in the cast component (A_1 and A_2) that show non-uniform structures. However, all categories showed similar microstructural behaviour with respect to SDAS, Si particle morphology and other intermetallic compounds. A_0 and A_1 have quite similar SDAS in the range of 11.2 ($\pm$3.1) μm and 9.4($\pm$1.8) μm respectively.

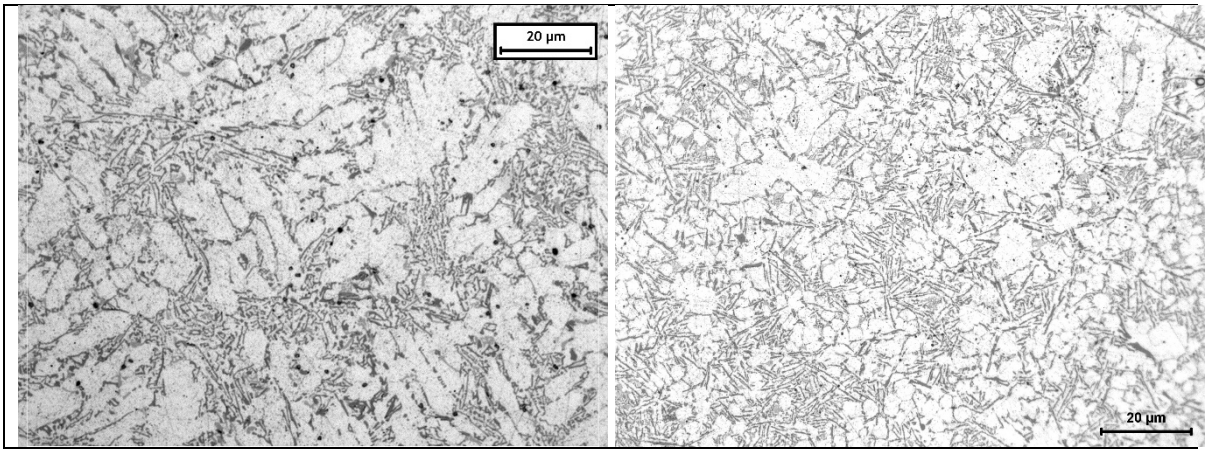

Figure 23. The microstructure of EN AC 46000 alloys cast (a) with gradient solidification set up and (b) in a die cast component.

SDAS is used as reliable index to distinguish microstructure scale in cast Al components. It is a function of the local solidification time and quantifies size of microstructure as well as its constituents. Differences in local solidification time between wall and centre sections of a cast component reflect upon the dimension and morphology of α-Al phase and eutectic Si particles. SDAS increased from the wall (high solidification rate) to the centre (lower solidification rate). The morphology of the α-Al showed mainly an equiaxed globular geometry in regions close to wall sections due to rapid solidification. This gradually developed into branches and dendrites moving toward the centre. The difference in SDAS, however, is not remarkable due to the constant thicknesses of sections of the component (~ 3-6 mm).

3.1.4 The characteristic of tensile behaviour

Due to variations in porosity, which is qualitatively monitored (Figure 21) and quantitatively reported (Table 5), comparing A_0, A_1 and A_2 the static tensile tests showed a notable decrease in the ultimate tensile strength (UTS) and elongation to failure as shown in Table 6. Reported data are average values of at least six tensile test specimens from three components.

Table 6. Mean values and standard errors (95% confident interval) of static tensile tests performed on specimens. Data for EN AC-44300 are reported according to DIN EN 1706 [61]. * F is representative of "as cast" condition.

	EN AC-44300	**A_0**	**A_1**	**A_2**
Yield strength (MPa)	**130**	**115**	**115**	**101**
SE	-	2	0.3	3
UTS (MPa)	**240**	**251**	**210**	**167**
SE	-	2	14	10
Elongation to failure (%)	**1**	**7.1**	**3.1**	**1.5**
SE	-	0.5	0.5	0.2
Material condition	**F***	**F**	**F**	**F**

The decrease in UTS and elongation to failure is a function of density in the studied specimens (Table 6). The decrease in UTS is significant when the degree of porosity is increased from A_0 to A_1 and from A_1 to A_2. The presented trend is in agreement with other studies [62, 63].

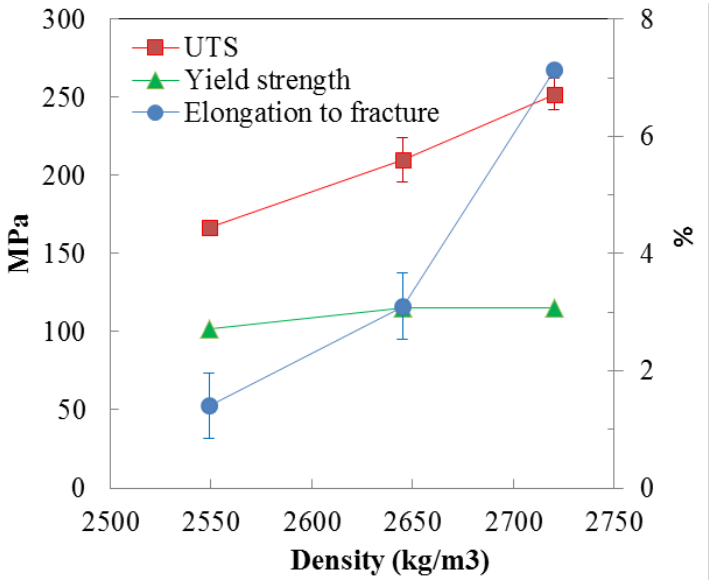

Figure 24. Tensile properties as a function of density of different classes.

Since the X-ray analysis does not reveal other casting defects such as surface oxides, cold fills and inclusion particles, it is worthwhile keeping in mind that the observed decrease in tensile properties could also be affected by the aforementioned casting defects, mainly in the crack initiation and propagation stages. However, porosity is introduced as the most thoroughly investigated defect in literatures data as well [62, 64]. The stress-strain curves of specimens belonging to A_1 and A_2 classes follow the curves of A_0 class which is obtained by gradient solidification (Figure 25).

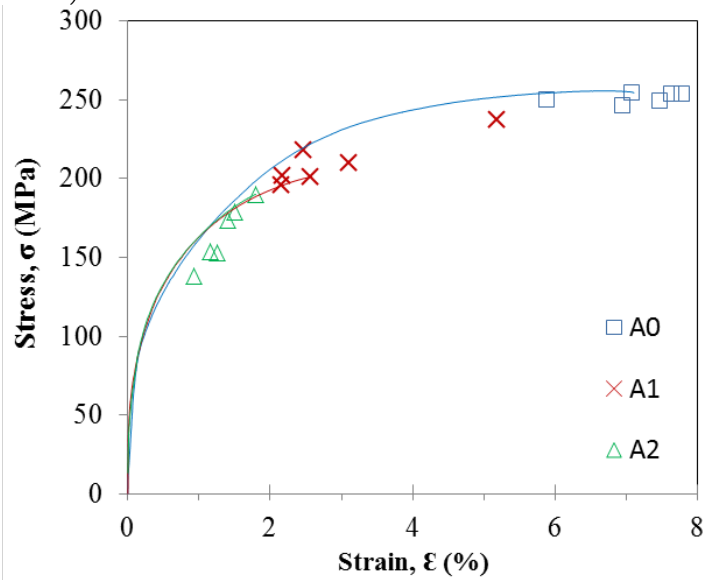

Figure 25. Tensile test curves for specimens of different classes. The indicated points are representative of UTS and elongation to failure of each specimen.

Moreover, all classes show similar yield strength values which confirm this behaviour (Figure 24). Nevertheless fracture occurs at lower stress and strain levels in specimens of A_1 and A_2 classes. The remarkable improvement of tensile properties, which is clearly mapped in Figure 25, is mainly caused by minimizing the levels of casting defects. Once the specimen subjected to a tensile load, a region of porosity would yield first due to the reduced load bearing area

concentrating the stress near the voids [62] is regarded as the main reason of lower strength and ductility of specimens of A_1 and A_2 classes. Through the gradient solidification technique, it was proven that the alloy and component has a potential to be improved more than 300% increase in elongation and 50% in UTS due to reduction of defects. This has been also indicated in other works [65, 66].

3.2 SR-MODIFICATION

3.2.1 Microstructural evolution by modification

3.2.1.1 Directionally solidified samples

In a general view, the microstructure of Al-Si-Cu-Mg cast alloys is a mixture of α-Al dendrites surrounded by the Al-Si eutectic aggregate and decorated by intermetallic compounds (e.g. Al_2Cu, β-Al_5FeSi, etc.). The microstructure variations of the samples obtained under different cooling rates, yielded average SDAD of 10, 25 and 50 μm, are presented as a function of the Sr level in Figure 26.

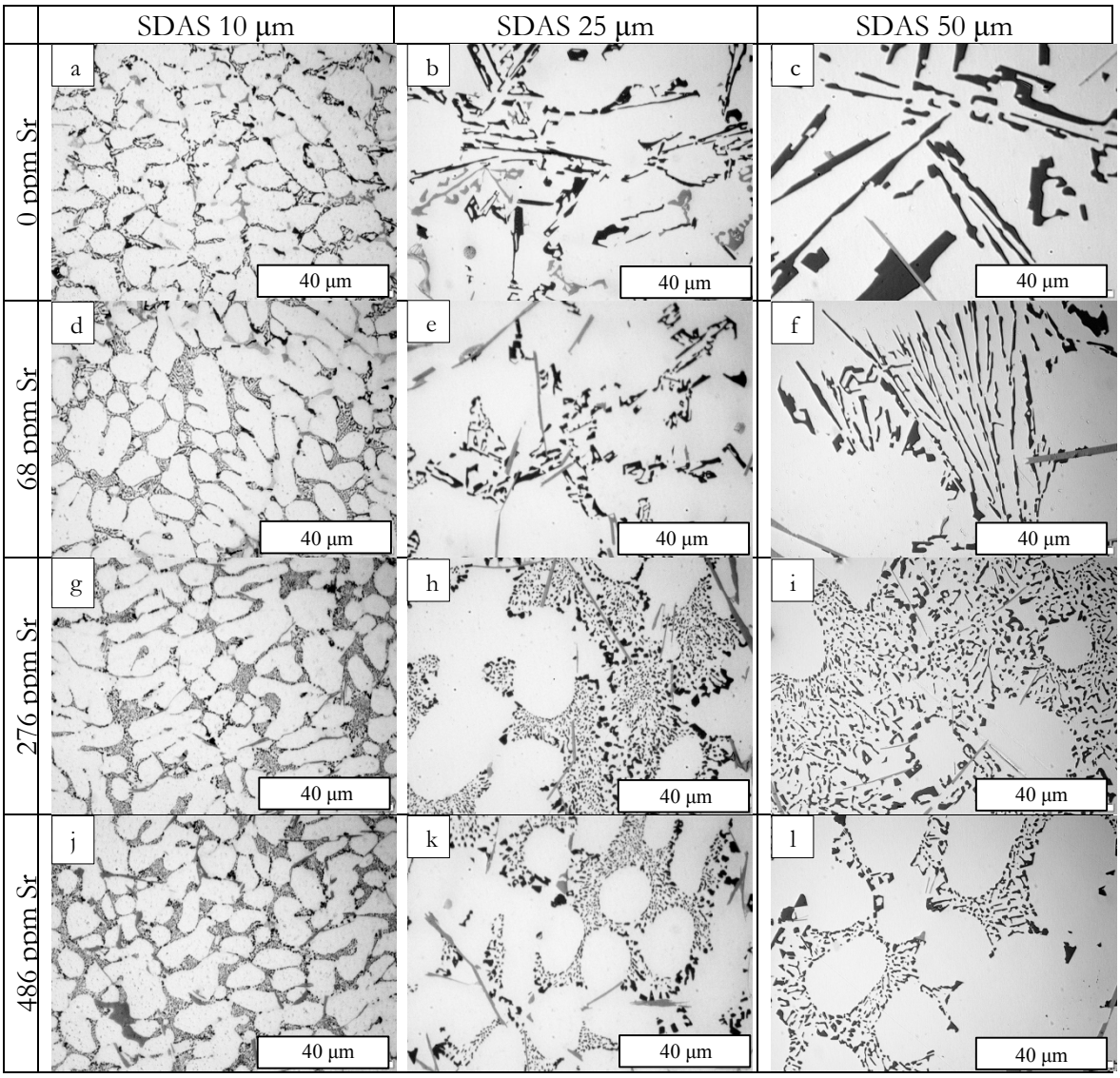

Figure 26. Microstructural evolution of unmodified and modified alloys directionally solidified with different cooling rates; from left to right SDAS is increasing, from top to bottom Sr content is increasing.

As depicted in Figure 26 a, b and c, the microstructure in the unmodified samples contains coarse plate-like Si-particles that often radiate from polyhedral Si particles. Although an increased cooling rate refined the microstructural constituents and reduced eutectic Si in size, it did not change the plate-like morphology of Si-particles. By adding 68 ppm Sr, the

morphology of Si-particles in samples with different SDAS showed a marginal change. Above 68 ppm Sr, as revealed in Figure 26 size of eutectic Si was dramatically reduced and the morphology is coral-like proving that Sr can change the eutectic Si from acicular to fibrous even if the eutectic phase is encompassed with various intermetallic compounds. Different Sr levels lead to different degrees of change in the morphology, depending on the coarseness of microstructure. Nevertheless, a clear progressive trend of Si modification level can be observed in samples having different SDAS. At levels of 68 ppm and eutectic structures still contain regions with a bimodal distribution of Si, in which typically fine fibrous Si is accompanied by coarse particles. In order to achieve a complete modification of Si for these coarsest microstructures, an addition of at least 278 ppm is required. However, when the Sr addition is increased to 500 ppm, the result is almost the same as that with 280 ppm, but excess Sr might generate Al_2Si_2Sr compounds in the microstructure and consequently degrade the alloy performance, as stated in the literature [67].

3.2.1.2 Mold cast samples with controlled cooling rate

The microstructures of the alloy cast under different cooling conditions and containing various Sr levels are depicted in Figure 27. The microstructure coarseness was measured through SDAS, which is a function of cooling rate. The measured SDAS for different solidification systems are summarized in Table 2.

Table 7. Corresponding SDAS for different cooling systems.

Mold type	Steel	Ceramic	Insulated mold
Cooling rate (ºC/s)	3.8	1.4	0.4
SDAS	20 ± 4	49 ± 7	91 ± 6

It is clearly demonstrated that the fast cooling rate resulted in smaller SDAS and smaller eutectic Si particles. However, no significant change in flaky morphology of Si was observed upon increased cooling rate.

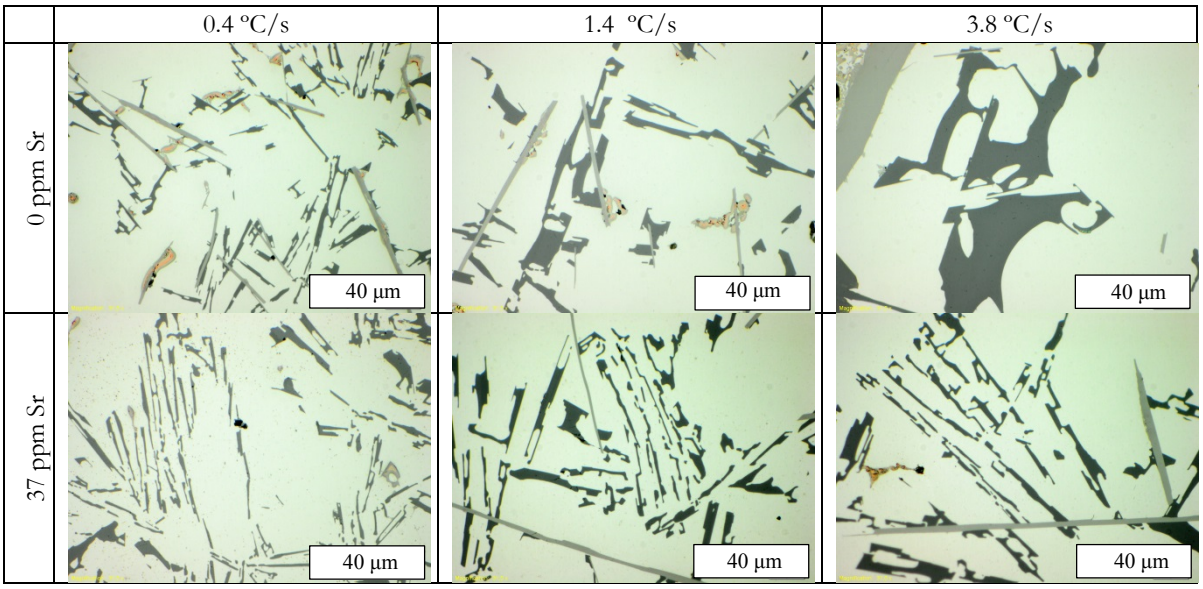

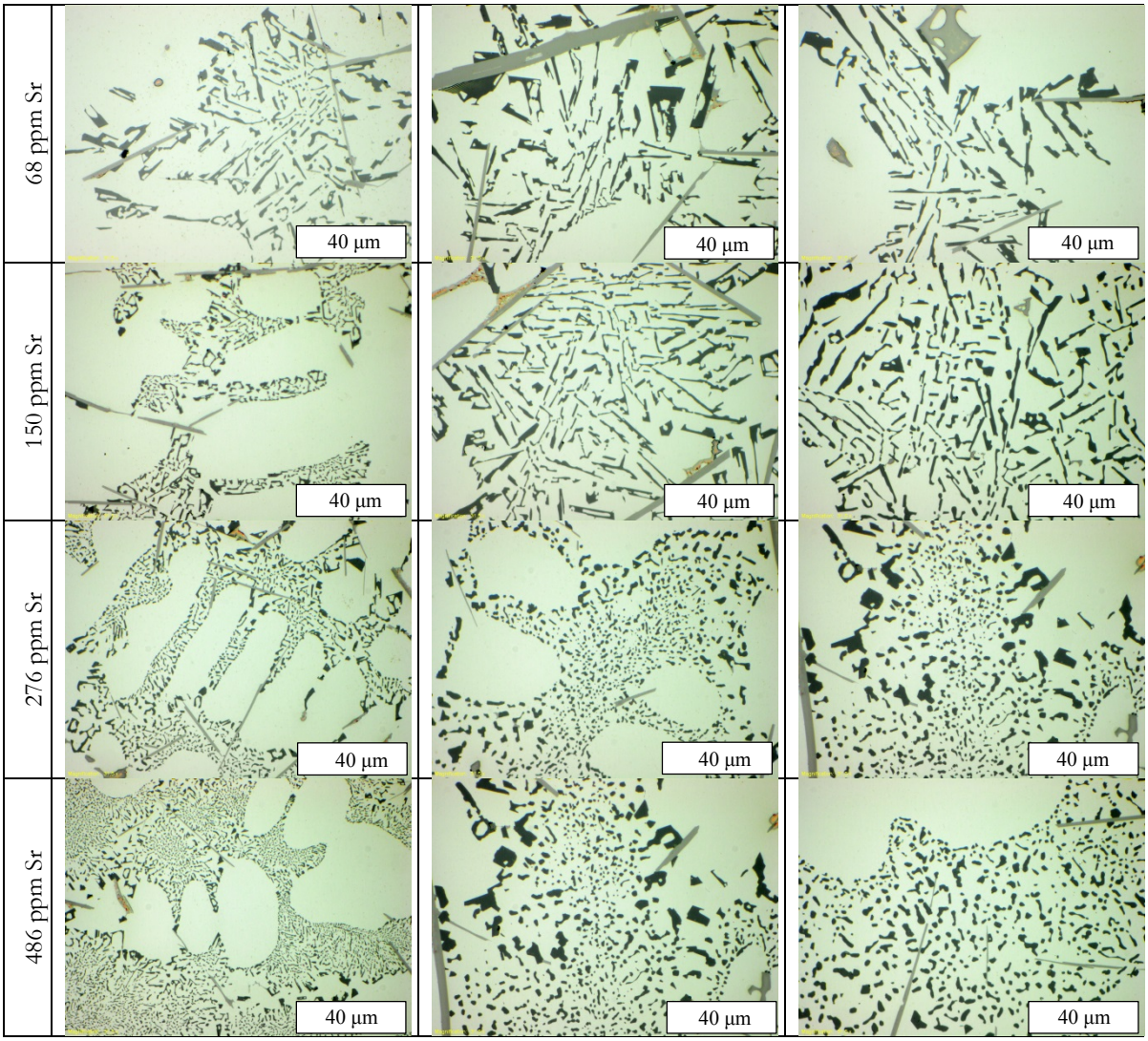

Figure 27. Micrographs showing Si structure cast under different cooling conditions and containing varied Sr content.

On the other hand, the optical micrographs clearly illustrate the tendency toward formation of fine fibrous eutectic Si particles upon initial addition of Sr and increasing level of Sr. It seems that the trend is quite similar for all coarseness of microstructure.

3.2.2 Assessment of modification level

Three different approaches were examined in order to assess the modification level (ML) and find the optimum Sr level in EN AC-46000 alloy. In what follows, the results and discussion on these approaches are explained.

3.2.2.1 AFS chart - The comparative approaches

The given microstructure is qualitatively compared with the American Foundry Society (AFS) chart for microstructure control in hypoeutectic alloys. The AFS charts contain six different classes; from unmodified (class 1) to fully modified (class 6). Based on visual comparison a given specimen is located where the microstructures and AFS chart are similar [68, 69]. The twenty four micrographs of each case were considered from two different cross-sections of

specimens and 2 specimens for each case. The ML for each case was then calculated as the following equation; ML = ((1 × a) + (2 × b) + (3 × c) + (4 × d) + (5 × e) + (6 × f))/n
where a - f are number of images located in each class (from 1 to 6) and n in number of total image for each case which was equal to 24. ML of Si for each sample was calculated according to the above-mentioned equation and the results are depicted in Figure 28.

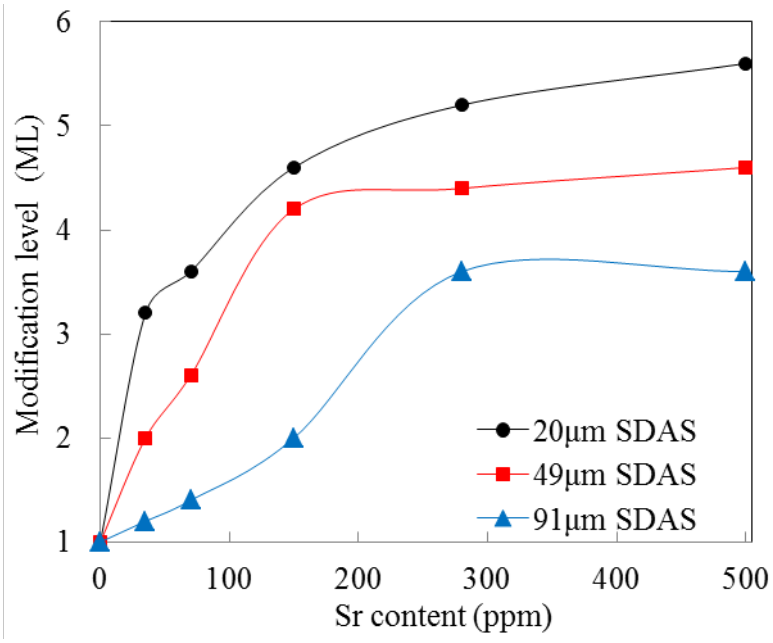

Figure 28. Effect of Sr content on ML for different SDAS.

This clearly shows the progressive trend of ML by increasing the Sr content. The trend is quite consistent for different coarseness of microstructure. The ML values obtained for different SDAS however are different. This approach was realized as an easy and practical method in order to assess the ML. Nevertheless the approach is time-consuming and subjective and suffers from a lack of accuracy.

3.2.2.2 The microstructure evaluation

The evolution of the Si morphology from coarse plate-like towards fine fibrous as a function of Sr content are depicted in Figure 27. Quantitative assessment of Si modification was done through analysis of 12 optical micrographs from two different cross section of each sample using image analysis system. Aspect ratio (AR), area and perimeter of eutectic Si particles were measured and mean value of them as a function of Sr level are depicted in Figure 29.
As a result, AR, area and perimeter of particles are expected to be decreased as Sr level increases. The results based on aspect ratio of Si particles showed negligible changes with changing Sr level from 0 to 486 ppm. This may be due to the fact that the microstructure analysis is necessarily two dimensional. Hence this parameter has proven to have poor validity in expressing the level of modification. This was also pointed out by Djurdjevic [23]. Compared to AFS charts on the relationship between Si morphology and ML [70], the current measurements on area and perimeter yielded similar trends which are an overall reduction of Si area and perimeter as a function of Sr content. Djurdjevic et al [23] has done an identical assessment for the 319 Al alloy cast in a graphite mold. The perimeter of eutectic Si particles was introduced as the most promising index to describe Si modification level through metallographic analysis which is in agreement with the present investigation. However the results of this study show that the trend is not consistent for slow cooling rates. The general decreasing trend in area and perimeter is accompanied with a slight increase

when the Sr content exceeds 150 ppm, which clear for the case of 0.4 ºC/s. This behavior could be due the presence of coarse particles which enlarged the mean values of area and perimeter. Increasing the population of counted particles (e.g. by counting multiple surfaces) may yield a more unified trend for all cooling conditions. The solution however requires more operational time and simultaneously increases the subjectivity of the results.

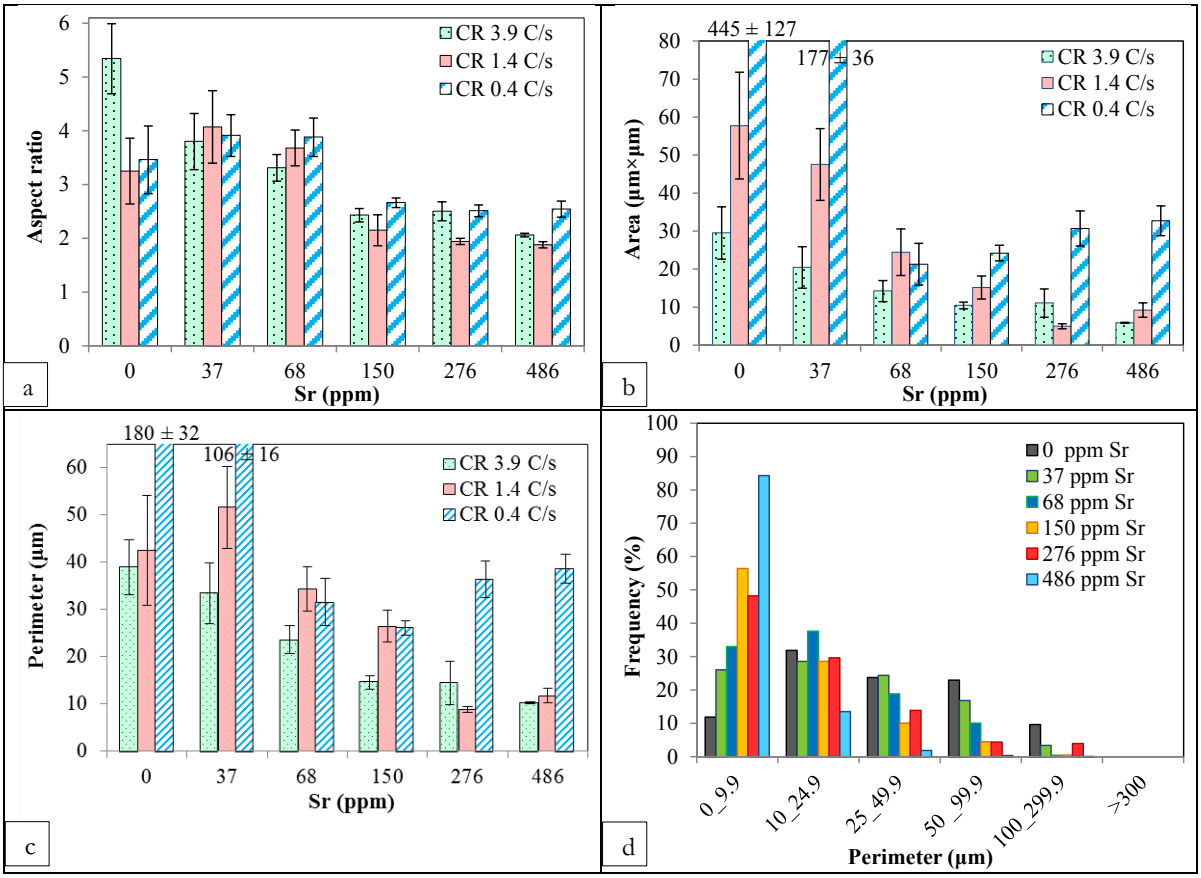

Figure 29. The diagrams showing a) Aspect ratio, b) Area and c) perimeters of Si-particles as a function of Sr content in the alloy. d) Histograms graph for the perimeter of at 3.8 ºC/s cooling rate.

Once the cooling rate increases, the gap between value of the parameters for each level of Sr decreases and thus the trend seems to become constant. The behavior was observed for both perimeter and area results, see Figure 29. In addition, the values of those parameters scattered significantly, especially in unmodified structures. For instance, the area varied from 100 to 2500 µm^2 and perimeter from 50 to 600 µm for the unmodified structure with cooling rate of 0.4 ºC/s. Thus, area and perimeter of adjacent Sr levels applying 95% confidence interval were overlapped at higher cooling rates (3.9 ºC/s), while it was noted that the structure visually changed significantly upon addition of Sr, see Figure 27. Thus, the mean value is assumed not to be a promising measure to report the parameters and relate them to modification level especially where the cooling rate is decreased. In a similar work [23] the median value of perimeter of Si particles was used in order to quantify the modification level of the microstructure. However, initially median value is assumed as an imprecise measurement.

The scattered values of perimeters are clearly depicted in Figure 29 which confirms the inaccuracy of using means value measurement. Summarisation of the smallest perimeter range (< 10 µm) shows the portion of structure which is fully modified. The general trend is

increasing over the addition of Sr at 3.8 ºC/s cooling rate, see Figure 29d. A similar trend was observed for the 0.4 and 1.4 ºC/s. It also shows a distinct gap between each adjacent Sr level. Despite an increase in the fraction of refined particles, the coarser still remained unaffected upon addition of 37 and 278 ppm Sr. This also confirms that the presence of residual coarse particles in selected regions may significantly affect the trend. Accordingly, the perimeter and area frequency of fully refined structure in histogram graphs appeared to be the best index to be employed to express modification status of the microstructure. However, the descriptor still excludes several particles and is also unable to yield the optimum Sr level for the alloy. All in all, characterizing the modification level through micrographs analysis was realized to be subjective and time consuming method. Hence it is not an appropriate approach to be employed in foundries in order to predict the optimum modification level in the Al-Si alloys.

3.2.2.3 Thermal analysis

Figure 30 shows cooling curves of the alloy in unmodified condition solidified in different molds. The alloy exhibits three main reactions during the solidification processes as pointed out, see arrows in Figure 30. The solidification starts with formation of α-Al dendritic networks in the temperature range of 620-580ºC followed by the development of eutectic phases; Al and Si in the temperature range of 580-555ºC. Eventually other intermetallic compounds are formed below 550 ºC [71-73]. In order to evaluate the modification level through cooling curves, nucleation and growth temperatures of the Al-Si eutectic are important parameters.

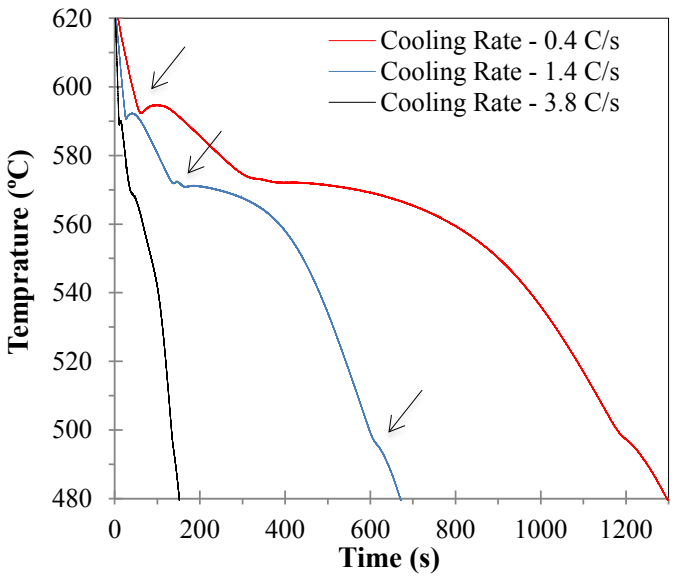

Figure 30. Cooling curves of the unmodified alloy at different cooling rates.

Generally two notable changes occur in the eutectic regions by the addition of Sr; first, a decrease in eutectic growth temperature (T_G) which means increased undercooling of the eutectic growth and second, an increase in recalescence undercooling of eutectic region [74]. Figure 31 a-c indicate that the minimum eutectic growth temperature was decreased with addition of Sr, up to a certain level and then slightly increased once the Sr content increased. It is well known that, Sr restricts the growth of Si acting as a impurity atoms which poisons the growing layers [22]. Blocking the growth of Si increases nuclei numbers and as a result reduces the nucleation and then growth temperature of Si [74], Figure 31 (a-c).

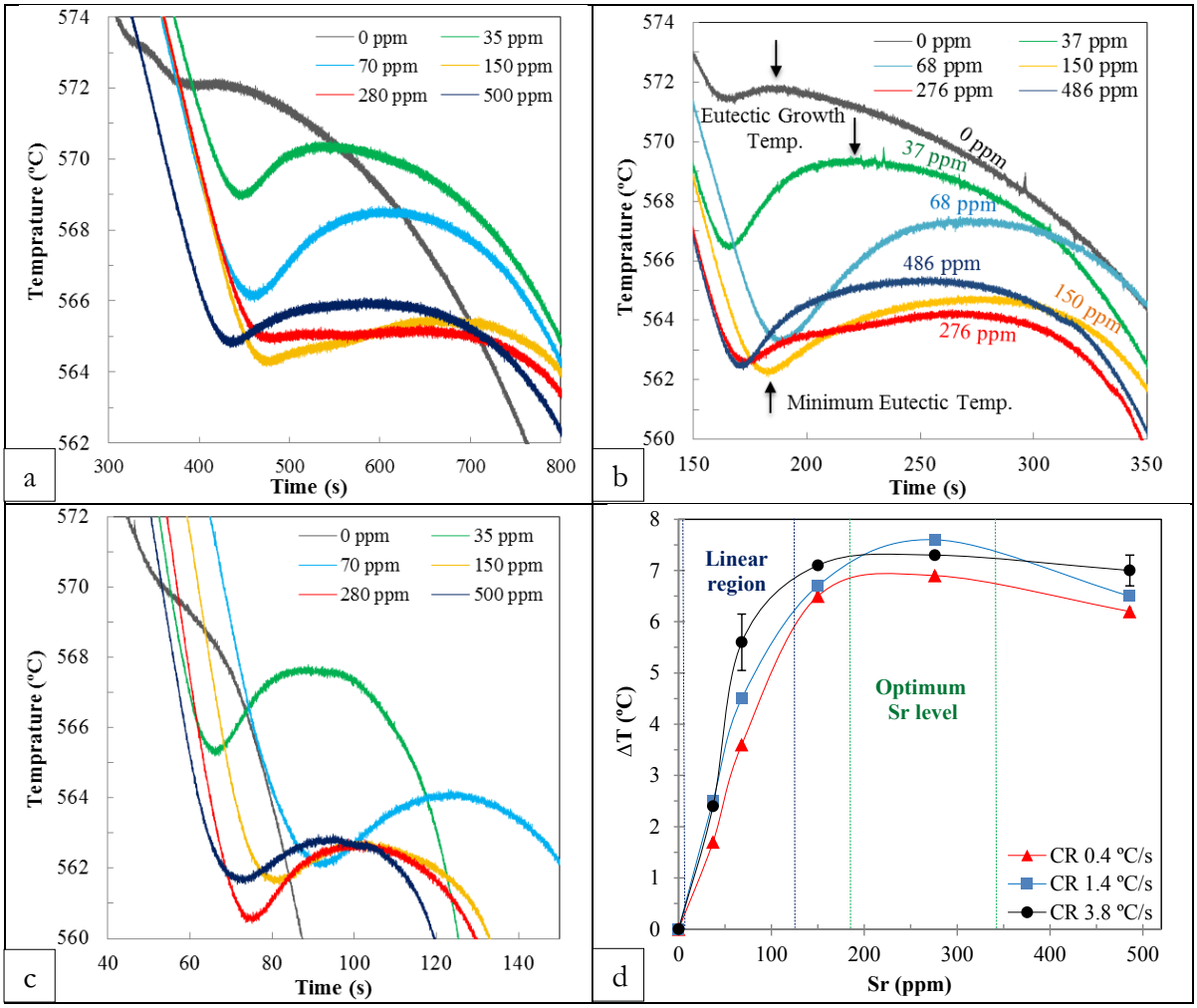

Figure 31. Cooling curves of EN AC-46000 alloy at eutectic region for different level of Sr. Cooling rate is a) 0.4, b) 1.4, c) 3.8 °C/s. d) Changes in eutectic growth temperature as a function Sr content at different cooling rates.

However, once Sr content exceeds a particular content, the excess amount forms the deleterious Al_2Si_2Sr intermetallic phase which also degrades the modification effect [67]. Hence, looking at thermal curves of the Al-Si alloys during solidification, the maximum eutectic growth temperature shifts to a lower value upon addition of Sr and this effect starts to diminish as the Sr content exceeds than a particular level [72, 74, 75]. Figure 31 (a-c) shows that increasing the Sr concentration in the alloy from 280 to 486 ppm leads to an increase in eutectic growth temperature. The trend is quite identical for all cooling conditions. It is suggesting that the excess amount of Sr does not additionally contribute to the modification of the Si particles and will exclusively form deleterious intermetallic compounds. Shabestrai et al. [74] studied the effect of Sr content on the eutectic nucleation and growth temperature of a Al5Si3CuMg cast alloy. It was pointed out that addition of 160 ppm decreases the minimum eutectic temperature by up to 6°C compared to the unmodified alloy, while 180 ppm Sr and upwards (to 800 ppm) resulted in an almost constant 3°C decrease in minimum eutectic temperature. This is in agreement with the finding of this study, and suggests that the lower Si-containing alloy demands less Sr to obtain the fully modified structure. One has also to bear in mind that the optimum Sr content, yielding the highest modification level without formation of Al_2Si_2Sr phase, is a function of Si level in the alloy.

Therefore, the depression of eutectic growth temperature from unmodified to modified structure ($\Delta T = T_{G/unmodified} - T_{G/modified}$) seems to be a suitable parameter expressing the modification status in Al-Si alloy. Figure 31(d) shows ΔT as function of Sr level for different cooling rates. Djurdjevic et al. [23] used ΔT in order to correlate modification level to Sr content in W319 Al cast alloy through a curve fitting equation. Francis et al. [68] used thermal analysis parameters as inputs to develop neural networks models which enables prediction of Si modification level in a W319 Al mold-cast alloy.

The trends in Figure 31(d) are initially ascending untill a maximum value is reached, followed by a slight reduction. In the linear region (pointed out in Figure 31), the relation between depression in eutectic growth and Sr content is approximately linear. The curve fitting equations of these regions are a promising means for online prediction of modification level of castings [23]. However it seems that the optimum Sr content is where ΔT obtains its highest value irrespective of cooling condition. Prior to reaching the peak point, the Sr content is not enough to modify all Si particles, Figure 31d. While after the peak point, Sr tends to form intermetallic compounds and its modification role diminishes. Therefore it is believed that the indicated region in Figure 31(d) (Sr level where maximum ΔT is obtained, plus/minus a few tens of ppm) is the optimum range of Sr levels offering excellent modification. Since the online prediction approach is through recording the thermal history of the melt, the acquired parameter (for example ΔT) is a unique value based on activity of Sr in the melt and represents the whole melt. However, results of the image analysis technique are based on evaluation of 2D microscopy images of a few hundreds of Si particles. It was already pointed out in another work [70] that, surprisingly the most appreciate significant improvement in tensile properties (in particular elongation to fracture) of the alloy was achieved by addition of 276 ppm Sr [67].

Figure 31(d)shows that the thermal history of the alloys in eutectic region at different cooling rates are quite similar suggesting that online prediction of optimum Si level in the alloy is independent of casting condition. It means that the size and type of the mold do not play any role in the experimental set-up which makes this method suitable for the industrial foundries. Thus, it is believed that employing thermal analysis for the online assessment of optimum level of Sr in the Al-Si cast alloys is inexpensive, accurate and objective approach.

3.2.3 Mechanical properties and failure analysis

3.2.3.1 The porosity formation

Modification as well as solidification rate play an important role in volume fraction and characteristic of defects such as gas porosity and shrinkage cavity [76, 77]. The volume fraction of porosity was measured for unmodified and modified samples having different SDAS via buoyancy method. It is worth noting that the melt hydrogen content has not been measured and assumed in this case to be constant for all the alloys since they have been produced under similar conditions. A general observation indicates that porosity values for all conditions are relatively low, less than 1%, which is due to the mode of solidification as a result of using the gradient solidification technique, see Figure 32. Samples are solidified in directional manner and a major part of the impurities are pushed ahead the advancing solidification front which are later cut off and are not a part of the evaluated samples. In addition, the current study cannot reveal any trend in porosity level as a function of Sr, irrespective of the SDAS, which is in agreement with the a study by Dinnis et al [76].

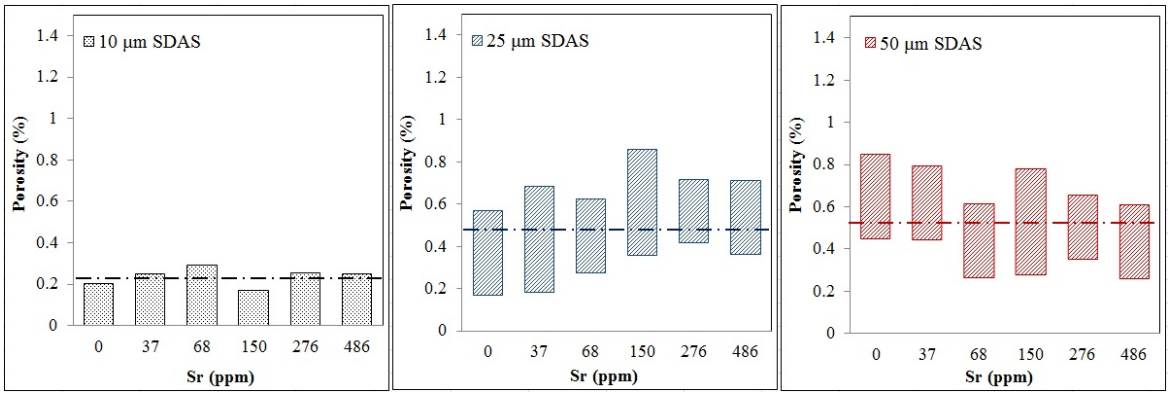

Figure 32. The volumetric pores in samples with different Sr content and SDAS.

As the solidification time is shorter for smaller SDAS, less time will be available for the diffusion of the hydrogen into the interdendritic regions which results in lower pore volume fraction. Theories of oxide films suggest that when an oxide film is approached by the solidification front, the film experiences the hydrogen-rich environment produced by the rejection of gas from the advancing solid. Furthermore, the gas gains access by diffusion into the air pocket in the gap of the oxide particles, the pore will start to form and grow. As the freezing rate becomes slower, higher SDAS, and the film is poorly wetted by the melt, time will therefore be available for more hydrogen to diffuse resulting in pore expansion and growth resulting as well in larger pore volume fractions as indicated from the measurements in the current study [78, 79]. Comparing the pore volume fractions, the samples with SDAS 25 and 50 µm are associated with largest fraction of porosity which might be due to the arrestment of premature pores as they become entrapped by the advancing solidification front; irrespective of the Sr content.

3.2.3.2 Tensile properties and failure analysis

The qualitative study of the microstructures Figure 26 showed that Si-particles are refined by the additions of Sr, however no evidence was found that the Fe- and Cu-rich intermetallic phases have been influenced by the modification treatment. As the series of micrographs (Figure 26 a-c) clearly demonstrate, the smaller the SDAS the finer and more homogenous is the microstructure. The fracture surface seen in profile of the smallest SDAS is of more transgranular character, while for large SDAS (25 and 50 µm) the fracture profile seems to be more intergranular, as depicted in Figure 33. It was also realized that the Fe-rich compounds are formed as coarse and large platelets with a random orientation. However in small SDAS they are refined in size to a great extent.

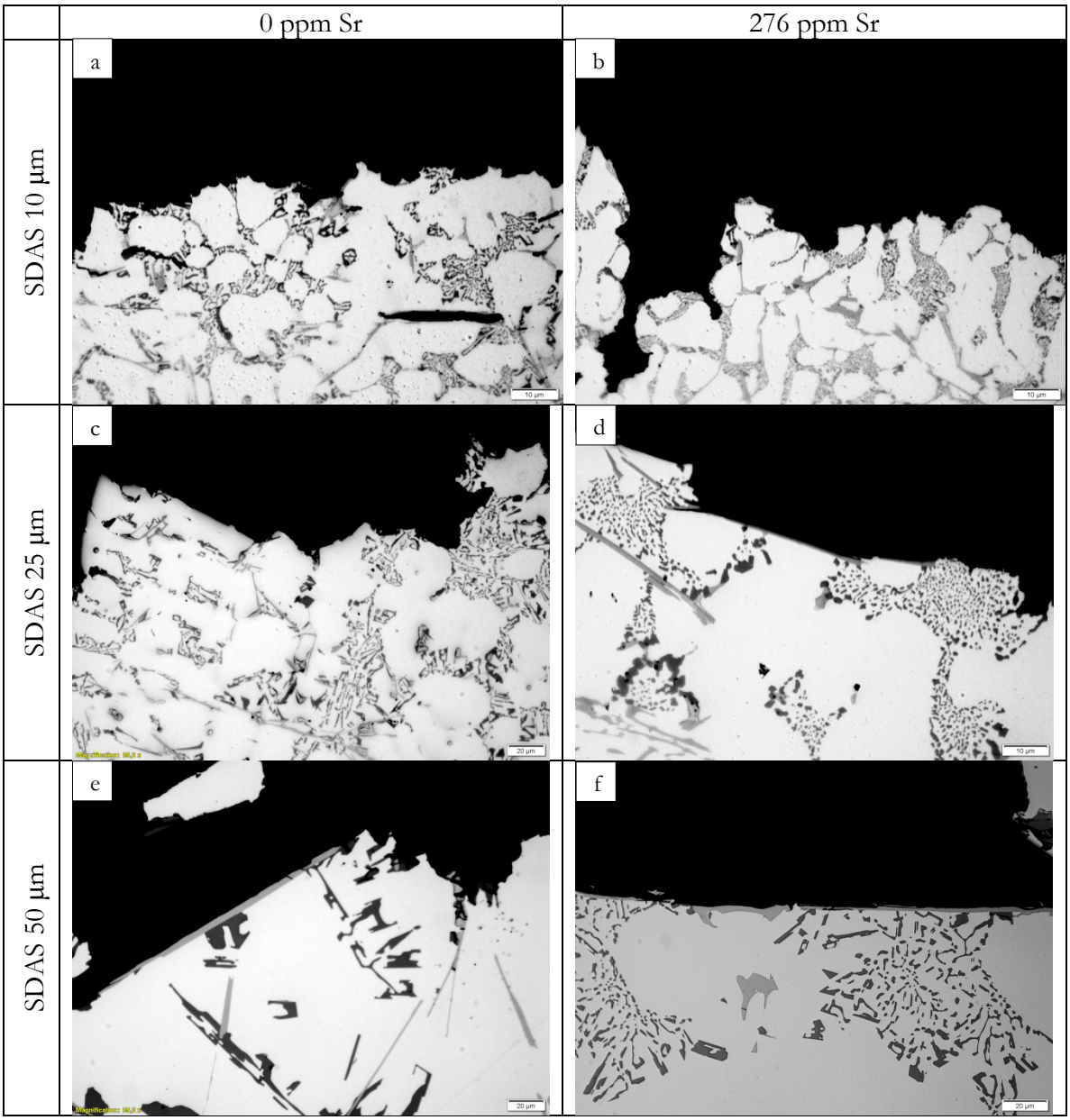

Figure 33. Fracture profile of EN AC-46000 alloy in unmodified and modified condition having different coarseness of microstructure.

In materials that are subjected to monotonic loading, the progression of damage occurs by nucleation and growth of cracks. The release of stresses that are carried by the secondary particles such as Si-particles and intermetallic compounds, at a macroscopic level when cracking occurs, affect the overall load bearing capacity of the material. When the cooling rate is high, the eutectic Si-particles are reduced in size. However they may also be modified in their morphology through the Sr additions. The overall microstructure constituents (e.g. secondary particles) are also refined as a result of increased cooling rate. As the size of intermetallic compounds is minimized (fine and small particles), the influence of Sr-treatment is evident which directly impacts on the elongation to fracture where the fracture seems to be transgranular and interdendritic, see Figure 34. The reduction in elongation to fracture for the case of larger SDAS (25 and 50 µm) rather than the small SDAS, might be related to the presence of larger Si particles with flake-like morphology and to the large iron-rich needles or

platelets. Since Sr modification did not impact on the size and morphology of the Fe-rich compounds, it seems that these phases are controlling to a major extent the fracture behaviour. The fracture profile indicates that the fractures in samples with SDAS 25 µm seem to follow the particle orientations and exhibit a mixed mode failure. In most cases, the fracture is dominated by the iron-rich intermetallics, and Si particles. In the coarser microstructure (SDAS 50 µm) the fracture seems solely of an intergranular failure mode where the iron-rich phase plays a dominant role. Being hard and brittle, these needles tend to have relatively low bond strength to the matrix and as noticed from the fracture profiles in Figure 33, there are no doubts that the iron-rich intermetallics together with the Si particles have been participating in the damage events. Both seem to play a critical role in the crack initiation and propagating processes, acting as easy crack paths, linking the particle fractures together and leading to an uncontrolled fracture of the material. In these cases, the role of Sr on elongation to failure is absent, instead iron-rich particles has to be neutralized by a proper corrector, normally Mn [80]. The tensile strength depends also on the overall fineness of the microstructure. A non-modified structure with SDAS 10 µm possesses finer and rounder Si than a non-modified structure where SDAS is 50 µm The overall structure differences directly impact the tensile strength as depicted in Figure 34. As Si is modified, the tensile strength is slightly improved but not to the same extent as the elongation to fracture, see diagrams in Figure 34.

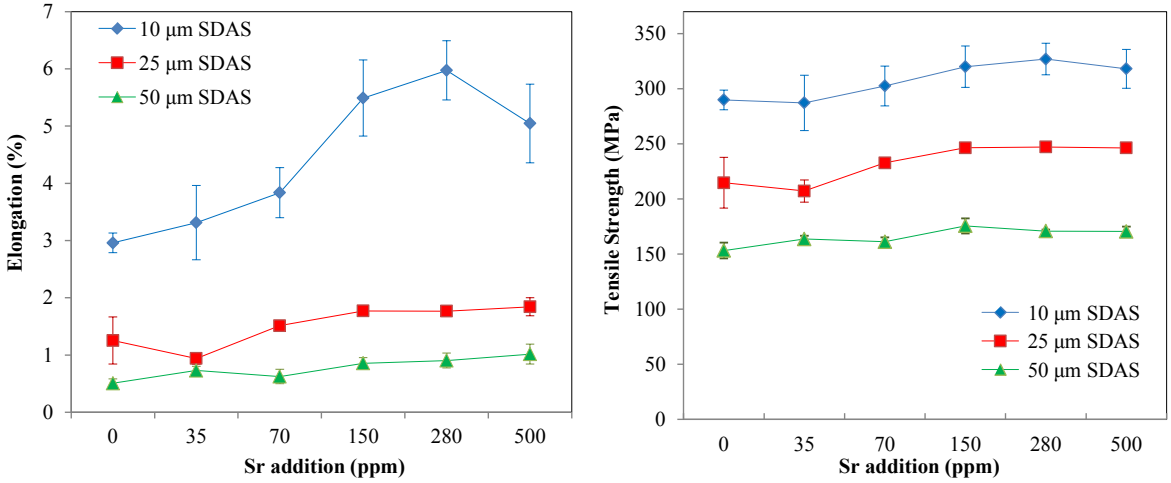

Figure 34. Effect of Sr content and cooling rate on elongation to failure and UTS.

3.3 HIGH TEMPERATURE DEFORMATION BEHAVIOUR

3.3.1 Microstructural characterization

3.3.1.1 The scale and morphology of microstructural features

Figure 35 shows the microstructural features of the EN AC-46000 alloy as-cast at two different cooling rates. The cooling rate governs size, morphology and distribution of the eutectic Si particles and intermetallic compounds [81, 82]. The microstructure consists of primary α-Al dendrites surrounded by eutectic Si particles and intermetallic phases. The intermetallic phases identified (Al_2Cu, α-Al_8Fe_2Si, β-Al_5FeSi) are indicated in Figure 35, which illustrates the effect of cooling rate on the scale of the microstructure. Increasing the solidification rate refines all microstructural features, decreases the SDAS and changes the

morphology of eutectic Si from large and elongated plates to small and rounder particles. This is supported by quantitative measurements of eutectic particle aspect ratio, see

Table 8.

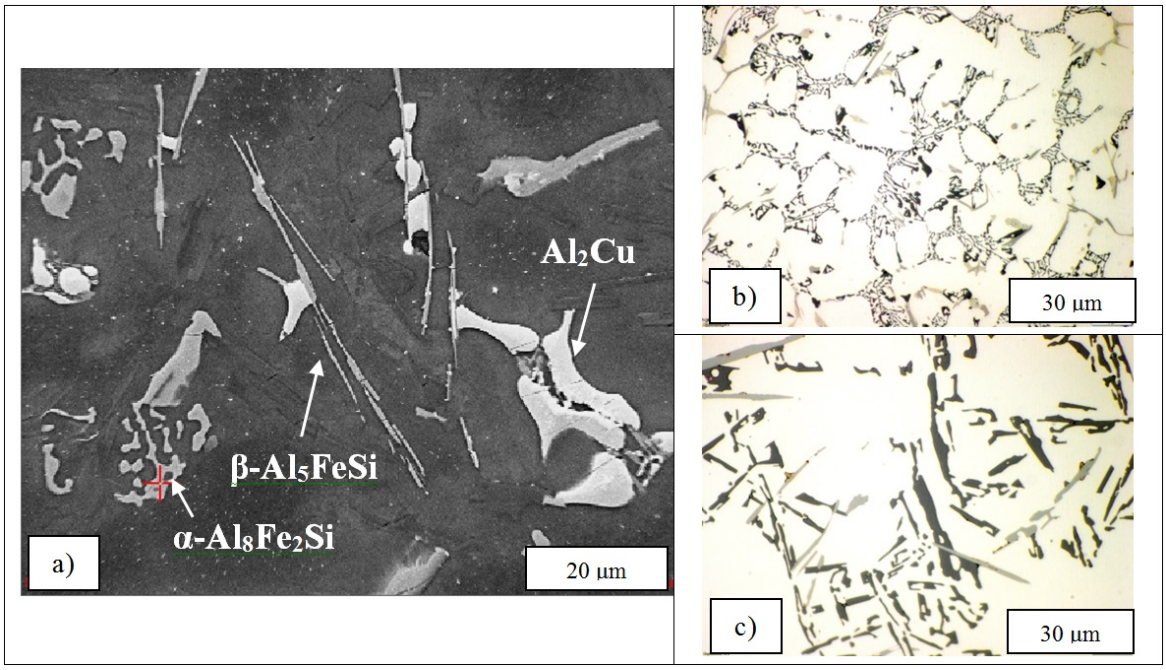

Figure 35. a) Intermetallic phases in as-cast microstructure identified through EDS analysis. Optical photomicrograph showing the effect of cooling rate on the SDAS, size, shape and distribution of eutectic Si in the alloy; b) SDAS 10 µm, c) SDAS 25 µm.

Table 8. Size and morphology of the microstructural features for high and low cooling rates.

Furnace pulling rate (mm/s)	SDAS (µm)	Grain Size (mm)	Si particles, aspect ratio	Al_2Cu, area fraction (%)	Al_5FeSi, length of largest needle (µm)
0.3	25.9 ± 3.4	2.10 ± 0.3	3.91 ± 0.69	1.9 ± 0.5	76
3	10.1 ± 2.3	1.19 ± 0.2	1.73 ± 0.25	2.1 ± 0.3	18

3.3.1.2 Cu- and Mg-bearing phases

The change in microstructure after heat treatment (15 mins.) at various temperatures for both cooling rates is shown in Figure 36. It can be seen that increasing the temperature results in dissolution of the Cu-containing particles (mostly Al_2Cu) formed during solidification. A final polishing step using colloidal silica (OP-S) was used to enhance the Cu-bearing phases, turning their color to one that is readily detectable. The Al_2Cu particles indicated in the 10 µm SDAS samples are completely dissolved after heating to 400 ºC. In the as-cast condition, the Al_2Cu phase is present in the form of both a eutectic phase and a block-like phase. It has been reported that the former dissolves by fragmentation to smaller segments and eventually dissolves by radial diffusion of Cu in the matrix, the latter however dissolves by spheroidization and shrinkage without fragmentation [83].

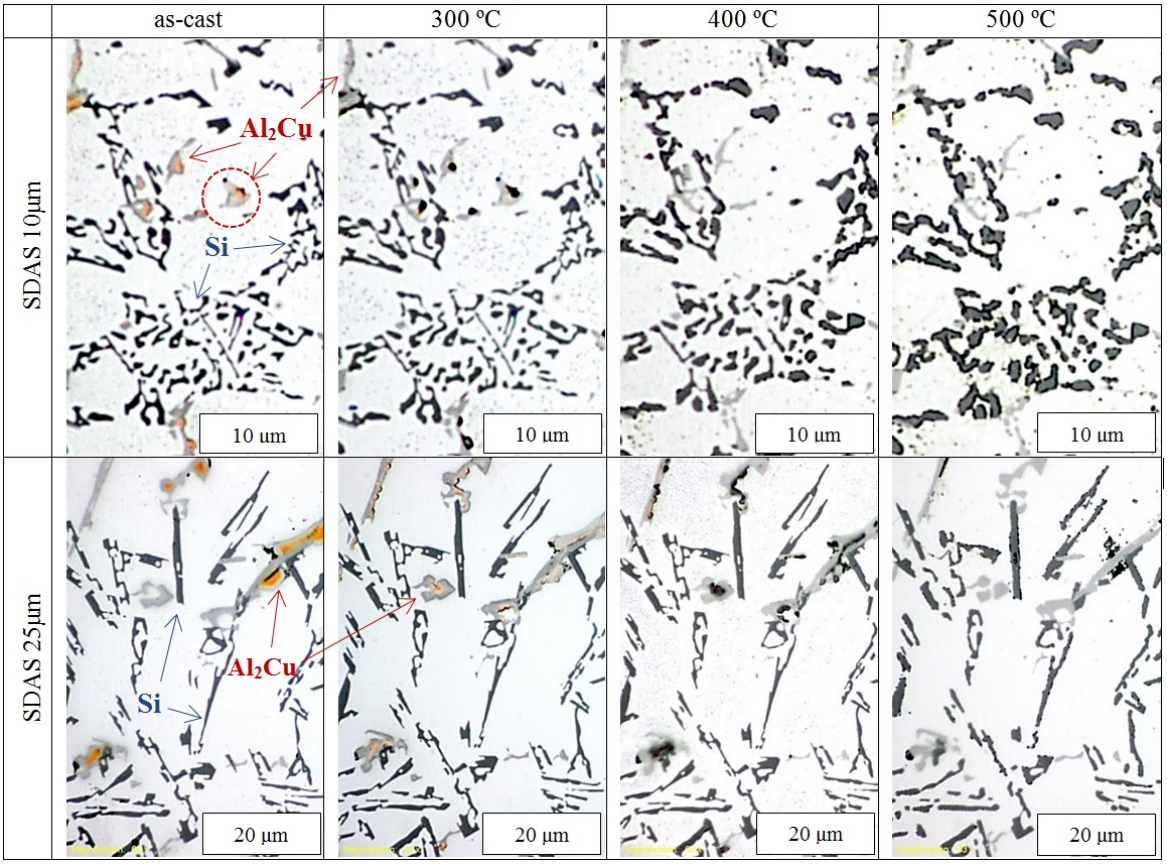

Figure 36. Micrographs after heat treatment at various temperatures for fine (SDAS 10 µm) and coarse (SDAS 25 µm) microstructures.

These two types of Al_2Cu phase are indicated in the coarse microstructure, Figure 36. In order to understand the dissolution of (Cu- and Mg-bearing) phases at elevated temperature, quantitative measurements of solute concentrations were made. Figure 37 shows the concentration of Cu and Mg in the centre of the dendrite arms.

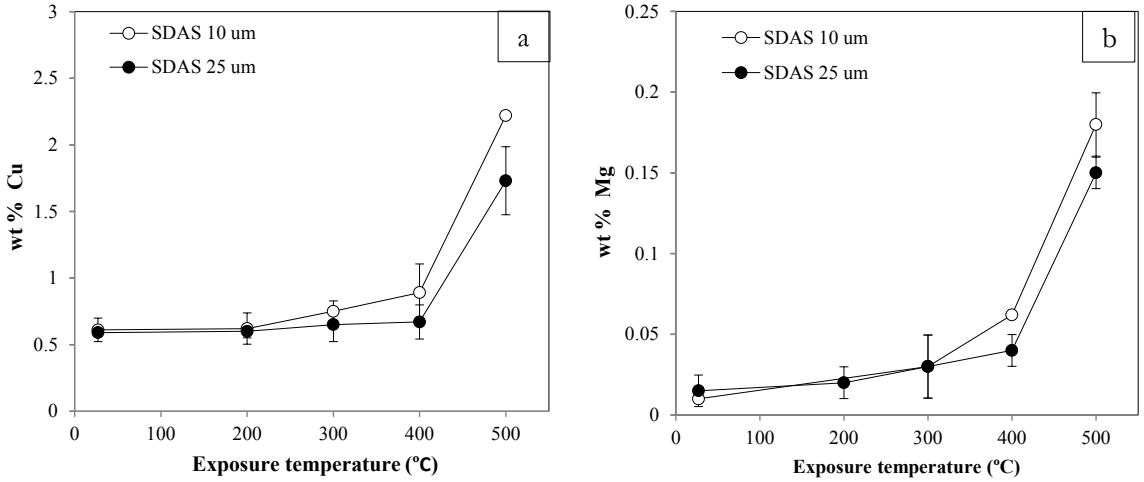

Figure 37. Solute concentration a) Cu and b) Mg at dendrite center measured after exposure to high temperature for SDAS = 10 and 25 µm. The error bars, which are not applied, are just as small as the points. Error bars calculated based on 95% confidence interval. This applies to all of the figures.

The increase in Cu concentration in the dendrite center, illustrated in Figure 37(a) could be a consequence of dissolution of Al_2Cu phase (the most abundant intermetallic) or fragmentation of other Cu-bearing phases such as Q-$Al_5Mg_8Si_6Cu_2$, which is noted in other studies [10, 84]. A large fraction of the Al_2Cu phases in the 10 μm microstructure dissolved at 500 ºC, and the solute concentration reaches 2.22 wt. %. The blocky Al_2Cu particle in the 25 μm microstructure remained stable even after exposure at 500 ºC, suggesting a lower dissolution rate, which is consistent with the lower concentration of Cu (Figure 37 a) compared to the fine microstructure.

The Mg-richest compound, Mg_2Si was rarely found in the micrographs due to the low Mg content in the alloy (0.24 wt. %). Nevertheless Mg could be present in other intermetallic compounds such as π-($Al_8Mg_3FeSi_6$). Figure 37 (b) shows the Mg concentration in the center of the dendrite arms for both SDAS after high temperature exposure. Increased Mg concentration in the dendrite center for both scales of microstructure is thought to be due to dissolution of Mg_2Si and also transformation of π-($Al_8Mg_3FeSi_6$) to β-(Al_5FeSi) and Mg in solid solution [84]. The Mg concentration in the fine microstructure dendrites increases from 0.015 wt. % in the as-cast condition to around 0.9 wt. % at 400 ºC. Figure 37 shows that dissolution of Mg-bearing phases is more pronounced at temperatures above 400 ºC. In the fine microstructure, a large fraction of the available Mg content was transferred to the matrix in the form of a solid solution within 15 min at 500 ºC. The rate of Mg concentration increase was slower for the coarse compared to the fine microstructure as a result of slower diffusion kinetics caused by the longer diffusion distance [84]. It is therefore shown that the rate of dissolution of Cu- and Mg-bearing phases depends on exposure temperature and the size of those phases.

3.3.1.3 Eutectic Si

The morphology of eutectic Si particles at elevated temperature is shown Figure 36. During heating, Si particles spheroidize and then coarsen The change in Si concentration (see Figure 38) suggests a rapid spheroidization rate for fine Si particles (SDAS 10 μm) above 400 ºC. The coarse plate-like Si particles in the 25 μm SDAS microstructure however are less responsive to spheroidization, and demand longer exposure times at a given temperature to become spheroidized. Si particles showed almost no change in their internal architecture below 300 ºC. Coarse Si particles resist coarsening up to 400 ºC. Figure 38 shows that the Si concentration at the center of a dendrite arm at room temperature is lower for the fine microstructure rather than for the coarse one. Increasing the solidification rate reduces the time during which solid state diffusion state may take place which results in a lower concentration of Si in solid solution [85]. The marginally higher concentration of Si in the dendrite of SDAS 25 μm (see Figure 38) may be due to that reason.

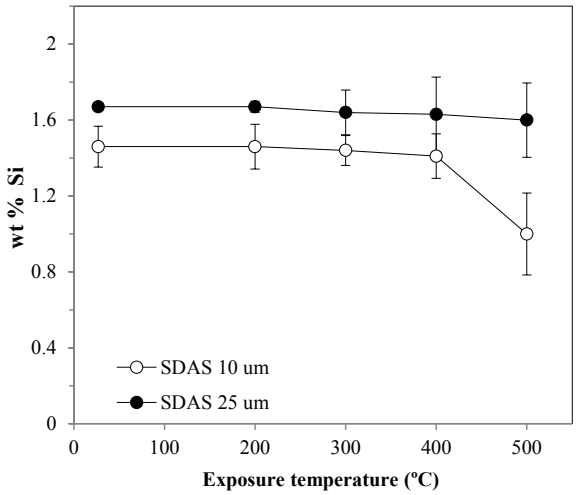

Figure 38. Si concentration in the center of dendrite arms measured after different exposure temperatures for SDAS 10 and 25μm.

According to the Al-Si equilibrium phase diagram [86], Si has a maximum solid solubility in Al of 1.6 wt. % at 576 ºC, which drops to 0.8 and 0.2 wt. % at 500 ºC and 400 ºC respectively. Coarsening of eutectic Si as a result of increased temperature is due to diffusion-controlled reduction of Si in solid solution in the vicinity of the eutectic cells and migration to pure Si particles. The concentration of Si in the center of small dendrite arms (SDAS 10 μm) drops dramatically above 400 ºC, as Si is gradually depleted from solid solution and contributes to coarsening of nearby eutectic Si particles, see Figure 38. Coarse dendrite arms (SDAS 25 μm), however experienced no meaningful change in Si concentration. The larger diffusion distance in 25 μm SDAS is presumed to hinder solute diffusion from the matrix to the particles; and from small to large Si particles. The spheroidization of Si by solution heat treatment is one of the steps of post-solidification processing Al-Si based cast alloys, and hence has been thoroughly discussed in that respect. Nevertheless, it is useful to note that the findings in this work are in agreement with previous studies [84, 87].

3.3.2 Mechanical properties

It is well-known that casting parameters (melt cleaning, oxide films, pores etc.) have marked effects on the tensile properties of Al-Si casting alloys at room and at elevated temperatures [58]. The presence of defects is associated with significantly degraded tensile ductility which consequently shortens the plastic strain region. Such defects prevent the direct determination of stress-strain relations in the plastic region and also result in significant scattering in measured tensile properties [59]. In order to avoid this problem the levels of these defects have been minimized by using the directional solidification technique. Any effects of casting defects have therefore been neglected. Figure 39 shows the R_m, $R_{p0.2}$ and ε_F as a function of temperature for samples with different SDAS. There is a general tendency toward decreasing R_m and $R_{p0.2}$ with increasing temperature due to facilitated dislocation movement [58, 88-91]. The movement of dislocations through a lattice is aided by thermal vibrations. Consequently, resistance to dislocation slip increases as the temperature falls. In Al alloys, room temperature falls in a range between $0.2T_m$ and $0.5T_m$, where the deformation mechanism is usually slip [28]. Figure 39 shows that at temperatures below 300 ºC (~$0.5T_m$), R_m slightly decreases with increasing temperature. However at 300 ºC and above the strength of the alloy degrades steeply. As the temperature increases, the potential for dislocation climb, and dislocation slip increases [28]. The fine microstructure (SDAS 10 μm) displayed superior ultimate tensile strength compared to the coarse microstructure (25 μm SDAS) at RT. This supremacy was retained at temperatures

up to 500 ºC. It was also observed that elongation to failure (ε_F) significantly increases at temperatures above 200 ºC for both coarseness of microstructure. However, the fine microstructure always showed higher ε_F values at any given temperature, Figure 39, and the difference increased with increasing temperature.

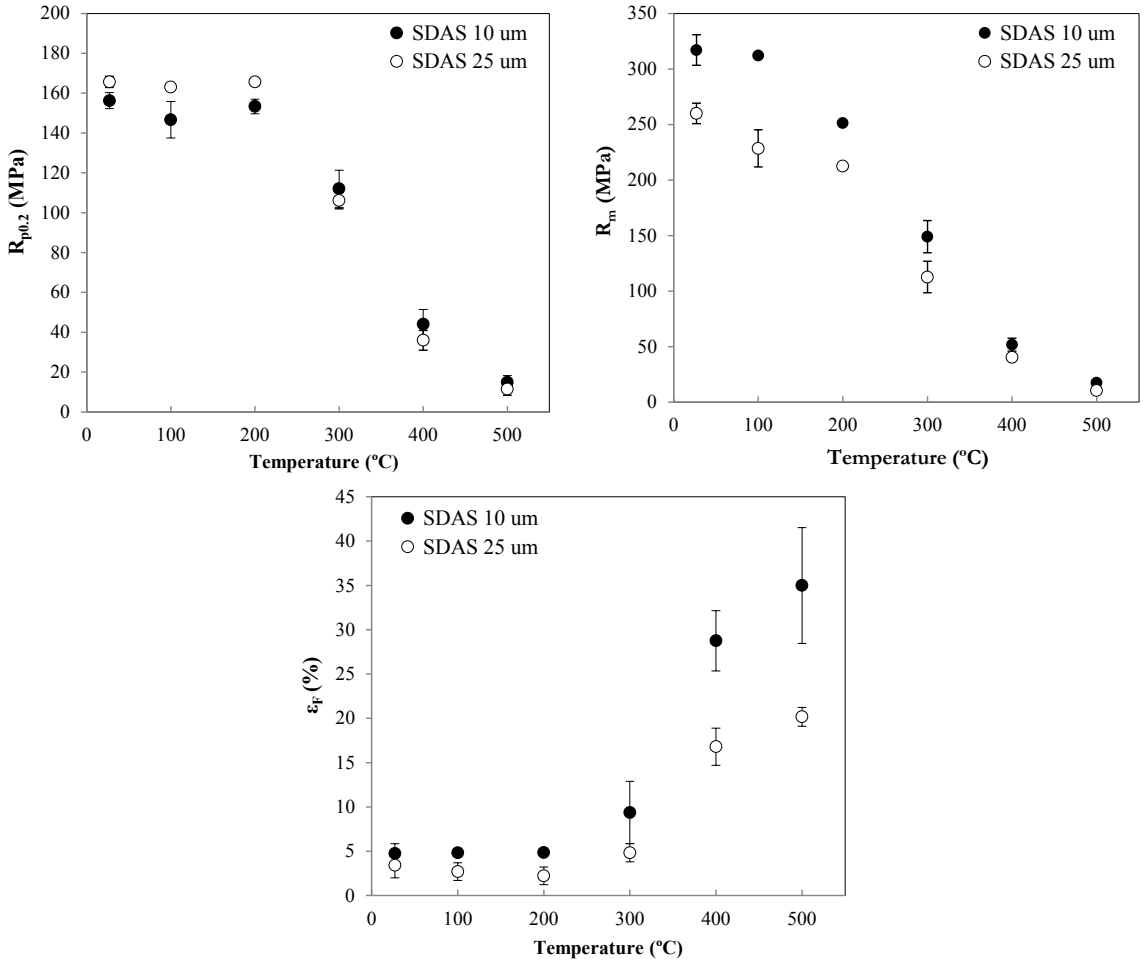

Figure 39. R_m, $R_{p0.2}$ and ε_F values of EN AC-46000 alloy with different SDAS at different temperatures. Strain rate is constant and equal to 10^{-3} s^{-1}.

The contribution of solute level on $R_{0.2}$ of the alloy at room temperature has been well documented. Higher amount of solute results in increased yield strength in Al-Si-Cu-Mg alloys [10, 92]. It was found that $R_{0.2}$ is marginally greater for the case of SDAS 25 μm rather than those in SDAS 10 μm, see Figure 39. Olofsson et al. [4] also reported similar observations comparing SDAS 10 and 25 μm. Figure 37 and Figure 38 show the concentration of solutes in the coarse microstructure is slightly greater in the fine microstructure, which could explain the increase in $R_{0.2}$. In other works, the aspect ratio of Si-particles [81] and size of the eutectic cell [93] were suggested to make a significant contribution to the strength of Al-Si alloys in the early strain regime (<0.003). The contribution of those features however is not pronounced according to the findings of this study. Figure 39 shows that the marked difference in $R_{0.2}$ fades at 300 ºC and above. Neither morphology of Si-particles nor the eutectic cell size showed any indicative change up to 400 ºC. Nevertheless, 300 ºC is the temperature where the significant change in solute

concentration profile initiated, see Figure 37. It is therefore suggested that the yield strength is solely matrix dependent irrespective of the size of microstructural constituents.

Flow stress curves of the alloy at different temperatures for SDAS 10 μm are shown in Figure 40. This shows an increase in hardening rate at 200 ºC in the low strain regime which is apparently due to precipitation hardening. A typical DSC trace for as-cast EN AC-46000 samples, scanned at a heating rate of 5 ºC/min showed an exothermic peak with onset temperature of 206 and 215 ºC for SDAS 10 and 25 μm respectively. The peak evidently corresponds to precipitation of Si from supersaturated solid solution [94]. According to the equilibrium phase diagram, Si has a maximum solubility of 1.6 wt. % at 576ºC in Al, which is lowered to 0.26 wt. % at 400ºC. Results from WDS analysis indicated average concentrations of 1.45 and 1.65 wt. % Si in the α-Al matrix for fine and coarse microstructures respectively, Figure 38. An initial average composition of 1.55 wt. % supersaturated Si was considered as reasonable in the as-cast condition. Increasing the temperature to 200 ºC results in precipitation of Si from supersaturated solid solution and a concomitant increase in strength through precipitation hardening. In a work by Rincon et al. [90], a precipitation hardening behavior was observable in the flow stress curve at 240 ºC in A319 cast alloy.

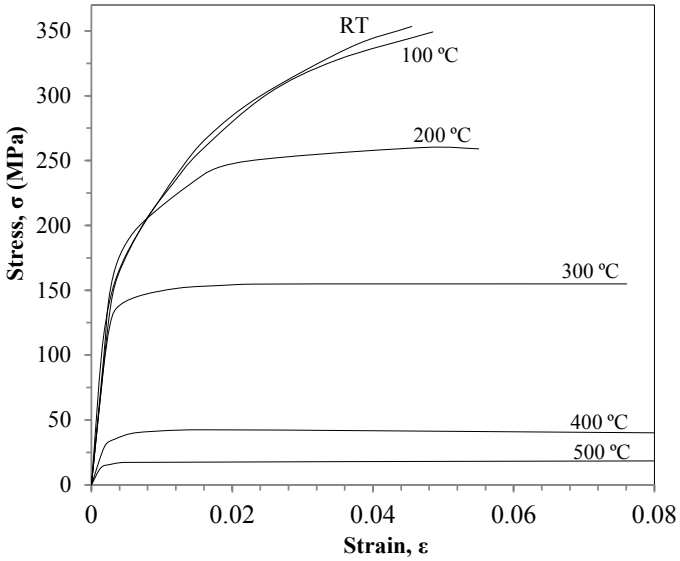

Figure 40. Flow curves corresponding to 10 μm SDAS at different temperatures. SR is equal to 10^{-3} s^{-1}.

Figure 41 shows the strain rate dependency of stress-strain behavior of the alloy at 400 ºC. The flow stress curves showed that the alloy became sensitive to strain rate at 300 ºC and above irrespective of coarseness of microstructure. The strain rate sensitivity (SRS = $\delta\log(\sigma)/\delta\log(SR)$) at constant strain (0.01) was calculated for both coarseness of microstructure. The value of 0.015 ± 0.004 was obtained for both SDAS 10 and 25 μm at 200 ºC and below. The corresponding value rises to 0.12 and 0.11 at 400 ºC for the fine and coarse microstructures respectively ($R^2 > 0.95$). Both coarseness of microstructure retain rather low strain rate sensitivity even at 400 ºC, which is plausible due to the relatively large grain size (~1-2 mm).

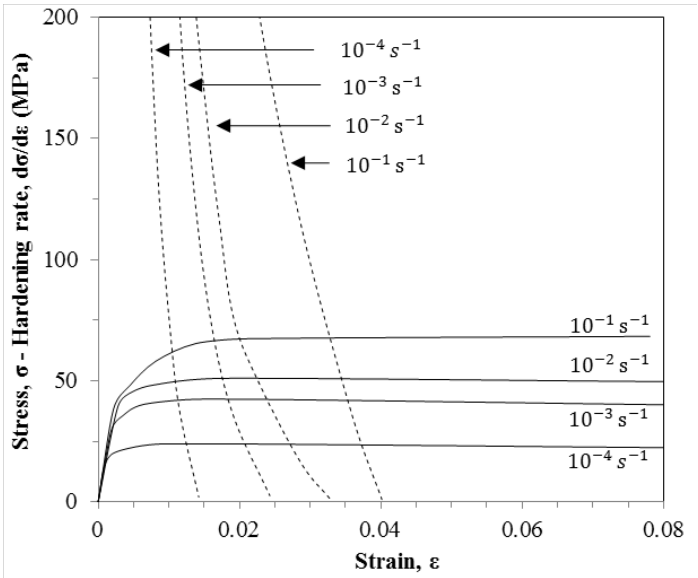

Figure 41. Flow curves corresponding to 25 μm SDAS at 400 ºC obtained under different SR.

An increased strain rate leads to a higher strain hardening rate at 400 ºC and consequently a postponed necking occurrence. Above 0.5 T_m, the dislocation density is determined by the balance between strain hardening and dynamic recovery. Once the rate of straining increases, a higher steady state dislocation density is obtained which leads to a larger saturation stress level [28]. The effect of strain rate disappears upon lowering the temperature due to the trifling rate of dynamic recovery compared to the rate of hardening.

3.3.3 Deformation and fracture behaviour

As long as the level of defects (e.g. gas porosity and oxide films) in cast Al alloys is minimized the failure sequence consists of three consecutive steps; initiation of small damage in particles, damage growth and microcrack formation in the particles, and finally linkage of the microcracks or crack propagation [59, 95]. The failure sequence is illustrated in Figure 42.

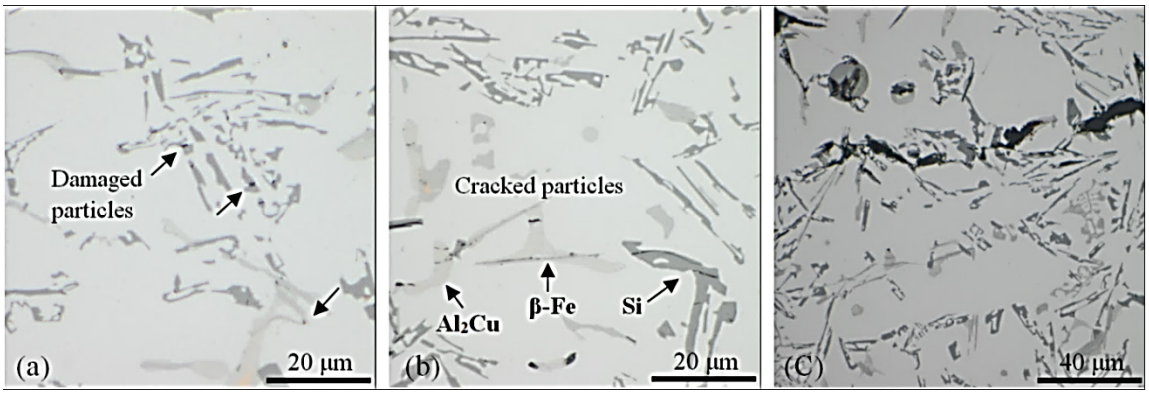

Figure 42. Micrographs showing the failure sequence. a) Damage initiation in particles, b) damage growth and c) crack linkage. SDAS 25 μm, test temperature 100 ºC, SR $10^{-4}s^{-1}$. The tensile axis is horizontal in all images.

In order to assess the role of microstructure coarseness, temperature and strain rate on the failure mechanism, the damage frequency (ratio of damaged/cracked particles over all particles) and area fraction of damaged/cracked particles in failed specimens was

quantitatively measured using image analysis. Measurements were made at room temperature in the central plane over the entire gauge length. Micrographs showed that the majority of cracked particles at any given condition were found in the region close to the fracture surface. Hence, the measurement in that region only was taken into account. Figure 43 shows the fraction of cracked particles as a function of temperature for the fine and coarse microstructures.

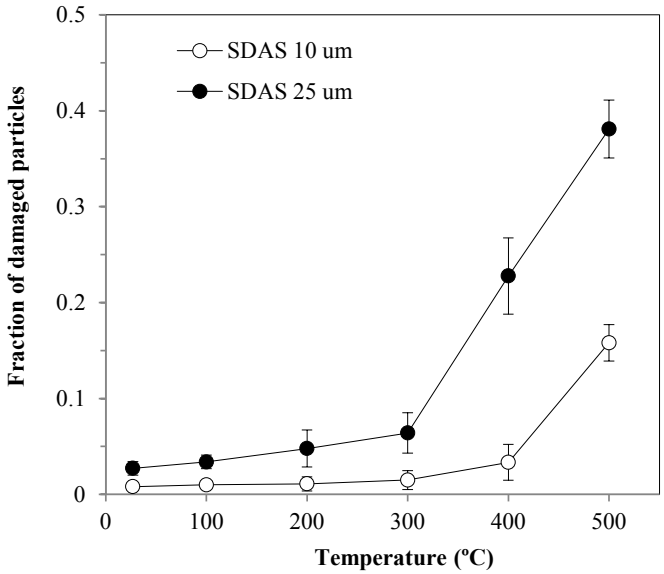

Figure 43. Fraction of damaged particles as of function of tensile test temperature.

It is evident that in the coarse microstructure increasing temperature leads to a monotonic increase in fraction of damaged particles, and the increase becomes significant above 300 ºC. In the fine microstructure however, the fraction of damaged particles below 300 ºC was quite limited (fraction lower than 0.02) and at 400 ºC and beyond, the fraction increased significantly. Plastic flow of the alloy is governed by stress incompatibilities between plastically deformed matrix and elastically strained particles. Once plastic strain in the alloy starts, the brittle second phase particles begin to form microcracks. This continues until a critical strain in which a critical volume fraction of cracked particles is reached, which leads to micro crack coalescence and failure as the matrix between the fractured particles becomes unstable. The process is primarily controlled by microstructure and matrix-properties [88, 95]. As long as the mode of fracture is brittle (below 300 ºC) particles dominate the microcracks linking process. As the matrix softens at higher temperatures, the matrix properties begin to play a role in the failure process. Raising the temperature may reduce the matrix instability between the fractured particles and microcracks. On the other hand, the stress induced in particles during matrix deformation will be intensified which leads to further particle damage and void formation. The end result is an increased fraction of fractured particles and increased strain. This trend was clearly seen in the coarse microstructure of this study (SDAS 25 μm in Figure 43). Rincon et al. [90] reported that increasing the temperature from 250 ºC to 400 ºC leads to an increase in fraction of cracked particles from 12 % to 50 % in an Al8Si3CuMg cast alloy having SDAS in the range 24-36 μm, which is in agreement with the findings of this work. Mahidhara & Mukherjee [88] also reported that as eutectic Si particles in a Al-Si eutectic alloy become coarser, the level of cavitation at the matrix-Si particle interface was significantly increased at 558 ºC.

Inter-particle cracking is a function of size, aspect ratio and type of particles as well their orientation with respect to the direction of applied load. Since larger defects and voids are allowed to exist in larger particles, they have a lower fracture stress and in turn they fracture promptly, as suggested by Wang et al and Hunt [96, 97]. In the microstructure with SDAS 25 µm, damage initiates more readily in elongated particles rather than in particles having a smaller aspect ratio. Particles in the fine microstructure (SDAS 10 µm) were however less prone to damage, as they have a smaller and less scattered aspect ratio, see Table 8. This is supported by the fact that higher aspect ratio particles accumulate stress at a faster rate and accordingly tend to crack earlier, as suggested by Wang [81]. It was observed that the fraction of damaged Al2Cu and β-Al_5FeSi particles was higher than the fraction of damaged Si particles. This was also noticed in another study [90]. However, in the present study no quantitative measurement was done to distinguish secondary particles according to type.

Figure 44 shows SEM micrographs of the fracture surface of the two microstructures which were strained to failure at room temperature, 300 and 400 ºC. It is obvious that the coarse microstructure experienced brittle fracture at 300 ºC and below due to the presence of large plate-like brittle phases. Rapid fracture of coarse particles and intergranular propagation of microcracks shield the matrix from plastic deformation (Figure 44 d and e). Lack of plasticity (

≤5 %) suggests that the cast alloy with SDAS 25 µm is in

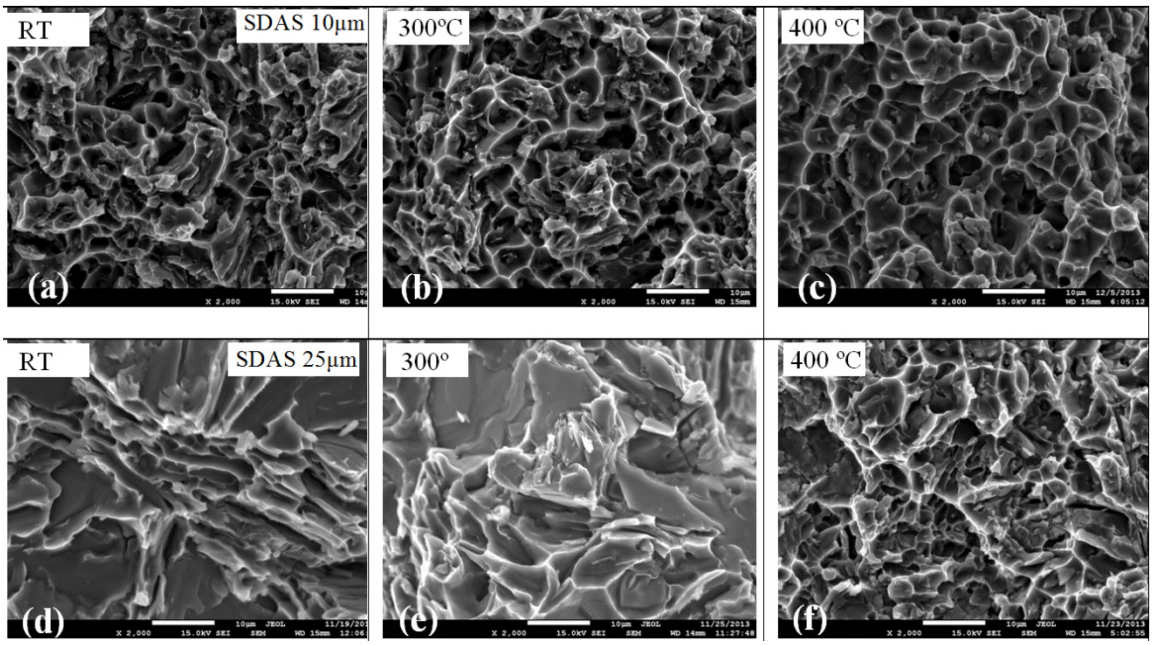

Figure 44. SEM micrographs of fractured surfaces of the alloy with SDAS 10 and 25µm tested at different temperatures. SR is equal to 10^{-3} s^{-1}.

Figure 45 shows the tensile instability behavior of the alloy with fine and coarse microstructure at temperatures of 200 ºC and 300 ºC. Below 200 ºC, the derivative of the curves does not meet the flow curves of the fine microstructure suggesting that brittle failure occurred at this temperature. The accumulation of damage in particles leading to failure takes place prior to necking. At 200 ºC and above however, the instability criterion is met, indicating that 200 ºC marks the brittle to ductile failure transition temperature. In the coarse microstructure, the instability criterion is satisfied at 300 ºC, see Figure 45. At 400 ºC the coarse microstructure shows the typical dimples of ductile fracture and multiple cracked particles in the fracture surface. In contrast, the fracture surface of the fine microstructure

tested at room temperature contains ductile dimples, see Figure 44a. The number of dimples was significantly increased at 300 ºC, proving the fully ductile fracture above 200 ºC, which is a consistent finding based on instability criteria. In a similar study to this [58], it was found that A319 alloy softens in the interval of 270 to 320 ºC, where SDAS ranged from 20-50 μm which agrees well the results for the case of SDAS 25 μm.

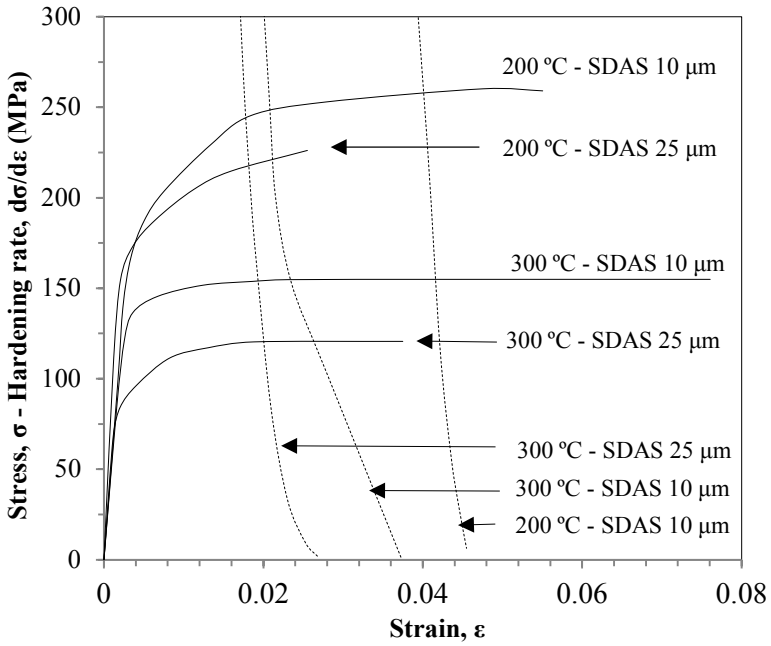

Figure 45. Tensile instability plots of the alloy at 200 and 300 ºC; for SDAS 10 and 25 μm. SR is equal to 10^{-3} s^{-1}.

In a study by Wang [81] it is suggested that in alloys with large SDAS, the failure occurs prior to necking at RT as a result of the high damage accumulation rate caused by particle cracking. In small SDAS samples however, necking takes place below the fracture strain. The comparison was made between 17 and 54 μm SDAS in A356/357 alloy. It is therefore feasible that in the coarse microstructure damaged particles (Si, Al_2Cu and β-Al_5FeSi etc.) cause premature failure but that this is deferred to a higher temperature (300 ºC) when necking occurs due to increase matrix plasticity. In the fine microstructure however, post-necking damage through particle cracking apparently takes place at 200 ºC. Results of tensile instability in the fine microstructure do not agree with the suggestion by Wang [81]. This contradiction may be due to the higher level of Si (10 wt. %) and the presence of Cu (2.6 wt. %) in the EN AC-46000 alloy, which limits the intrinsic ductility of the matrix. The tensile instability point of the fine and coarse microstructure approaches the same value at higher temperature (above 400 ºC), indicating that necking occurrence is determined by stress relaxation during plastic deformation instead of damage accumulation in particles [58].Two typical modes of damage accumulation found in the present study are single micro cracks and microcrack clusters, see Figure 46c and d.

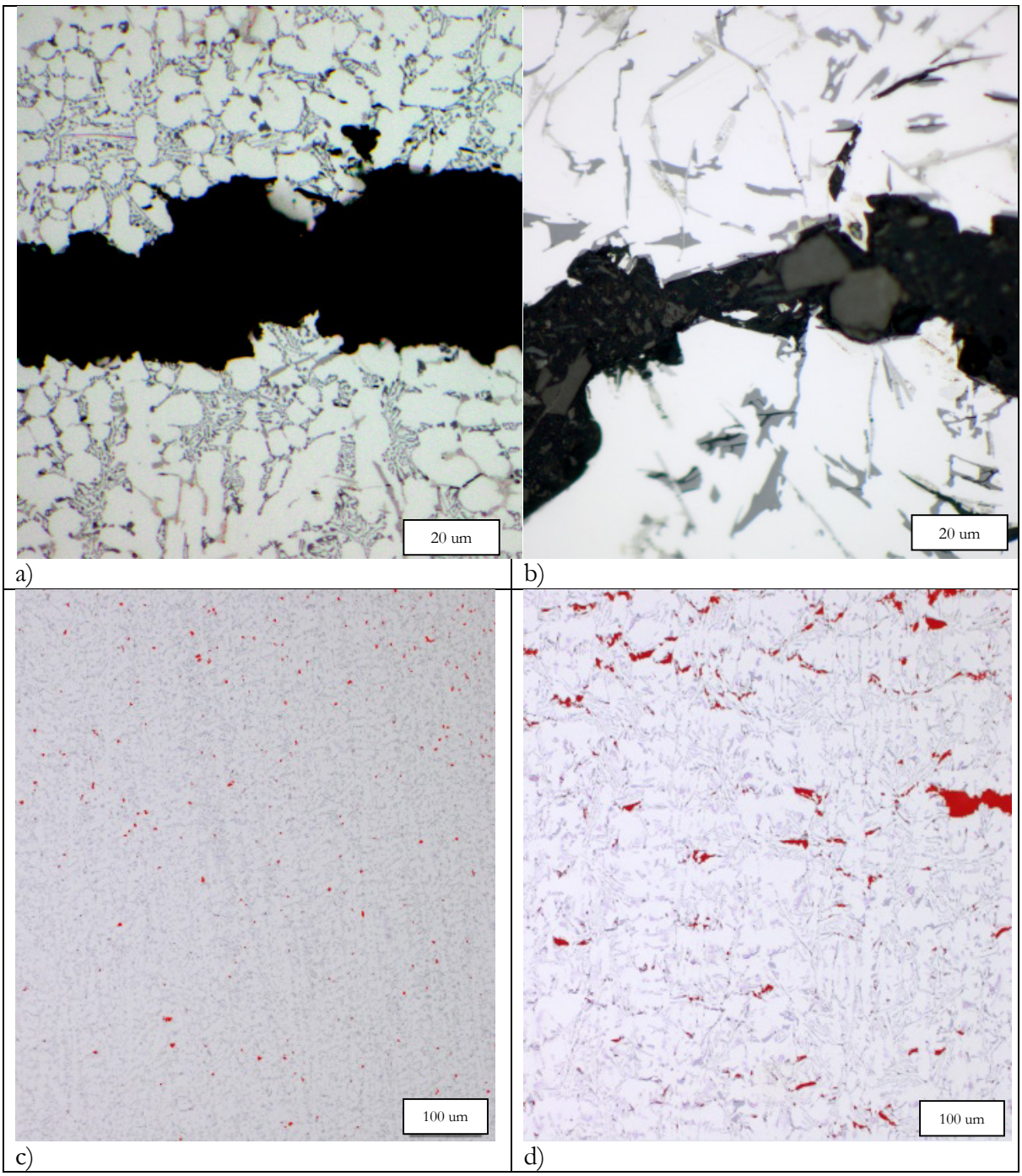

Figure 46. Optical micrographs showing fracture path of failed specimen a) SDAS 10 µm, RT, 10^{-2} s^{-1}, b) SDAS 10 µm, RT, 10^{-2} s^{-1}; c) single microcrack and d) microcracks clusters at RT, 10^{-2} s^{-1}.

It has been proposed that the rate of damage formation in single particles at different strain is approximately constant. The accumulation of damage in particles however is rare at low strain levels and becomes significant as the fracture strain is approached [97]. Figure 47 shows the area fraction of fractured particles and cavities as a function of strain rate at 500 ºC for different microstructure coarseness.

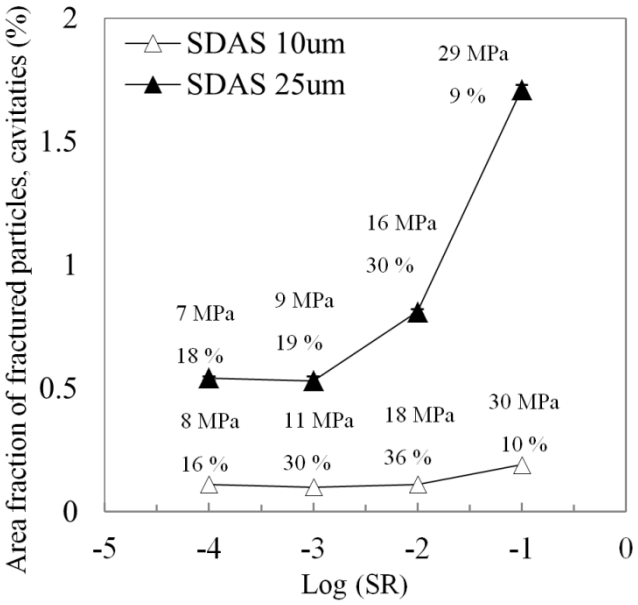

Figure 47. 2D Area fraction of fractured particles and cavities at particle/matrix interface as function of strain rate at 500 ºC. The corresponding elongation to failure and UTS are indicated for each case.

It was observed that at 500 ºC increasing the strain rate from 10^{-3} to 10^{-1} s^{-1} profoundly increased the area fraction of fractured particles for the coarse microstructure. The trend was not as clear at 400 ºC and no trend was found at lower temperature, nor was this trend evident for the fine microstructure. This suggests that the cleaving rate of the particles which are already fractured at lower strain levels is related to a thermally activated stress relaxation mechanism such as dislocation climb. Increasing the strain rate leads to a higher dislocation density [28] and accordingly an increased number of dislocations enhances the probability of interactions with particles. Micrographs suggest that an increase in the area fraction of damaged particles includes more frequent microcrack clusters and single cleaved particles. However, no meaningful trend was observed between the strain rate and elongation to failure at 500 ºC (see Figure 47) or any other test temperatures. This is consistent with somewhat lower ductility of the alloy at higher strain rate (due to the increased probability of microcrack aggregation). The higher strain rate leads to instability in plastic deformation at higher strength and strain at elevated temperature (above 400 ºC) see Figure 41. Extended local uniform plastic strain at high strain rates resulted in opening of microcracks and shattering of cracked particles without any pronounced initiation of damage in the particles. Localized shear bands formed in the matrix at the edge of microcracks (mostly inside the grains) provide an opportunity for fractured particles to grow [95]. Mahidhara & Mukherjee [88] report quite the opposite observation for an Al-13Si wrought alloy deformed at 557 ºC under different strain rates. It was qualitatively observed that by reducing the strain rate from 10^{-2} to 10^{-5} s^{-1}, the numbers of cavities - particularly in grain boundaries – surprisingly increased and elongation to failure monotonically decreased. Their observation is however not consistent with the findings of the current study. Unlike the Al-13Si wrought alloy [88] in which the grain size ranged from 15-35 μm, grain boundary sliding is not a plausible deformation mechanism in the EN AC-46000 alloy which has a grain size of around 1-2 mm. Therefore, the higher rate of straining does not necessarily facilitate grain boundary sliding and consequently improved plasticity. Another reason which may be relevant is the inevitable uncertainties related to the mode of processing (e.g. casting defects). Since the samples are in the as-cast condition, their plasticity severely suffers from such defects.

3.4 THE MODELLING BEHAVIOUR OF THE EN AC-46000 ALLOY

3.4.1 The constants of the model

In order to develop the model for the prediction of the deformation behaviour of these materials, a number of parameters have to be derived from the experimental flow curves as well as data related to the alloy which is extracted from the literature and summarised in Table 9. The constants were chosen either for Al-Si alloy or for pure Al based on availability in the literatures. The Taylor factor (m) is corresponding for Al alloy including the effect of alloying element addition [43, 98]. Self-diffusion activation energy (Q_v) for Al-Si interdiffusion is equal to 148.6 kJmol^{-1} [45, 99, 100], while the self-diffusion activation energy for pure Al = 140 [45], in current model the value close to the average was considered. The value for initial vacancy diffusivity (D_{vm}) corresponds to pure Al [45], however the values reported for Al alloys are in the same range [99, 101]. The constant for the entropy of vacancy formation (ΔS_{vf}) corresponds to FCC metals [102].

Table 9. The parameters which were used in the model.

Parameter	Notation	Value	Dimension	References & Comments
Boltzmann's constant	k	1.38×10^{-23}	JK^{-1}	
Melting temperature	T	660	°C	[86]
Taylor factor	m	3.06	-	[43, 98]
Atomic volume	Ω_0	1.66×10^{-29}	m^3	[45]
Burger 's vector	b	2.85×10^{-10}	m	[103]
Young's modulus at room temperature	E	65	GPa	from tensile test
Shear modulus	G	12.7	GPa	[104]
Poisson's ratio	υ	0.33	-	
Self-diffusion activation energy	Q_v	140	kJmol^{-1}	[45, 99, 100]
Activation energy of vacancy formation	Q_{vf}	74.3	kJmol^{-1}	[100, 105]
Energy barrier for vacancy migration	Q_{vm}	65.7	kJmol^{-1}	$Q_v = Q_{vf} + Q_{vm}$
Initial vacancy diffusivity	D_{vm}	1.71×10^{-4}	m^{2}s^{-1}	[45]
Pipe diffusivity	D_{p0}	4.0×10^{-5}	m^{2}s^{-1}	[45]
Reference strain rate	$\dot{\bar{\varepsilon}}_{ref}$	10^6	s^{-1}	[106]
Increased entropy upon creating a vacancy	ΔS_{vf}	1.92×10^3	JK^{-1}	[102]
Fraction of mechanical work for vacancy formation	χ	0.1	-	[52]
Formation energy of thermal jogs	Q_{fi}	3.53×10^{-20}	J	[52]
Neutralisation effect by vacancy emitting and absorbing jogs	ς	10	-	[52]
Initial immobile dislocation density	ϱ_{i0}	10^{12}	m^{-2}	[106]
Equilibrium vacancy concentration	c_v^{eq}	3.04×10^{-5}	-	[107]

3.4.2 The addition of a scaling factor

Addition of Si to Al decreases the vacancy formation energy [108] and increases the concentration of vacancies particularly near the Si solute atoms [54]. The generation, motion and interaction of vacancies are coupled with the diffusion of solute atoms and hence dislocation recovery. The current model considers the material as a mono-phase matrix containing reinforcing particles (e.g. precipitates). The role of the Si solute during hardening has been considered through equation (2) as the parameter Δf_0. However the interaction with vacancies, their effect on excess vacancy formation and on vacancy annihilation processes has not been considered in the initial model. Therefore a correction term was added to provide a better description of the recovery process assisted by vacancy formation. Using the relation proposed by Lomer [54], the interaction between Si solute atoms and vacancies can be estimated (equation 7):

$$\frac{X_{vac}^{Al-Si}}{X_{vac}^{Al}} = 1 - ZX_{Si} + ZX_{Si}\exp\left(\frac{E}{kT}\right) \qquad (7)$$

where Z is the coordination number, X_{si} is concentration of solute, E (J) is the vacancy-Si binary interaction energy in Al, and k (JK^{-1}) is Boltzmann's constant. The concentration of solute in the matrix (X_{si}) was measured using WDS technique. X_{si} (the value for SDAS 10 and 25 μm) was then given as 0.014 and 0.015 respectively, Z was set to 12 (for FCC materials [54]) and E was set to 1.6×10^{-19} [109]. The value of c_v^{eq} which is the corresponding value for Al in equation (5) is then multiplied by the correction scale, equation 7. Figure 48 shows the influence of the correction scale addition on the predicted flow curve.

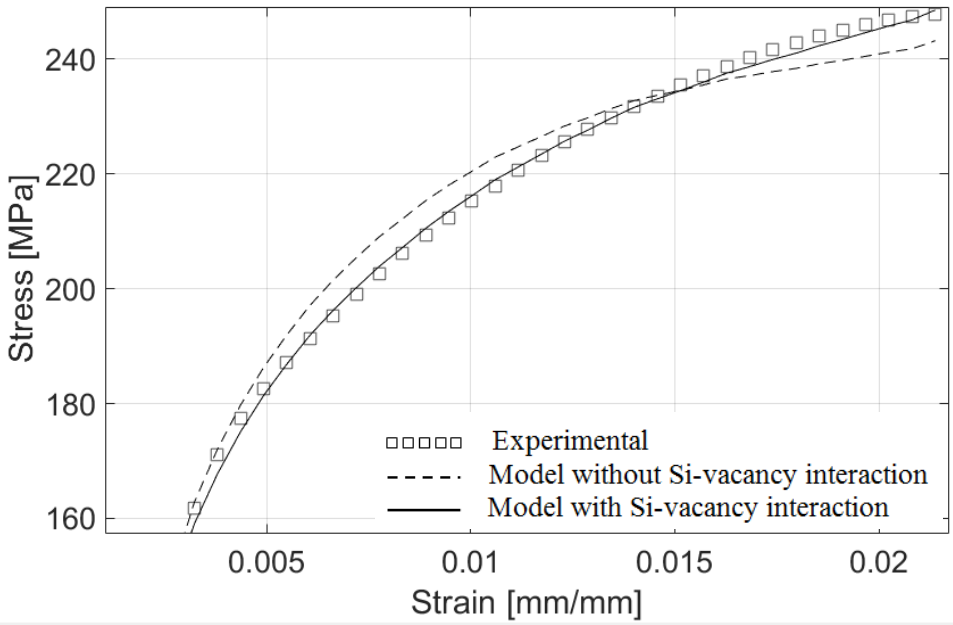

Figure 48. The calculated flow curve with and without the correction factor. SDAS 10 μm at 200 °C. Strain rate is equal to 10^{-4} s^{-1}.

The value of the correction varies from 10^7 to 10^{16}, which means a significant increase in the equilibrium vacancy concentration. This increase primarily facilitates the annihilation process, which opposes the hardening process. The trend can clearly be observed in Figure 48 in strain ranges from 0.005 to 0.015. The correction resulted in a more precise description of the flow curves under all conditions; however the level of improvement in fitting was different from case to case.

3.4.3 Calibration of stress–strain curves

The tensile test results for the materials tested in various conditions are presented in Figure 49 andFigure 50. The role of microstructural coarseness (SDAS), strain rate and testing temperatures are clearly demonstrated. Typical experimental and predicted flow stress curves, are plotted in Figure 49 and 4. Curves corresponding to different coarseness of microstructure (SDAS 10 and 25 µm) and the Sr-modified microstructure at different temperature are plotted in Figure 49. The influence of strain rate can be observed in the series of curves in Figure 50.

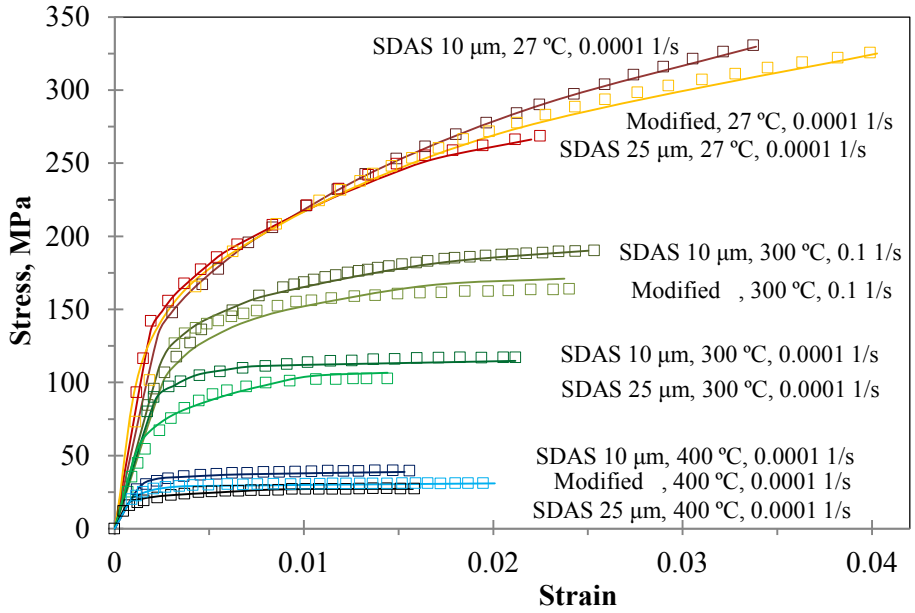

Figure 49. Measured and calculated flow stress curves for unmodified (SDAS 10 µm and 25 µm) and modified alloys from ambient temperature to 400 ºC.

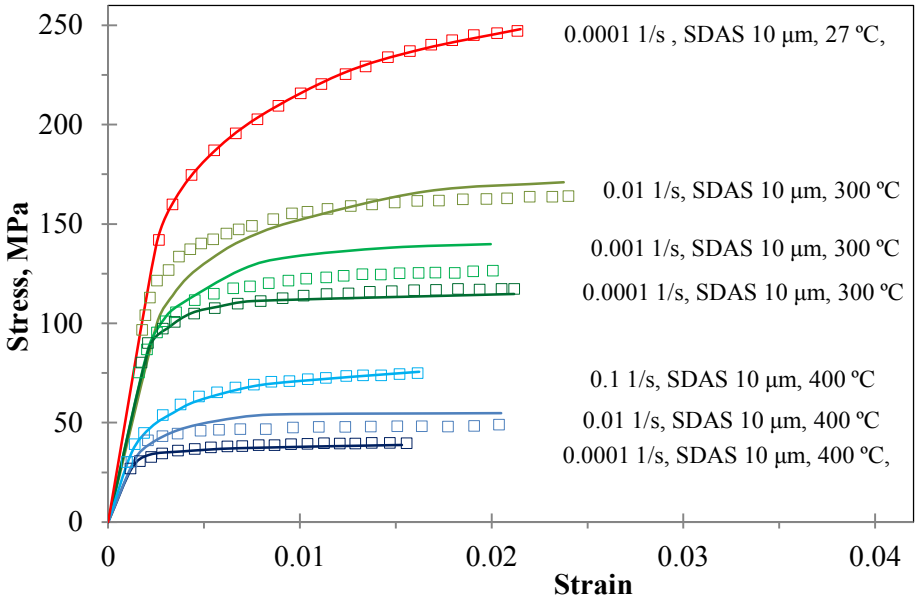

Figure 50. Measured and calculated flow curves for SDAS 10 µm at strain rate of 10^{-4} to 10^{-1} from 200 to 400 ºC.

The measured values have been smoothed in order to remove serrations due to measurement noise. The hollow squares show the experimental data, while the solid lines indicate the

calculations using the material model. The overall matching shows quite promising agreement between the experimental and computed flow stress curves for any given test conditions. This is primarily due to the addition of a correction term which includes the effect of solute concentration in the α-Al, see equation 7. This influences the initial hardening stage ($\varepsilon < 0.02$) and consequently alters the shape of the flow stress curves [110]. However, there is still some deviation between the measured and calculated data, particularly for the case of SDAS 10 μm. This may be due to experimental errors in the furnace temperature, or gauge length misalignment of the laser extensometer. It should be noted that although the test samples experienced quite large strain deformation, especially above 300 ºC, the model used the experimental data obtained before tensile instability occurred. The parameters from the model which are temperature and microstructure dependant are listed in Table 10.

Table 10. Calibrated parameters as a function of temperature for different as-cast condition.

Parameters	T (ºC)	27	100	200	300	400
τ_0	SDAS 10 μm - Modified	0.0078	0.0079	0.0114	0.0144	0.0140
	SDAS 10 μm - Unmodified	0.0072	0.0086	0.0127	0.0128	0.0127
	SDAS 25 μm - Unmodified	0.0085	0.0090	0.0118	0.0138	0.0118
Δf_0	SDAS 10 μm - Modified	0.839	0.859	1.184	1.077	0.855
	SDAS 10 μm - Unmodified	0.856	1.031	1.258	1.279	1.077
	SDAS 25 μm - Unmodified	0.957	0.923	1.078	1.094	1.099
Ω	SDAS 10 μm - Modified	44.3	60.1	79.7	144.0	259.0
	SDAS 10 μm - Unmodified	45.9	75.1	119.1	146.7	256.2
	SDAS 25 μm - Unmodified	48.5	62.9	115.0	146.6	249.1
K_c	Modified: 25	SDAS 10 μm : 29		SDAS 25 μm : 23		
c_γ	Modified: 0.31	SDAS 10 μm : 0.63		SDAS 25 μm : 0.05		
α	1.42					

3.4.4 Validation of temperature dependent variables of the model

The present model assumes the material is a single-phase deforming matrix containing reinforcing particles. The parameter τ_0 controls the quality and magnitude of the effect of reinforcing particles during the hardening process. The quantity τ_0 equation (5) is athermal stress related to the strength of precipitates in the matrix. The values of τ_0 are relatively low (<0.013) compared to the values for Al5Mg wrought alloy (0.013-0.06) [40] and Ti6Al4V (0.1 - 3.5) [111]. This suggests that the precipitate contribution to the yield strength is low at all temperatures. Figure 51 shows the quantity of τ_0 as a function of temperature for both SDAS 10 and 25 μm (solid lines). It is seen that τ_0 value increases at temperatures above 200 ºC, which suggests that the contribution from precipitated to the yield strength increases.

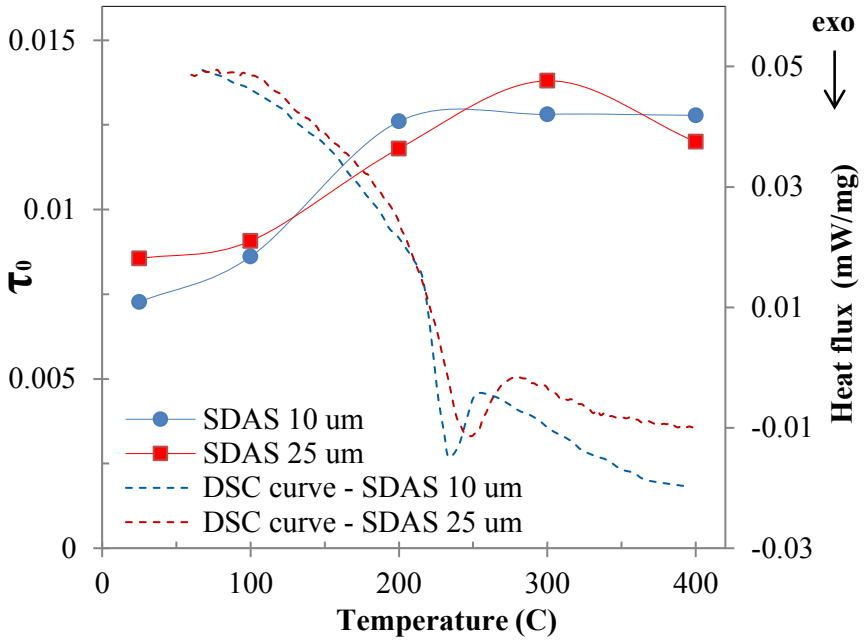

Figure 51. The τ_0 as a function of temperature, and DSC thermograms of the alloy with SDAS 10 and 25 μm

According to the equilibrium phase diagram, Si has a maximum solubility in Al of 1.6 wt. % at 576 °C, which is lowered to 0.26 wt. % at 400 °C. The WDS analysis indicated 1.45 ± 0.10 wt. % Si in the α-Al dendrites for both coarseness of microstructure. An initial composition of 1.5 wt. % supersaturated Si was assumed for the as-cast condition. Typical DSC traces obtained during heating show an exothermic peak in the temperature range of 200-300 °C which corresponds to Si precipitation [94], Figure 51. The kinetics of Si precipitation is closely linked to the amount of excess vacancy [112, 113]. A considerable fraction of the vacancies form a significant number of loops which act as heterogeneous nucleation sites for precipitation of Si atoms [114, 115]. The formation of Si precipitates explains the intensified effect of the reinforcing particle on hardening, which is reflected as the increase in the magnitude of τ_0. However, as it was mentioned earlier the values of τ_0 is quiet small suggesting that the contribution of particles (e.g secondary particles and precipitates) in hardening process in short strain regime is negligible.

The quantity Δf_0 is the activation energy to overcome lattice resistance or obstacles without aid from external stress [43]. The temperature variations in Δf_0 prove that the short-range stress σ^* is influenced by temperature changes. The variation however is not significant, and the Δf_0 values for different microstructure are approximately constant.

The Ω parameter describes the recovery process induced by dislocation glide and annihilation, equation (4). The optimized Ω values were increased by increase in temperature, with quite similar trends for the different microstructures. The inverse dependency of Ω with temperature is plotted in Figure 52, showing an exponential relationship, $\Omega = A\exp(-Q_{\text{dislocation-glide}}/RT)$ where A is an empirical constant, R is the gas constant and $Q_{\text{dislocation-glide}}$ is the activation energy for dislocation glide. The corresponding activation energy

for dislocation glide was calculated to be in the range of (6-7 kJ/mol) which is quite a low value. The corresponding value found to be order of 10 $kJmol^{-1}$ for the Al5Mg alloy [40] which rather same range of this study. Roter et al. [98] indicated that the activation energy for dislocation glide could be expected to be low as the activation energy for particle cutting which is of the order $Gb^3/4\pi$ (31 kJ/mole for this case).

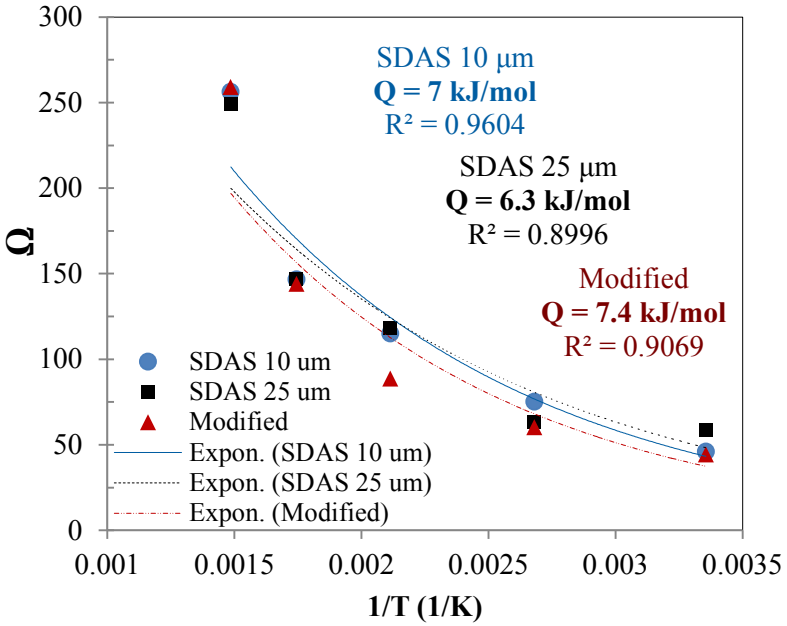

Figure 52. Ω as a function of temperature for different microstructures.

CHAPTER 4

CONCLUDING REMARKS

CHAPTER INTRODUCTION

This chapter summarizes the highlighted conclusions which were made from this study.

Two systems of Al-Si based casting alloys were studied in this thesis; Al-12 Si (EN AC-44300) and Al-Si-Cu-Mg (EN AC-46000). The effect of the casting defects (in particular porosity) on tensile properties and failure characteristic of EN AC-44300 alloy cast by high pressure die casting and gradient solidification technique was studied. The effect of cooling rate refinement and Sr-modification on porosity formation, microstructure and mechanical properties of EN AC-46000 alloy were investigated. Different approaches were examined in order to assess the level of Sr modification and find the optimum content of modification agent. The microstructural evolution and deformation behaviour of EN AC-46000 alloy comprising two distinctive coarseness of microstructure in the temperature range of room to 500 ºC were studied. A physically based model was adapted and improved in order to describe flow stress curves of the alloy cast under different conditions. The following conclusions are highlighted from the work:

Casting defects

The gradient solidification set-up was proven to be a reliable technique to (i) produce the as-cast specimens with comparable microstructure and having low level of defects and (ii) predict the full potential of tensile properties of the alloy. The tensile strength and ductility of the EN AC-44300 dramatically decreased with the increase of volume fraction of pores.

Sr modification & coarseness of microstructure

Coarseness of microstructure has a close relation with tensile properties. When the SDAS increases from 10 to 50 μm, both tensile strength and fracture strain drastically decreased. The Fe-bearing intermetallic compounds play an active role on failure process of the EN AC-46000 alloy, especially in coarser microstructure (SDAS>20 μm). Addition of around 280 ppm Sr to the alloy changes the eutectic Si-particles morphology from coarse plate-like (unmodified) to fine fibres (fully modified). This cetain Sr amount is needed to achieve a fully modified structure, but exceeding that may lead to the formation of undesirable phases such as Al_2Si_2Sr. Sr modification may improve the ductility of the alloy to a great extent as long as the size and morphology of Fe-bearing phases are controlled (e.g. through the cooling conditions). In this case eutectic Si-particles make a significant contribution during crack propagation.

No correlation was found between modification treatment and additional porosity formation. An objective and precise approach was suggested to assess the modification level of Sr in the alloy and subsequently find the optimum Sr content for modification. Sr content in the alloy was found to be strongly correlated with the depression of the eutectic growth temperature.

High temperature deformation behaviour

The tensile properties (R_m, $R_{p0.2}$, and ε_F) of EN AC-46000 alloy were largely dependent on temperature. Ductility increased significantly above 300 ºC, even for the case of coarse microstructure (SDAS 25 μm). R_m consistently decreased with increasing temperature for the case of SDAS 10 and 25 μm. The brittleness of the alloy below 300 ºC was related to accumulation of a high volume fraction damaged particles such as Fe- and Cu-bearing phases and Si-particles. The initiation rate of damage in the coarse particles was significantly higher, which enhances the probability of failure and decreases both R_m and ε_F compared to the fine microstructure. The fraction of cracked particles was found to be a function of temperature. The coarse microstructure is more sensitive to crack formation at any given temperature. The area fraction of damaged particles was significantly increased at high strain rate (10^{-1} s^{-1}) at 500 ºC. No meaningful relation between the fraction of damaged particles and strain rate was found at any temperature.

The concentration of Cu and Mg in the dendrites increases as the temperature exceeds 300 ºC. The increase becomes significant above 400 ºC. The rate of dissolution of Mg- and Cu-bearing phases is higher in the alloy with fine microstructure. Spheroidazation of eutectic Si particles occurred above 400 ºC and the rate was greater in the fine microstructure alloy. The strain rate effects on tensile behaviour were not significant below 200 ºC for both SDAS 10 and 25 μm. The effect of strain rate became more important at 300 ºC where the flow stress of the alloy decreased dramatically. At this temperature and above, strain rate has a marked effect on R_m. The effect on the flow stress curve became even more highlighted at 400 ºC and above. Four order of magnitude increase in strain rate at 500 ºC (from 10^{-4} to 10^{-1} s^{-1}) resulted in a higher flow stress, even when the temperature was 100 ºC lower (10^{-4} s^{-1} at 400 ºC).

The modelling flow stress behaviour of EN AC-46000 alloy

A physically-based dislocation model with the interaction between dissolved Si and vacancies was optimized to describe the as-cast yield stress of EN AC-46000 casting alloy. This is the first time a model has been developed for an Al-Si-Cu-Mg casting alloy and describes the tensile behavior of the alloy from ambient temperature up to 400 ºC and strain rates from 10^{-4} up to 10^{-1} s^{-1} and containing different scales of microstructure. The correction improved the accuracy of the predicted the flow stress curves. The contribution of particles (e.g secondary particles and precipitates) in hardening of the alloy in short strain regime is negligible holding is quiet small τ_0 values at all temperature range. It is therefore plausible to employ the mono-phase material model for the prediction of such alloy having large secondary particles.

CHAPTER 5

FUTURE WORK

CHAPTER INTRODUCTION

Based upon the results and findings of high temperature deformation behaviour of the Al-Si alloy, ideas are presented on how to develop an Al alloy suitable for high temperature usage through novel approaches. The dynamic mechanical properties of the improved alloys and developed alloys will be investigated.

The alloy development

The study of Al-Si alloys at high temperature will continue with the development of new alloy systems suitable for elevated temperatures usage. In the field of Al-based amorphous alloys which have possibility to be cast under ordinary conditions, the successful systems are still limited. Based upon the alloying criteria of bulk metallic glasses (BMG), alloy system candidates will be chosen. Their following characteristic will be then investigated; (i) castability and (ii) the mechanical properties at elevated temperature.

Fatigue test

Several Al cast component are being exposed to cyclic loads in their applications. It is therefore interesting to investigate the dynamic mechanical properties of the alloys which showed improved mechanical properties under static testing. Thus, the role of microstructure (e.g. SDAS and Si morphology) on fatigue behaviour of Al-Si cast alloy will be investigated.

Grain refinement

EBSD maps of the as-cast EN AC-46000 alloys revealed that it comprises quite large grains (1-2 mm) irrespective of the cooling conditions. During the literature survey it was noticed that addition of grain refinement agents (like Ti and B) could lower the size of grains, reaching as low as a few microns. In addition the effect of grain refinement on mechanical properties and thermal history of Al-Si cast alloys are less documented.

In-situ tensile testing

In the future, it would be interesting to develop the in-situ investigation on the Al-Si and Al-Si-Cu-Mg alloys during deformation at ambient and elevated temperature. This will help to expand our understanding on deformation behaviour and failure mechanisms. The results will also be comparable with ex-situ tensile tested samples.

REFERENCES

[1] A. Handbook, in, New York. ASM Internacional, 1985.

[2] J.R. Davies, Aluminium and aluminium alloys, ASM international, 1993.

[3] F. Stadler, H. Antrekowitsch, W. Fragner, H. Kaufmann, E. Pinatel, P. Uggowitzer, Materials Science and Engineering: A, (2012).

[4] J. Olofsson, I.L. Svensson, P. Lava, D. Debruyne, Materials & Design, 56 (2014) 755-762.

[5] F. Lasagni, A. Lasagni, E. Marks, C. Holzapfel, F. Mücklich, H. Degischer, Acta materialia, 55 (2007) 3875-3882.

[6] G. Requena, G. Garcés, M. Rodríguez, T. Pirling, P. Cloetens, Advanced Engineering Materials, 11 (2009) 1007-1014.

[7] Z. Asghar, G. Requena, F. Kubel, Materials Science and Engineering: A, 527 (2010) 5691-5698.

[8] F. Stadler, H. Antrekowitsch, W. Fragner, H. Kaufmann, P. Uggowitzer, International Journal of Cast Metals Research, 25 (2012) 215-224.

[9] M. Sahoo, R. Smith, Metal Science, 9 (1975) 217-222.

[10] E. Sjölander, S. Seifeddine, Journal of Materials Processing Technology, 210 (2010) 1249-1259.

[11] F. Stadler, H. Antrekowitsch, W. Fragner, H. Kaufmann, P.J. Uggowitzer, in, 2012, pp. 431-434.

[12] F. Stadler, H. Antrekowitsch, W. Fragner, H. Kaufmann, P.J. Uggowitzer, in, 2011, pp. 274-277.

[13] L. Wang, M. Makhlouf, D. Apelian, International Materials Reviews, 40 (1995) 221-238.

[14] V.M. Karpachev, A.A. Ofengenden, V.S. Zolotorevskii, Izv. Akad. Nauk SSSR, Met., (1989) 133-136.

[15] Z.Y. Liu, Q.Y. Xu, B.C. Liu, International Journal of Cast Metals Research 20 (2007) 109-112.

[16] H. Fredriksson, U. Åkerlind, Solidification and Crystallization Processing in Metals and Alloys, John Wiley & Sons Ltd., Chichester, 2012.

[17] D.M. Stefanescu, Science and Engineering of Casting Solidification, Kluwer Academic/Plenum Publishers, New York, 2002.

[18] H. Fredriksson, U. Åkerlind, Materials Processing during Casting, John Wiley & Sons Ltd, Chichester, 2006.

[19] J.R. Brown, Foseco Non-Ferrous Foundryman's Handbook, Butterworth-Heinemann, Oxford, 1999.

[20] J. Campbell, Complete casting handbook: metal casting processes, techniques and design, Butterworth-Heinemann, 2011.

[21] P.N. Crepeau, in, 1995, pp. 361-366.

[22] M. Makhlouf, H. Guthy, Journal of Light Metals, 1 (2001) 199-218.

[23] M. Djurdjevic, H. Jiang, J. Sokolowski, Materials characterization, 46 (2001) 31-38.

[24] D. Hamilton, R. Seidensticker, Journal of Applied Physics, 31 (1960) 1165-1168.

[25] D.A. Porter, K.E. Easterling, Phase transformations in metals and alloys, CRC PressI Llc, 1992.

[26] B.M. Thall, B. Chalmers, Journal of the Institute of Metals, 77 (1950) 79-&.

[27] S.Z. Lu, A. Hellawell, Metallurgical and Materials Transactions A, 18 (1987) 1721-1733.

[28] D.C. Stouffer, L.T. Dame, Inelastic deformation of metals: models, mechanical properties, and metallurgy, John Wiley & Sons, 1996.

[29] E.R. Petty, Physical metallurgy of engineering materials, Allen & Unwin, 1968.

[30] R.E. Reed-Hill, R. Abbaschian, in, Boston: PWS Publishing Company.

[31] G.E. Dieter, D. Bacon, Mechanical metallurgy, McGraw-Hill New York, 1986.

[32] J.H. Hollomon, AIME TRANS, 12 (1945) 1-22.

[33] D. Ludwigson, Metallurgical Transactions, 2 (1971) 2825-2828.

[34] F. Nabarro, Philosophical magazine letters, 75 (1997) 227-233.

[35] L.-E. Lindgren, K. Domkin, S. Hansson, Mechanics of Materials, 40 (2008) 907-919.

[36] A. Ma, F. Roters, Acta materialia, 52 (2004) 3603-3612.

[37] W. Blum, P. Eisenlohr, F. Breutinger, Metallurgical and Materials Transactions A, 33 (2002) 291-303.

[38] D. Bae, A. Ghosh, Acta materialia, 48 (2000) 1207-1224.

[39] B. Babu, Physically based model for plasticity and creep of Ti-6Al-4V, Division of Material Mechanics, Luleå University of Technology, 2008.

[40] J. Liu, J. Edberg, M. Tan, L. Lindgren, S. Castagne, A. Jarfors, Modelling and Simulation in Materials Science and Engineering, 21 (2013) 025006.

[41] Y. Bergstrom, MAT SCI ENG, 5 (1970) 193-200.

[42] U. Kocks, Journal of Engineering Materials and Technology, 98 (1976) 76-85.

[43] H.J. Frost, M.F. Ashby, Deformation mechanism maps: the plasticity and creep of metals and ceramics, Pergamon press, 1982.

[44] U. Kocks, A. Argon, M. Ashby, Progress in Materials Science, 19.

[45] H.J. Frost, M.F. Ashby, (1982).

[46] H. Mecking, U. Kocks, Acta Metallurgica, 29 (1981) 1865-1875.

[47] J.C. Fisher, W. Johnston, R. Thomson, Dislocations and mechanical properties of crystals, Wiley, 1957.

[48] Y. Bergström, The Plastic Deformation of Metals: A Dislocation Model and Its Applicability, Division of physical metallurgy, Royal Inst. of techn.[Inst. för metallografi, Tekn. högsk.], 1982.

[49] Y. Estrin, A. Finel, M. Veron, D. Mazière, NATO advanced study institute on thermodynamics. Microstructures and plasticity, Kluwer Academic Publishers, France, (2002) 217-238.

[50] G. Voyiadjis, F. Abed, Archives of Mechanics, 57 (2005) 299-343.

[51] Y. Bergström, Rev. Powder Metall. Phys. Ceram., 2 (1983) 79-265.

[52] M. Militzer, W. Sun, J. Jonas, Acta metallurgica et materialia, 42 (1994) 133-141.

[53] A. Jarfors, Journal of Materials Science, 33 (1998) 3907-3918.

[54] W. Lomer, Institute of Metals, London, (1958) 79.

[55] A.D. Freed, K.P. Walker, (1993).

[56] K. Williamson, Research methods for students, academics and professionals: Information management and systems, Elsevier, 2002.

[57] M. Thirugnanam, Transaction of Indian Foundry Congress, 61 (2013) 1-7.

[58] E. Rincon, H. Lopez, M. Cisneros, H. Mancha, Materials Science and Engineering: A, 519 (2009) 128-140.

[59] M. Zamani, S. Seifeddine, A. EW Jarfors, in: Light Metals 2014, 2014.

[60] Annual Book of ASTM Standards. American Society for testing and Materials, (2011).

[61] E. DIN, Aluminium and aluminium alloys–Castings, Chemical composition and mechanical properties, (1998).

[62] C. Caceres, B. Selling, Materials Science and Engineering: A, 220 (1996) 109-116.

[63] M. Avalle, G. Belingardi, M. Cavatorta, R. Doglione, International Journal of Fatigue, 24 (2002) 1-9.

[64] C. Sonsino, J. Ziese, International Journal of Fatigue, 15 (1993) 75-84.

[65] Y. Wang, H. Liao, Y. Wu, J. Yang, Materials & Design, (2013).

[66] H. Liao, Y. Sun, G. Sun, Materials Science and Engineering: A, 335 (2002) 62-66.

[67] M. Zarif, B. Mckay, P. Schumacher, Metallurgical and Materials Transactions A, 42 (2011) 1684-1691.

[68] R. Francis, J. Sokolowski, Metalurgija, 14 (2008) 3-15.

[69] C. Xiang, L. Yanxiang, Research and Development, (2010).

[70] M. Zamani, S. Seifeddine, M. Aziziderouei, in, 2013, pp. 297-302.

[71] N. Tenekedjiev, S. Thomas-Sadowski, Microstructures and Thermal Analysis of Strontium-Treated Aluminum-Silicon Alloys, American Foundrymen's Society, 1995.

[72] L. Backerud, G. Chai, J. Tamminen, American Foundrymen's Society, Inc., 1990, (1990) 266.

[73] L. Dobrzański, R. Maniara, J. Sokolowski, Journal of Achievements in Materials and Manufacturing Engineering, 17 (2006) 217-220.

[74] S. Shabestari, S. Ghodrat, Materials Science and Engineering: A, 467 (2007) 150-158.

[75] S.Z. Lu, A. Hellawell, JOM Journal of the Minerals, Metals and Materials Society, 47 (1995) 38-40.

[76] C.M. Dinnis, M.O. Otte, A.K. Dahle, J.A. Taylor, Metallurgical and Materials Transactions a-Physical Metallurgy and Materials Science, 35A (2004) 3531-3541.

[77] L. Lu, K. Nogita, S. McDonald, A. Dahle, JOM Journal of the Minerals, Metals and Materials Society, 56 (2004) 52-58.

[78] J. Campbell, Castings, Butterworth-Heinemann, 2003.

[79] T.S. Shih, L.W. Huang, Y.J. Chen, International Journal of Cast Metals Research, 18 (2005) 301-308.

[80] S.G. Shabestari, T. Mahmudi, M. Emamy, T. Campbell, International Journal of Cast Metals Research, 15 (2002) 17-24.

[81] Q. Wang, Metallurgical and Materials Transactions A, 35 (2004) 2707-2718.

[82] S. Seifeddine, T. Sjögren, I.L. Svensson, the Journal of Metallurgical Science & Technology, 25 (2007) 12-22.

[83] Y. Han, A. Samuel, F. Samuel, S. Valtierra, H. Doty, Transactions of the American Foundrymen's Society, 116 (2008) 79.

[84] E. Sjölander, S. Seifeddine, Metallurgical and Materials Transactions A, (2011) 1-12.

[85] A. Dons, L. Pedersen, L. Arnberg, Materials Science and Engineering: A, 271 (1999) 91-94.

[86] L.F. Mondolfo, Aluminum alloys: structure and properties, Elsevier, 2013.

[87] D. Apelian, S. Shivkumar, G. Sigworth, AFS transactions, 97 (1989) 727-742.

[88] R. Mahidhara, A. Mukherjee, Journal of Materials Science, 32 (1997) 809-814.

[89] A. Mohamed, F. Samuel, Materials Science and Engineering: A, (2013).

[90] E. Rincón, H. López, M. Cisneros, H. Mancha, M. Cisneros, Materials Science and Engineering: A, 452 (2007) 682-687.

[91] A. Garza-Delgado, K. Kabiri-Bamoradian, R.A. Miller, Die Casting Engineer, 52 (2008) 40-46.

[92] C. Cáceres, J. Sokolowski, P. Gallo, Materials Science and Engineering: A, 271 (1999) 53-61.

[93] A.A. Benzerga, S.S. Hong, K.S. Kim, A. Needleman, E. Van der Giessen, Acta Materialia, 49 (2001) 3071-3083.

[94] R. Li, R. Li, Y. Zhao, L. He, C. Li, H. Guan, Z. Hu, Materials letters, 58 (2004) 2096-2101.

[95] Q. Wang, Metallurgical and Materials Transactions A, 34 (2003) 2887-2899.

[96] Q. Wang, C. Caceres, J. Griffiths, Metallurgical and Materials Transactions A, 34 (2003) 2901-2912.

[97] W. Hunt Jr, J. Brockenbrough, P. Magnusen, Scripta metallurgica et materialia, 25 (1991) 15-20.

[98] F. Roters, D. Raabe, G. Gottstein, Acta materialia, 48 (2000) 4181-4189.

[99] S.-i. Fujikawa, K.-i. Hirano, Y. Fukushima, Metallurgical Transactions A, 9 (1978) 1811-1815.

[100] E. Ogris, A. Wahlen, H. Lüchinger, P. Uggowitzer, Journal of Light Metals, 2 (2002) 263-269.

[101] G. Van Gurp, Journal of Applied Physics, 44 (1973) 2040-2050.

[102] J. Burton, Physical Review B, 5 (1972) 2948.

[103] Y. Xue, C. Burton, M. Horstemeyer, D. McDowell, J. Berry, Metallurgical and Materials Transactions B, 38 (2007) 601-606.

[104] P.D. Chinh, International journal of engineering science, 31 (1993) 11-17.

[105] F. Vollertsen, S. Vogler, Werkstoffeigenschaften und Mikrostruktur, Hanser Muenchen, 1989.

[106] B. Banerjee, A. Bhawalkar, Journal of Mechanics of Materials and Structures, 3 (2008) 391-424.

[107] R.W. Cahn, P. Haasen, Physical metallurgy. Vol. 1, North-Holland, 1996.

[108] A. Roswell, A. Nowick, Transactions, (1953) 1259.

[109] T. Górecki, Berichte der Bunsengesellschaft für physikalische Chemie, 87 (1983) 801-803.

[110] Ø. Ryen, B. Holmedal, O. Nijs, E. Nes, E. Sjölander, H.-E. Ekström, Metallurgical and Materials Transactions A, 37 (2006) 1999-2006.

[111] B. Babu, L.-E. Lindgren, International Journal of Plasticity, 50 (2013) 94-108.

[112] H. Rosenbaum, D. Turnbull, Acta Metallurgica, 6 (1958) 653-659.

[113] H. Rosenbaum, D. Turnbull, Acta Metallurgica, 7 (1959) 664-674.

[114] V. Zenou, A. Kiv, D. Fuks, V. Ezerski, N. Moiseenko, Materials Science and Engineering: A, 435 (2006) 556-563.

[115] F. Lasagni, B. Mingler, M. Dumont, H.P. Degischer, Materials Science and Engineering: A, 480 (2008) 383-391.

APPENDED PAPERS

Supplement I

M. Zamani, S. Seifeddine, A.E.W Jarfors**;** Effects of Microstructure and Defects nn Tensile and Fracture Behaviour of a HPDC Component; Potential Properties and Actual Outcome of EN AC-44300 Alloy, Light Metals Proceeding, TMS 2014. February 16th-20th, San Diego, CA, USA.

Supplement II

M. Zamani, S. Seifeddine, M. Azizderouei; The Role of Sr on Microstructure Formation and Mechanical Properties of Al-Si-Cu-Mg Cast Alloys, Light Metals Proceeding, TMS 2013. March 3rd-7th, San Antonio, TX, USA.

Supplement III

M. Zamani, S. Seifeddine; Assessment of Modification Level in En AC-46000 Aluminium Cast Alloys Using Thermal Analysis and Microscopic Evaluation, Metals Proceeding, TMS 2015. March 15th-19th, Orlando, FL, USA.

Supplement IV

M. Zamani, S. Seifeddine, A.E.W Jarfors; High Temperature Tensile Deformation Behaviour and Failure Process of an Al-Si-Cu-Mg Cast Alloy – The Microstructural Scale Effect. Submitted to the journal of Materials & Design.

Supplement V

M. Zamani, H. Dini, A. Svoboda, L.E Lindgren, S. Seifeddine, N. Andersson, A.E.W Jarfors; A Dislocation Density Based Yield Stress Model for as-cast EN AC-46000 Alloy; Effect of Temperature and Microstructure. To be submitted to the journal of Materials & Design.